TIME-SCALING IN ATOMISTICS AND THE MECHANICAL BEHAVIOR OF MATERIALS

A Dissertation

Presented to

the Faculty of the Department of Mechanical Engineering

University of Houston

In Partial Fulfillment

of the Requirements for the Degree

Doctor of Philosophy

in Mechanical Engineering

by

Xin Yan

December 2016

TIME-SCALING IN ATOMISTICS AND THE MECHANICAL BEHAVIOR OF MATERIALS

Xin Yan

Approved:

Chair of Committee
Pradeep Sharma, Professor,
Department of Mechanical Engineering

Committee Members:

Theocharis Baxevanis, Assistant Professor,
Department of Mechanical Engineering

Yi-Chao Chen, Professor,
Department of Mechanical Engineering

Lars C. Grabow, Assistant Professor,
Department of Chemical and Biomolecular Engineering

Yashashree Kulkarni, Associate Professor,
Department of Mechanical Engineering

Suresh K. Khator, Associate Dean,
Cullen College of Engineering

Pradeep Sharma, Department Chair,
Department of Mechanical Engineering

Acknowledgements

First and foremost, I would like to express my deepest gratitude to my Ph.D. advisor, Dr. Pradeep Sharma, for his patient guidance, understanding, and encouragement. He builds up the relax atmosphere and elastic working schedule, which I enjoy a lot. His outstanding creativity and enthusiasm for science have encouraged me to open mind for feeding my curiosity of scientific problems. His relaxed life style with curiosity and the good sense of humor also have impressed me that being a scientist is a fun and enjoyable experience. Pradeep puts his effort into helping me on every small step I need to make, from forming the logic of the papers, to giving detailed suggestions of how to deliver an insightful presentation. I have been fortunate to work with him. He is not only a research advisor but also a career mentor as well as a good friend for me.

I would like to acknowledge my committees, Dr. Yasharshree Kulkarni, Dr. Yi-Chao Chen, Dr. Lars C. Grabow, and Dr. Theocharis Baxevanis for reviewing my dissertation and giving valuable suggestions and comments.

I have been lucky to have friends here who share their knowledge and experience with me. The list is so long that I cannot accommodate all of them here. Special thanks go to Qian Deng, Afif Gouissem, Yuranan Hanlumyuang, Fatemeh Ahmadpoor, Dengke Chen, Xiaobao Li, Shuyin Jiao, Shengyong Yang, Shengjie Tang, Nikhil Walaniand, Sana Krichen, and all the other fellows for their sincere supports and all the unforgettable moments during the last five years.

Special thanks to Jeffrey S. Sarlo. Even though we never meet, he helped me through tons of Emails during my Ph.D journey. His timely response, even in weekend and evenings, and detailed instruction made my life much easier. He is always responsible and resourceful. Without his help, I could not have make the in-house code running in the cluster. Also, I appreciate the help from all the staff in the Department of Mechanical Engineering, including Trina, Karina, Tracy, April, Joana, Cesily, etc.

I own special thanks to my friend, Xu Liu, for his consistent help and invaluable suggestions on programming.

Sincere and infinite thanks to my parents for their endless love and support throughout

my life. Special thanks to my parents in law for their generous help and support, especially on taking care of my baby. I want to dedicate my dissertation to my beloved husband, Jiebo Li, for the happiness we shared every day. It is my luck to have him in my life and his love, patient, and support make it possible for me to overcome all the hardship of my Ph.D. Last but not least, my naughty little girl, Yuyan, who is the sweetest part of my heart and who forces me to learn how to work efficiently.

TIME-SCALING IN ATOMISTICS AND THE MECHANICAL BEHAVIOR OF MATERIALS

An Abstract

of a

Dissertation

Presented to

the Faculty of the Department of Mechanical Engineering

University of Houston

In Partial Fulfillment

of the Requirements for the Degree

Doctor of Philosophy

in Mechanical Engineering

by

Xin Yan

December 2016

Abstract

Modeling physical phenomena with atomistic fidelity and at laboratory time-scales is one of the holy grails of computational materials science. Conventional molecular dynamics (MD) simulations enable the elucidation of an astonishing array of phenomena inherent in the mechanical and chemical behavior of materials. However, conventional MD, with our current computational modalities, is incapable of resolving time-scales longer than microseconds (at best).

In this dissertation, using a recently proposed approach—the so-called autonomous basin climbing (ABC) method— together with other techniques, including nudged elastic band (NEB), kinetic Monte Carlo (KMC), and transition state theory (TST),we provide several insights on some key problems in material science. The following topics are addressed:

(i) Li diffusion in amorphous matrix: Using ABC-based approach, a realistic evaluation of Li-ion diffusion pathways in amorphous Si is evaluated. Diffusive pathways are not *a priori* set, but rather emerge naturally as part of our computation. The comparative differences between Li-ion diffusion in amorphous and crystalline Si is elucidated.

(ii) Rate-dependent mechanical behavior of crystalline nano-structure: A study of the mechanical compression behavior of nano-slabs to specifically interrogate its deformation behavior under both slow and fast strain rates. While high-strain rate deformation proceeds in an unremarkable manner—merely shortening its length along with the formation of an expected defect sub-structure, the slow-strain rate results (—precisely what is to be expected in most applications and laboratory experiments) exhibit a dramatically different behavior. We observe “liquid-like”deformation under low strain rate.

(iii) Elucidating the micro-mechanisms of rate-dependent plasticity in a-LiSi nano-structure: Silicon is arguably one of the most important electrode materials in Li-battery system. In this study, we conduct slow strain rate computational studies to provide insights into the mechanisms underpinning plastic deformation of amorphous Li-Si. We find that in the case of Li-Si nano-structures, the basic mechanism of plasticity are similar

to what has been discussed in other amorphous system—formation of shear transformation zone engineered by diffusion like process. We also identify the rotation of the STZ as a key dissipation mechanism. Furthermore, the behavior under high & low strain rate is quite different and accordingly convectional MD cannot be used to understand plasticity.

Table of Contents

List of Figures

List of Tables

1 Chapter 1: Introduction and Overview

1.1 Motivation for Long-time Scale Atomistic Simulations

In 1934, G.I. Taylor made, what is now, a historical speculation that atomistic defects called "dislocations"are responsible for the ductile "plastic"deformation of metals [9]. Were the scientists of that time to have had recourse to molecular dynamics (MD) algorithms and modern computers, this would not have been *mere* speculation, and direct evidence of dislocation-mediated plasticity would be at hand. This arguably artificial scenario underscores the power of conventional MD simulations to provide microscopic insights into material behavior that sometimes may not be easily discernible experimentally [1]. Indeed, conventional MD, which simply consists of numerically solving the Newtonian equations of motion for a set of atoms, has unrivaled predictive power in providing a microscopic window to the chemical, mechanical and physical behavior of materials. MD can be used to elucidate atomistic structures and mechanisms that aid in the interpretation of the experiment, or even reveal behavior that is unavailable to test in a laboratory setting. Archival literature and, now even textbooks [10, 11], are rife with examples of the success achieved by MD in understanding physical phenomena from an atomistic viewpoint.

In principle, MD can be used to obtain any thermodynamic or kinetic quantity, without introducing approximations beyond the assumption of classical mechanics and what may be involved in deriving an interatomic potential. However, when we integrate the equations of motion $-\frac{dV}{dr_i} = m_i \frac{d^2 r_i}{dt^2}$ [2] in MD, the resolution of individual atomic vibrations requires an integration time-step of the order of femtoseconds (10^{-15} seconds). Even the fastest processors of our times can, at present, achieve total simulation times of microseconds (10^{-6} seconds). The time-integration is inherently sequential in nature, and accordingly direct parallelization does not help much in resolving the "time-scale bottleneck"of conventional MD[3]. This time-scale limitation of conventional MD restricts its usefulness to phenomena

[1] While MD simulations are of importance in a diversity of disciplines such as chemistry, physics and biology among others, we will primarily focus on materials with a further emphasis on mechanical aspects.

[2] V is the interatomic potential.

[3] We remark however that parallelization has had a very positive impact on bridging lengths scales and thus now large system sizes consisting of billions of atoms can be handled.

that occur within micro to nanosecond time scales. Thus, many interesting physical processes that occur at much longer time scales than microseconds, i.e. creep, diffusion, protein unfolding, grain boundary dynamics, etc. are inaccessible by conventional MD.

In the past, researchers have attempted simulation acceleration via application of higher temperatures [12], high stress [13], and high strain rate [14]. Unfortunately, all these treatments may conceal important behavior and mechanisms during deformation. Accessing long time scales in atomistics has therefore become an intensely studied research topic within the past decade, and notable success has been achieved using different approaches. Complete success, however, has still been elusive and all approaches have their respective strengths and limitations. Among many, the Autonomous Basin Climbing (ABC) method is one of the attempts to circumvent the time-scale issue of traditional MD [15, 16]. This algorithm was originally applied to the study of supercooled liquids, viscosity, and glass transition [16].

1.2 Long Time Scale Atomistic Methods

Over the past few decades, there have been various attempts to extend the time scale of atomistic simulations beyond those that can be accessed with traditional MD. These approaches can be categorized into two groups. The first are those that are based on potential energy surface (PES) exploration, where different techniques are developed to efficiently explore the PES.

The second set of approaches can generically be grouped as accelerated MD approaches. In this category, different techniques are utilized to accelerate traditional MD, thereby extending the timescales that can be accessed using molecular simulation.

1.2.1 Potential Energy Surface Exploration

A general approach to determining the evolution of an atomistic system without explicitly solving and integrating Newton's equations of motion is through PES exploration, where transition state theory (TST) provides a link between the time evolution of the system to the topology of the underlying PES. It is shown in Figure 1.1 a one-dimensional PES, with different local energy minima that can be accessed by climbing over the various

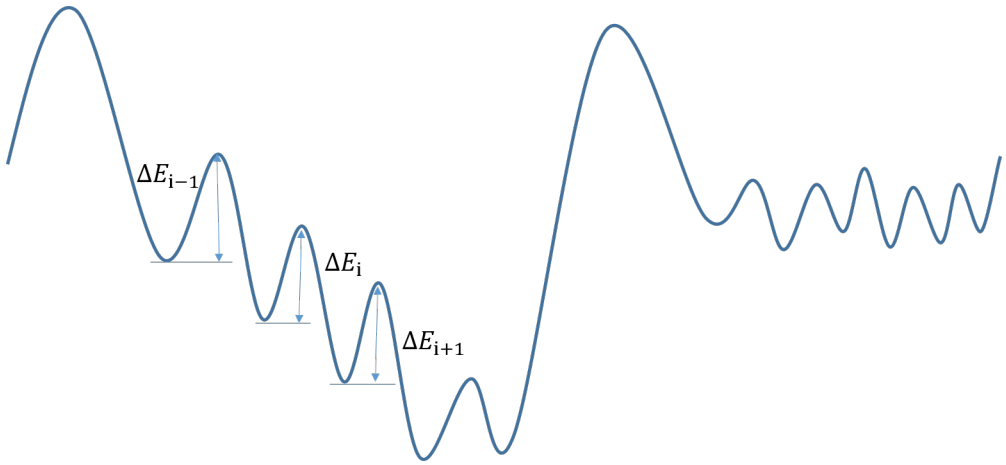

Figure 1.1: Schematic of a 1-D potential energy surface.

energetic barriers $\Delta E_{(i)}$. In general, the PES is $3N$-dimensional, where N is the number of atoms in the system. Various approaches have been proposed that enable efficient and accurate exploration of the $3N$-dimensional PES.

One approach is metadynamics [17], which was originally developed as a free energy surface sampling technique, but has evolved to function as a general PES exploration technique that can resolve saddle points, local energy minima, and the connecting energetic barriers. Metadynamics works by adding Gaussian functions to the PES to force the system out of local energy minima and into neighboring energy wells. In order to reduce the infinite number of configurations that can be explored on the PES, metadynamics utilizes so-called "collective variables ", which are functions of the system configuration that are used to bias the PES search directions. Examples of such collective variables are coordination numbers, potential energies, box shapes, and path variables [18]. Metadynamics is limited in the number of atoms that can be modeled due to its need to store all previously used Gaussian functions, which is necessary to prevent the system from re-exploring previously found potential energy basins.

Other approaches to finding neighboring local minima, and thus explore the PES include the activation-relaxation technique (ART) [19, 20], and the dimer method [21]. ART is a method of searching the saddle points associated with a selected basin on the PES. ART works by applying a perturbation to a relaxed system, which forces the system up a potential energy well to locate the saddle point. The system is then set back to the

relaxed energy minimum, at which point another perturbation is applied [19, 22]. ART has been used with success in various applications [23], but does exhibit shortcomings due to increasing computational expense for complex non-equilibrium processes, where it can encounter difficulties related to computational expense in finding a final, desired system configuration [24].

In the dimer method [21], one rotates a dimer (two replicas with constant distance) to find the lowest curvature mode of the PES at the current position. The approach subsequently forces the dimer to move up the PES along this direction to find the saddle point. Similar to ART, once a saddle point is reached, the system is set back to the original local energy minimum, and displaced along another random direction to find other saddle points.

The discrete path sampling (DPS) method of Wales [25, 26] is another approach to PES exploration. This approach has been used, for example, for applications involving different aspects of protein folding and unfolding [27, 28]. Equilibrium mapping approach [8] uses branch-following and bifurcation algorithms to generate a diagram that contains information regarding the possible stable and unstable equilibrium states on the PES.

The approaches that have been discussed above all deal with finding a pathway between a specified initial configuration, and a resulting, generally unprescribed final configuration. Intrinsic to these PES exploration techniques is the fact that the concept of time, i.e. the real physical time a system would expend in going from the initial to the final configuration, is not addressed. Instead, the output of these PES exploration simulations is typically the energy barriers that have been crossed in going from the initial to final configuration. Thus, once the pathway between two configurations on the PES has been determined, connections to time t can be made through transition state theory (TST) [29, 30], i.e.,

$$t = \sum_{i=1}^{N} \left(\nu \exp^{-\Delta E_i / k_B T} \right)^{-1}, \tag{1.1}$$

where ΔE_i is the energy barrier separating energy minima $i-1$ and i, N is total number of energy minima explored, ν is a frequency prefactor that is typically chosen to be on the order of 10^{12} s^{-1} for crystalline solids, T is the temperature and k_B is the Boltzmann constant. Through this TST connection, one can calculate the amount of time needed for a

specific energetic transition to occur, or for the system to reach a specific final configuration.

An important comment to make is that Eq. (1.1) makes clear that the calculated time t needed to cross an energy barrier on the PES is dependent on the accuracy of the energy barrier ΔE_i. In other words, errors in computing this value may lead to either under or over prediction of the barrier crossing time. Due to this feature, besides methods that explore the PES by finding neighboring energy minima, methods exist that enable accurate calculation of each energy barrier that is crossed during the PES exploration. Perhaps the most widely used approach to calculating the value of the energy barriers by finding the minimum energy pathway (MEP) is the nudged elastic band method (NEB) [31]. One of the artifacts that plague ABC and other PES exploration methods is that often the saddle points are discovered in a sequence that is not physically relevant. Accordingly, it is usually necessary to employ a technique such as kinetic Monte Carlo (KMC). KMC can be applied to select the most probable path a system may take starting from some initial minimum state to the various minima identified during the ABC-based PES exploration.

1.2.2 Extended Timescale Atomistic Methods

Apart from PES exploration techniques, extensive efforts have been dedicated to accelerating traditional MD. Much of this effort has been performed by Voter and co-workers, who have developed a range of approaches to extending the time scale in MD simulations, including parallel-replica dynamics [32], hyperdynamics [33], and temperature-accelerated dynamics [34, 35].

In parallel-replica dynamics, the system is first replicated on M processors. Each replica is evolved forward independently using thermostatted MD. After a transition is detected in any of the replicas, the parallel simulations of all replicas are terminated, and the transition time can be calculated as the summation of the trajectory time over all replicas [36]. An extensive discussion of parallel-replica dynamics was recently given by Perez et al. [32].

In hyperdynamics, a bias potential is added to the PES in the areas close to local minima. In this way, the height of the barriers between different states is reduced. A boost factor can be obtained due to the bias potential, which can be used to scale the transition time [33]. However, the bias potential must be zero at the dividing surfaces

between two minima, and must also satisfy the constraint that the bias potential does not erroneously alter the dynamical evolution of the system, which introduces challenges and significant computational cost in effectively applying the bias potential in hyperdynamics applications. Because of this, other researchers have pursued different approaches to adding the bias potential. For example, in the accelerated MD approach, the bias potential is applied to the entire PES when the system potential energy is below a certain threshold, which has been used to study the configurational space of biological materials in an efficient manner [37]. Simple versions of hyperdynamics using local bias potentials, such as the bond-boost [38] and strain-boost [39] methods, have also been proposed to increase the efficiency and accuracy of hyperdynamics-type approaches, and recent approaches using hyperdynamics to study fracture in crystalline materials containing millions of atoms have recently been performed [40].

Temperature-accelerated dynamics accelerates the transitions by increasing the temperature in the MD simulation, after which an extrapolation to the low-temperature regime is performed assuming Arrhenius behavior while filtering out the transitions that could not have occurred at the required temperature [34]. While large time boosts can be achieved, the temperature-accelerated dynamics method appears to be most effective for systems where the lowest energy barrier of interest is relatively high [32].

1.3 Dissertation Overview

In this dissertation, we provide a broad overview of ABC-based approaches for time-scaling and applications to contemporary materials science problems. The rest of the dissertation is organized as described below:

In Chapter 2, we describe the fundamental principle of ABC-based time-scaling algorithms as well as other techniques we have applied. A few different ABC-based simulation approaches are discussed and compared. Examples from published literature are reviewed.

In Chapter 3, we present a computational study of Li diffusion in amorphous silicon matrix.

In Chapter 4, we investigate the mechanical deformation of a nano-slab under slow compression from an atomistic point of view.

In Chapter 5, we elucidate the mechanism underpinning plasticity in amorphous Li-Si alloy nano-structure in different strain rates.

Finally, in Chapter 6, we conclude this dissertation by summarizing the highlights and limitations of current approach and presenting some avenues for future exploration.

2 Chapter 2: Computational Approach

2.1 Autonomous Basin Climbing (ABC) Sampling Method

2.1.1 Original ABC PES Sampling Method

The autonomous basin climbing (ABC) method was originally proposed by Yip and co-workers in 2009 [41, 42]. It has since been applied to a wide range of phenomena which require atomistic resolution at time scales far beyond those accessible via traditional MD, including trapped self-interstitial atom clusters [43], strain-rate effects on yield stress [44], interstitial emission at grain boundaries [45], diffusion [24], and viscous relaxation [16]. The original ABC method, which is an activation-relaxation method used to explore and reconstruct the PES, is illustrated in Figure 2.1. Specifically, the ABC PES sampling process involves the following steps:

i An initial structure at an energy minimum, i.e. $E_{min}^{(1)}$ in Figure 2.1(a), is chosen.

ii A penalty function $\phi_i(\mathbf{r})$ with particular shape is added to the system, where i denotes the local penalty function number. The width and height of the penalty functions determines the sampling resolution of the PES; these parameters are often dependent on the specific physical problem of interest as discussed later. The penalty functions typically assume Gaussian-like shapes, i.e.,

$$\phi_i(\mathbf{r}) = \omega \exp[-(\mathbf{r} - \mathbf{r}_{min}^i)^2/2\sigma^2], \tag{2.1}$$

which are centered at the minimum energy configuration $\mathbf{r}_{min}^i$. The parameters ω and σ control the strength and width of the penalty function. These penalty functions modify the potential energy $\Psi(\mathbf{r})$ as

$$\Psi(\mathbf{r}) = E(\mathbf{r}) + \sum_{i=1}^{p} \phi_i(\mathbf{r}), \tag{2.2}$$

where $\mathbf{r}$ are the 3N-dimensional atomic configurations and p is the total number of penalty functions.

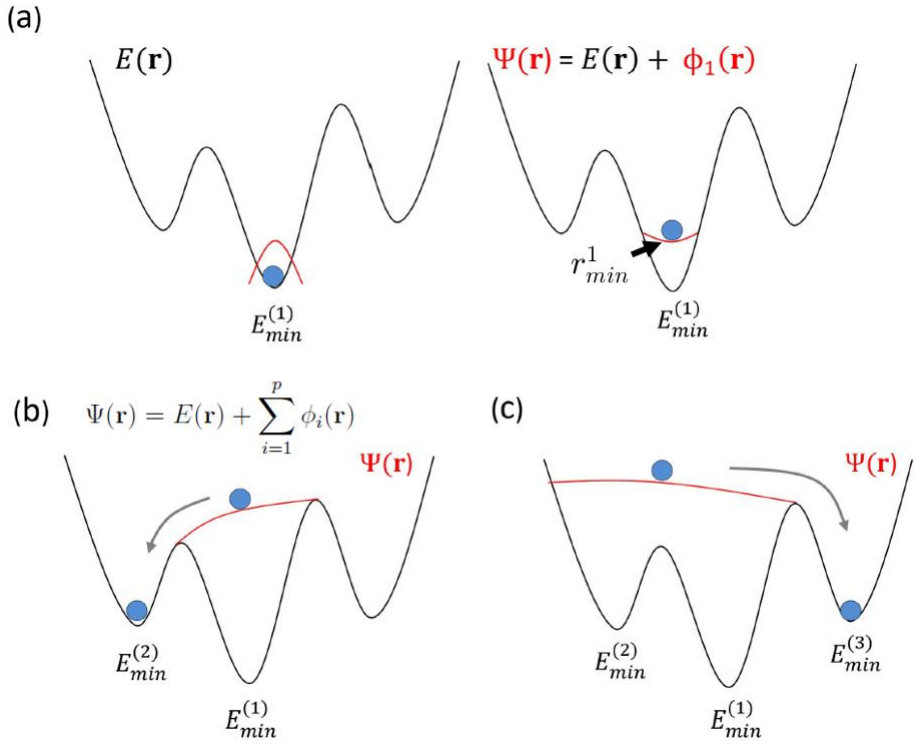

Figure 2.1: Illustration of basin filling with penalty functions in the ABC method. (a) Penalty function ϕ_1 added to PES, with the center of the penalty functions at $\mathbf{r}^i_{min}$; (b) and (c) Continue adding additional penalty functions to push.

iii The system is relaxed using static energy minimization (i.e. using conjugate gradient energy minimization) to find the next minimum energy configuration $\mathbf{r}^{i+1}_{min}$ on the penalty function-modified PES.

iv Repeat starting from step II until the target physical phenomenon is observed.

The above outline and Figure 2.1 make clear that there are similarities and differences with metadynamics [17, 18]. For example, metadynamics was designed as a dynamic sampling tool for exploring the free energy surface. In contrast, the ABC method is limited to PES exploration method as static energy minimization is used to relax the system between penalty function increments. Another key difference is that the penalty functions in metadynamics are typically constrained by a choice of collective variables [17]; these are used because of the computational expense inherent to considering entropic effects, and also to reduce the dimensions of the free energy landscape search. In contrast, the ABC method does not

utilize collective variables, and thus represents an unconstrained PES search methodology. The practical implications of this difference are that the ABC method can, in theory, find all transitions on the PES, though not all of them may be important or relevant, whereas metadynamics will only find those transitions that are of relevance to the collective variables.

The discussion above corresponds to the original ABC method of Kushima et al. [41, 42]. Since 2009, multiple groups, have identified and attempted to ameliorate deficiencies that have been identified with the basic ABC PES exploration method. These issues include: (1) Computational expense related to storing penalty functions for PES exploration; (2) Resolving the one-dimensional nature of the PES search that is intrinsic to the ABC method; (3) Improving the accuracy of energy barriers obtained through the ABC PES exploration; (4) Choosing the most probable ABC pathway or trajectory. We now describe each of these in detail.

2.1.2 Self-Learning Metabasin Escape Algorithm

One of the key computational bottlenecks facing the basic ABC method is the increasing number of penalty functions that must be stored as more and more of the PES is explored. The reason for this is illustrated in Figure 2.1(b) and (c). Specifically, in Figure 2.1(b), a sufficient number of penalty functions are applied such that the system exists the energy well defined by the minimum $E_{min}^{(1)}$, and into the neighboring energy well defined by the local minimum $E_{min}^{(2)}$. Additional penalty functions are applied to the energy well with $E_{min}^{(2)}$ until the system is able to exit to the neighboring energy well with minimum $E_{min}^{(3)}$. In going from $E_{min}^{(1)}$ to $E_{min}^{(3)}$, all of the penalty functions that are applied need to be stored, or else the system could fall back into the energy well containing the local minimum $E_{min}^{(1)}$ in going from $E_{min}^{(2)}$ to $E_{min}^{(3)}$. In general, keeping previously applied penalty functions are necessary to prevent the system from falling into and re-exploring energy basins that have already been explored, though this means that the computational expense associated with the PES search increases dramatically as more of the PES is explored.

To mitigate this problem, Cao et al. [46] formulated a self-learning strategy to improve the PES exploration efficiency, termed the self-learning metabasin escape (SLME) method. Starting from an initial configuration that is a local energy minimum, a small random

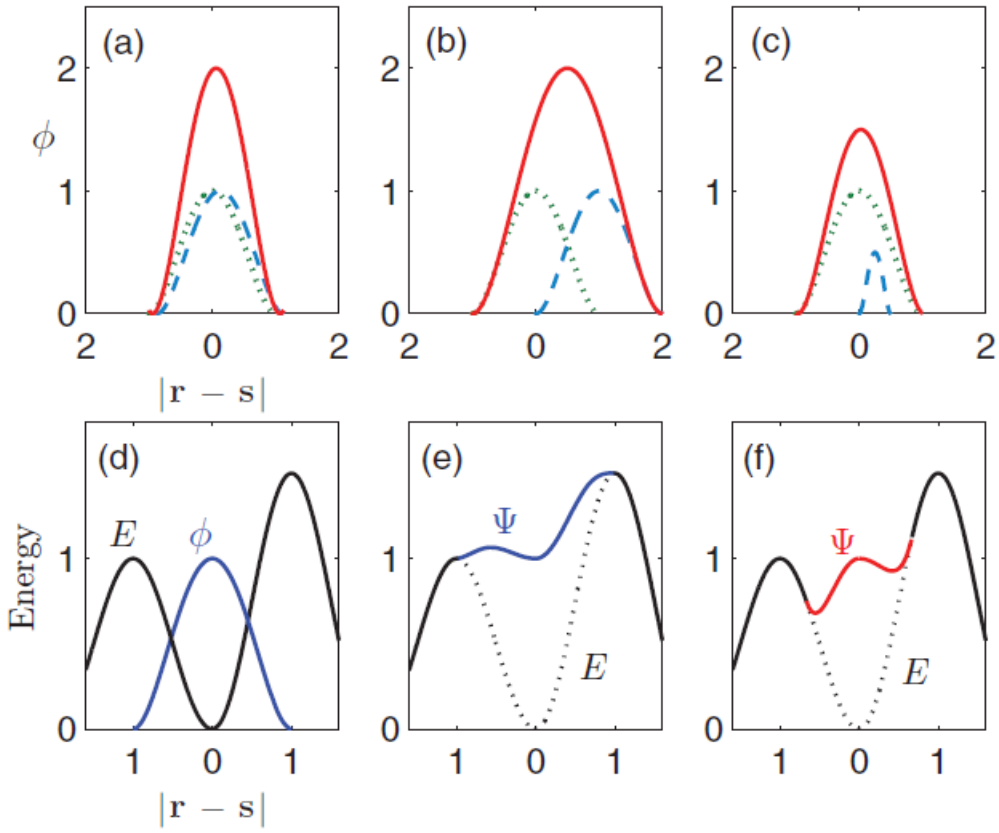

Figure 2.2: (a)-(c) Three different types of combination of two small penalties. (d) The original energy E and the penalty function ϕ. (e) Their augmented energy Ψ still has a dip at the original local minimum. (f) The augmented energy Ψ using a smaller half-width.

penalty function is applied to the system. Starting from the second penalty function, after adding each penalty function to the system, an overlap check is carried out. If the distance between the center of the newly added penalty function and any of the previous penalty functions is less than the sum of their half-widths, these two penalty functions will be replaced by a new, single penalty function with height equal to the sum of the two penalty functions and width of $\boldsymbol{W}_n$, which can be written as [46]

$$| \boldsymbol{W}_n | = max[\frac{| \boldsymbol{s}_i - \boldsymbol{s}_j | + | \boldsymbol{W}_i | + | \boldsymbol{W}_j |}{2}, | \boldsymbol{W}_i |, | \boldsymbol{W}_j |], \tag{2.3}$$

The center of the new penalty function will be shifted to

$$\boldsymbol{s}_n = \frac{\mid \boldsymbol{W}_i \mid h_i \boldsymbol{s}_i}{\mid \boldsymbol{W}_i \mid h_i + \mid \boldsymbol{W}_j \mid h_j} + \frac{\mid \boldsymbol{W}_j \mid h_j \boldsymbol{s}_j}{\mid \boldsymbol{W}_i \mid h_i + \mid \boldsymbol{W}_j \mid h_j}. \tag{2.4}$$

In the expressions above, $\boldsymbol{s}$ and h represent the center and the height of the penalty functions, respectively. The new penalty function will be treated as the current penalty function, and the previous identified two overlapped penalty functions can then be removed from memory. Figure 2.2 demonstrates three typical cases of how overlapping penalty functions can be combined, i.e., (a) Two sequential fully overlapped penalty functions (green, dotted curve and blue, dashed curve) give a strong indication of inefficient sampling. The combined penalty function (red, solid curve) doubles the local curvature to assist the system in moving away from the stuck configuration. (b) Two slightly overlapping penalty functions. Combination of two penalty functions (green, dotted and blue, dashed curves) at the maximal separation. The new penalty function (red, solid curve) has a half-width that is 3/2 times of the original values. (c) The combination of a larger and smaller penalty function. The SLME approach was shown to lead to significant decreases in computational expense, and thus enables the ABC method to find significantly more local energy minima on the PES in a shorter amount of time, as shown in Cao et al. [46].

2.1.3 Extended ABC (ABC-E)

Another modification of the basic ABC algorithm was developed by Fan and co-workers [24] which is called the extended ABC (ABC-E). In ABC-E, after a new energy basin is identified, the system is sent back to the initial energy basin and a Gaussian penalty function is added on the saddle point to block the identified pathway. Penalty functions are then added until another saddle point is found, at which point the system is again placed back into the initial energy basin while the newly found saddle point is blocked with penalty functions. In this way, a series of distinct exits or transition pathways from a single energy basin can be identified. Identifying the exit pathways in order of increasing activation barrier enables them to be sorted according to their relative importance and contribution to the process kinetics.

Table 2.1: Comparison of different ABC PES sampling approaches

	Original ABC [41]	ABC-E [24]	ABC-SLME [46]
Simple description	Starting from current energy minimum, Gaussian penalty functions are added to push the system to climb out of the current energy well.	After a new minimum is identified using ABC, a penalty function is added on the saddle point to block the identified path. The system then is set back to the initial state to find other possible transition pathways out of the energy basin.	If the new added penalty function overlaps with existing ones, the overlapping penalty functions will be replaced by a new, larger one .
NEB is used to accurately calculate the energy barriers	Yes	Yes	No
sampling efficiency	Intermediate	Slowest	Fastest
time estimation	Less accurate	More accurate	Less accurate

Thus, the ABC-E, and the ABC-SLME represent the two major algorithmic improvements to the original ABC method. Aside from the distinctions already discussed, another key difference between them is that ABC-E may provide more accurate estimations of transition time because it is not a 1D PES searching tool [24], in contrast with the ABC-SLME. However, there exists a trade-off in computational expense, with ABC-E being more expensive than ABC-SLME. This, and the other choices discussed above lead to trade-offs in terms of sampling rigor and computational efficiency, which are summarized in Table 2.1.

2.1.4 Rate Constants

Regardless of the specific ABC PES methodology that is utilized, the output from an ABC PES search are all the energy barriers that are crossed, as well as all of the local energy minima. However, one shortcoming that is intrinsic to all of the discussed ABC methods is an overestimation of the energy barriers connecting neighboring energy minima, which thus causes an overestimation of the corresponding transition times. One approach to mitigating this issue is to utilize penalty functions with smaller heights. However, this requires more penalty functions to exit a given local energy well, and thus results in significantly enhanced

computational cost. Alternatively, minimum energy pathway strategies, which are superior in calculating energy barriers, such as the NEB [31] and finite temperature spring (FTS) [47, 48], can be adopted. After refining the energy barriers obtained from ABC using NEB or FTS, the transition times can be calculated through TST using Equation (1.1).

However, the ABC PES searches are not deterministic in the sense that starting from the same local energy minimum on the PES, different ABC trajectories based on different parameters, namely the penalty function width σ and strength ω, may identify different minimum energy pathways, or different sequences of local energy minima. Thus, kinetic Monte Carlo (kMC) [30] is used to ascertain the most probable pathway that the system follows in going from one physical state to another. This method is used to calculate the corresponding possibilities for the system to cross every barrier (that has been identified) and to determine the most probable transition trajectory to cross the various energy barriers. With all the barrier information calculated from ABC or a MEP method like NEB, TST is then applied to estimate the rate constant for each event (crossing a barrier):

$$k_{ij} \propto exp[-\Delta E/k_b T], \tag{2.5}$$

where k_{ij} is the rate constant for the single event, ΔE is the barrier energy calculated from ABC/MEP, k_b is Boltzmann constant, and T is the temperature. The rate constant divided by the summation of the rate constants of all possible events from the current state yields the possibility of this single event. One of the possible transitions is randomly chosen based on the relative possibilities by comparing a randomly generated number in the range of (0,1] to an array of partial summation of the possibilities as illustrated in Figure 2.3. Starting from the new state, with the corresponding rate constants in the rate matrix, the same action is taken to find the next transition state.

We hope that the preceding discussion has demonstrated that the best strategy for extracting useful information from numerical simulations is to use several tools synergistically, while exploiting the advantages of each. In this respect, ABC is complementary to other techniques, such as minimum energy pathway (MEP) searches, harmonic transition state theory, and kinetic Monte Carlo, which are less efficient in PES sampling, but advanced in

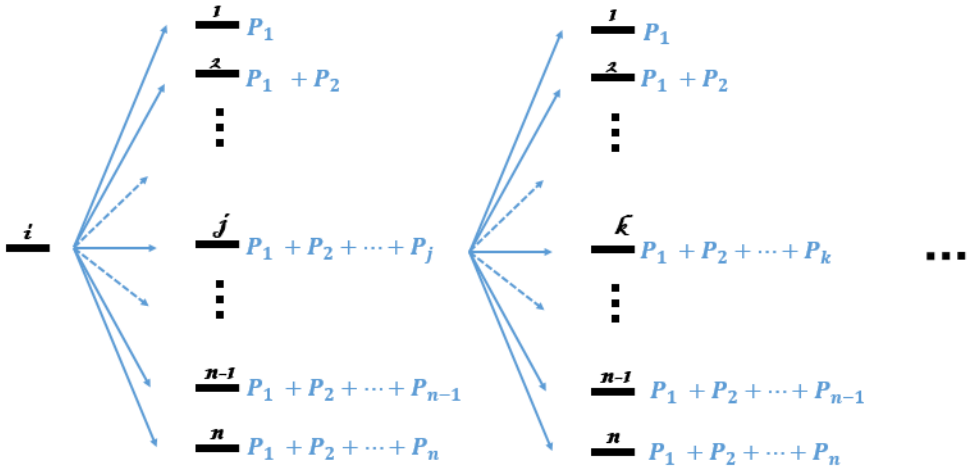

Figure 2.3: KMC algorithm.Reprinted from [1] with permission from Elsevier.

terms of detailed analysis of the transition pathways.

2.2 ABC for Slow Strain Rate and Long Timescale Atomistic Simulations

As previously discussed, in conjunction with other techniques, the ABC method has shown substantial promise in studying atomistic processes that occur at long time scales. However, an important area that has until recently remained underdeveloped and underexplored is the specific question of how the ABC method of PES exploration can be utilized to study problems in which constant forces, or mechanical loading, are applied, or where the strain rate ($\dot{\epsilon}$) that is applied to the system is on laboratory time scales, i.e. $\dot{\epsilon} \approx 10^{-2}$ s^{-1}, and where the total amount of time that needs to be simulated is on the order of seconds or longer. In this section, we describe multiple methodologies that have recently emerged that use the ABC PES exploration method as an essential component to performing atomistic modeling at experimental strain rates and time scales.

2.2.1 Method 1: No Mechanical Loading or Constant Stress Loading

The first approach can be used to study atomistic systems without loading or with constant stress [1, 5]:

i For a given set of boundary conditions, the ABC method is used to sample the PES—this determines the local energy minima of the PES as well as the saddle points, thus yielding the energy barriers between different local minima;

ii The energy barriers obtained from ABC are approximate since the determination of the saddle points can be in error based on the resolution of the ABC sampling. Accordingly, to extract accurate energy barriers, NEB is applied to *all* of the pairs of local energy minima that are obtained from the ABC PES search;

iii With the energy barriers in hand, KMC is used to find the most probable pathway between the different PES minima;

iv Following the pathway provided in step iii, TST is used to calculate the transition time between two steps.

This approach uses the ABC method to find the pathway between the initial and final configurations, but exploits other techniques to get accurate energy barriers, and thus accurate transition times that are needed to move from one local energy minimum to another. This approach can thus be used to find processes that occur at time scales slower than those accessible to classical MD, but cannot be used for problems where the external loading is a prescribed strain rate.

2.2.2 Method 2: ABC-SLME Method with Constant Clamping Forces

A different set of mechanical boundary conditions that is important to model for long timescale simulations is that of a constant clamping force. Clamping forces are most often used in steered molecular dynamics (SMD) studies of protein unfolding to mimic the experimental approach of applying forces to proteins via optical tweezers, or an atomic force microscope (AFM) [49, 50, 51, 52, 53]. The methodology described here has been used in conjunction with the ABC-SLME approach to sampling the PES to study the mechanically-driven unfolding of various proteins [6, 54, 55].

i Apply constant force to specific parts of the molecular system, i.e. the termini of a protein;

ii Apply a penalty function, followed by an energy minimization;

iii Repeat step II until the protein has unfolded.

The reason this approach is able to access the experimentally observed unfolding times of seconds is due to the continued application of penalty functions, where it is important to note the utility of the ABC-SLME approach here in enabling the PES exploration by significantly reducing the memory requirements for storing penalty functions in previously explored portions of the PES. In other words, for the small clamping forces that are applied (100 pN or smaller), the protein is likely to become stuck in various potential energy basins, and would remain stuck if not for the applied penalty functions. The penalty functions which are continuously applied to boost the system out of energy basins can be interpreted as thermal activation that assists the mechanical (clamping) force in enabling the system to escape from energy wells that it would otherwise become stuck in. The heights of all energy barriers ΔE_i that are crossed over can be used in Equation (1.1) to determine the total unfolding time.

2.2.3 Method 3: ABC-E Combined with On-the-fly KMC

The ABC-E method was designed for problems, such as diffusion, in which there are multiple competing physical processes, and thus energetic pathways on the PES, that are connected to the same energetic configuration. The ABC-E method can be applied to identify the competing states around the initial state [24]. The simulation steps are shown in the flowchart in Figure 2.4, where the detailed description is as follows:

i Starting from a local energy minimum, ABC is used to find a neighboring energy well;

ii Record the newly found state, and apply a large penalty function on the saddle point and set the system back to the previous minimum energy configuration just prior to crossing the saddle point;

iii Continue ABC to find another connected energy basin;

iv Judge whether it is a new state or a previously visited state is found: (a) if it is a new

state, calculate the possibility factor $\alpha(T)$ (Possibility factor $\alpha(T) = \frac{exp\left(-\frac{E^{new}}{k_b T}\right)}{\sum_{N_{states}^{obs}} exp\left(\frac{-E_i^{obs}}{k_b T}\right)}$. In this equation, E^{new} is the energy of newly identified barrier and E_i^{obs} is the energy of observed barriers.), if $\alpha(T) < \alpha(T)_0$, stop sampling, otherwise go to step II; (b) if it is a previously visited state, put the system back to the previous state and add additional blocking penalty on the saddle point. Restart step IV;

v Apply NEB to refine all the saddle points identified in the ABC sampling.

vi Apply KMC to select one final transition state from all the states identified in ABC;

vii Starting from the selected state, go back to step I.

2.2.4 Method 4: Controlling Strain Rate via Connection to the PES

In many problems in which the mechanical properties of atomistic systems are studied, a constant, but unrealistically large strain rate is applied [56, 57, 58]. To incorporate the effects of strain rate, Cao *et al.* [59, 3, 60] proposed an approach coupling the ABC-SLME method with Monte Carlo, as illustrated in Figure 2.5. In this approach, the connection between strain rate and the energy barriers crossed on the PES is obtained by utilizing an expression for strain rate [61] that was derived from transition state theory assuming constant temperature:

$$\dot{\gamma} = n v_0 \frac{k_\mathrm{B} T}{\mu \Omega} \exp\left[-\frac{Q^*(T) - T S_\mathrm{c}}{k_\mathrm{B} T}\right], \tag{2.6}$$

where n is the number of independent nucleation sites, v_0 is the attempt frequency, μ is the shear modulus, Ω is the activation volume, Q^* is the energy barrier and S_c is the activation configurational entropy, which has previously been calculated, for example, for crystalline FCC metals for the specific case of dislocation nucleation [62].

Then, by defining a characteristic temperature-dependent prefactor [63, 64]:

$$\dot{\gamma}_0(T) = \frac{k_\mathrm{B} T n v_0}{\mu \Omega} \exp\left(\frac{S_\mathrm{c}}{k_\mathrm{B}}\right). \tag{2.7}$$

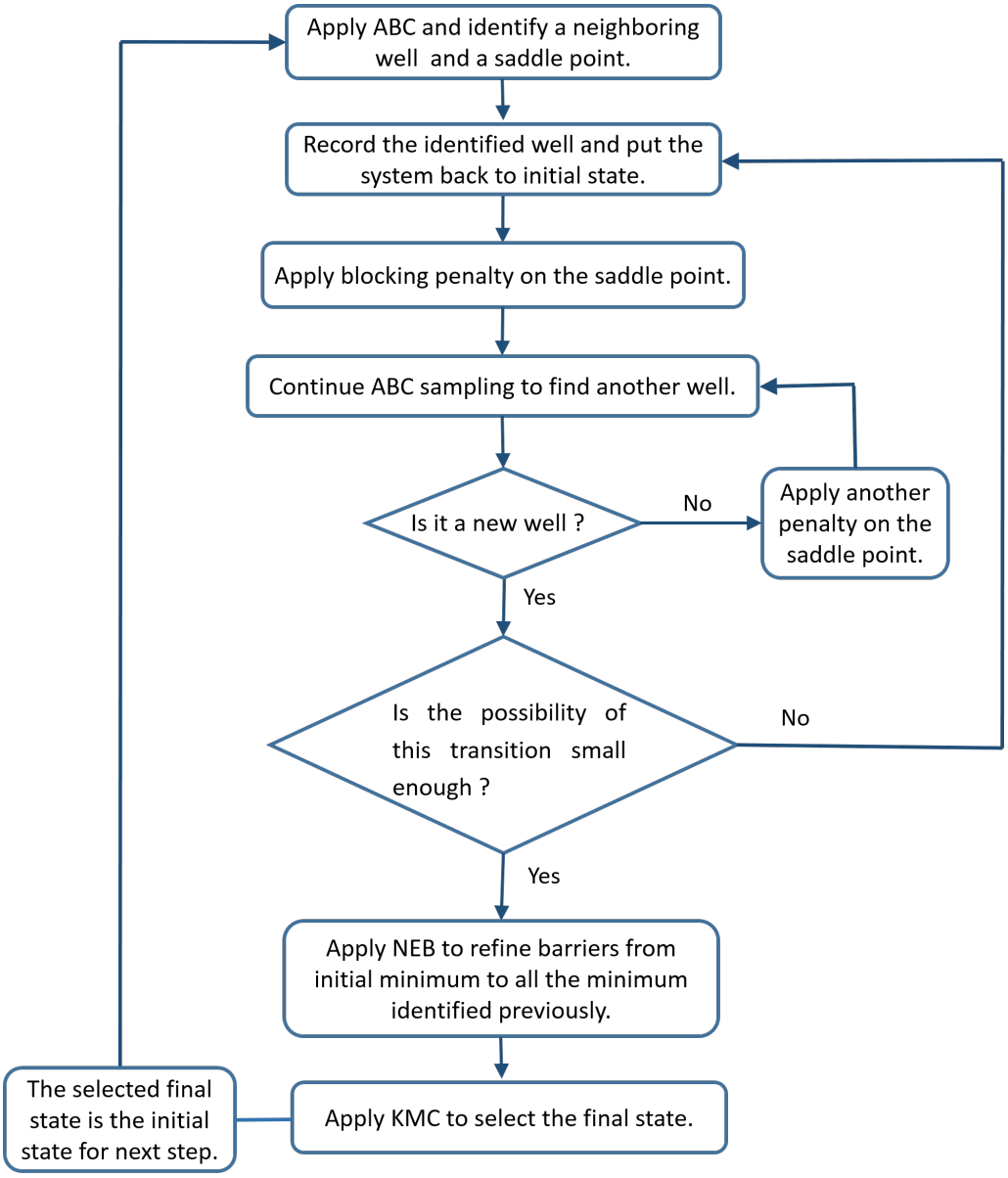

Figure 2.4: Algorithmic flowchart of method 3 (ABC-E).

We can rewrite Eq. (2.6) as

$$\dot{\gamma} = \dot{\gamma_0} \exp\left[-\frac{Q^*(T)}{k_\mathrm{B}T}\right]. \tag{2.8}$$

Eq. (2.8) thus plays the essential role of being a physical link between the SLME trajectories and the strain rates from MD to experimental values, which depends on only a single unknown temperature-dependent prefactor $\dot{\gamma_0}(T)$.

The connection between energy barriers, the PES, and enabling the study of atomistic systems at slow, constant strain rates is illustrated in Figure 2.5, and its connection to the way in which deformation is applied experimentally to structures can be understood as follows. Experimentally, constant strain rate loading is performed by deforming the structure, and then waiting a certain amount of time before applying the next load increment, during which the system is able to relax. For high strain rate loading, the relaxation time given to the system before another deformation increment is applied is minimal. Thus, the system has only a small amount of time to explore its PES, implying that it will only be able to cross small energy barriers Q^* between each deformation increment. In contrast, for slow strain rate loading, the system has more time to explore its PES between loading increments, and thus may be able to climb over larger energy barriers Q^*. The ability to cross over large energy barriers Q^*, and thus access slow, experimentally-relevant strain rates is made possible by the development of the ABC-SLME algorithm for efficient PES exploration [46].

The method can be detailed, as illustrated in Figure 2.5 as:

i Begin from a relaxed structure with strain γ_n;

ii Apply a strain increment $\Delta\gamma$;

iii Minimize the structure using conjugate gradient energy minimization while keeping the strain fixed. The system is then in the state γ_{n+1}^{cg};

iv Starting from the minimized state γ_{n+1}^{cg}, ABC-SLME is used to determine the potential energy tree structure as shown in Figure 2.5. The tree structure is truncated to only enable energetic transitions below Q^*, as shown in the green box in Figure 2.5.

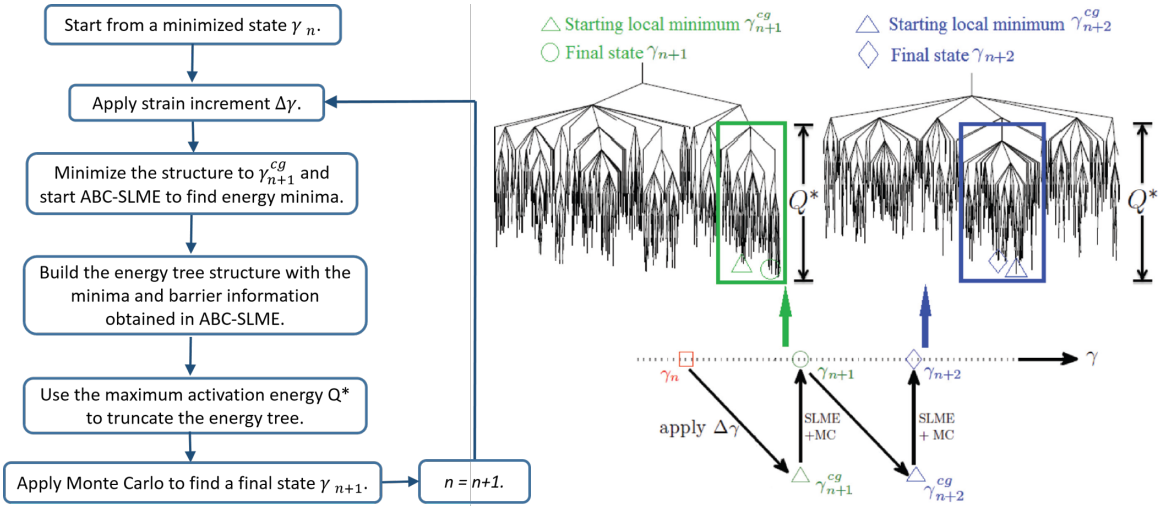

Figure 2.5: Algorithmic flowchart of the constant strain rate approach of Cao et al [2, 3]. Reprinted with permission from ref. [2].Copyright (2013) by the American Physical Society.

v A Monte Carlo algorithm is employed to find the most likely equilibrium configuration (γ_{n+1}), at which point the algorithm repeats itself until a desired amount of strain has been applied to the system.

It is important to note that the PES is strain-dependent, and thus changes after each strain increment is applied. This is captured in this method as shown in Figure 2.5, by repeating the PES exploration after each new strain increment is applied.

2.2.5 Method 5: Strict Strain-rate Controlled ABC

An alternate approach to applying a constant strain rate to an atomistic system was recently proposed by Fan *et al.* [4]. The steps in this approach, as outlined in Figure 2.6 are:

i Choose a desired strain rate($\dot{\varepsilon}$);

ii For a given strain (ε_i), the current PES is sampled by ABC and a neighboring energy basins is identified;

iii NEB is then used to accurately calculate the energy barrier connecting the two energy wells;

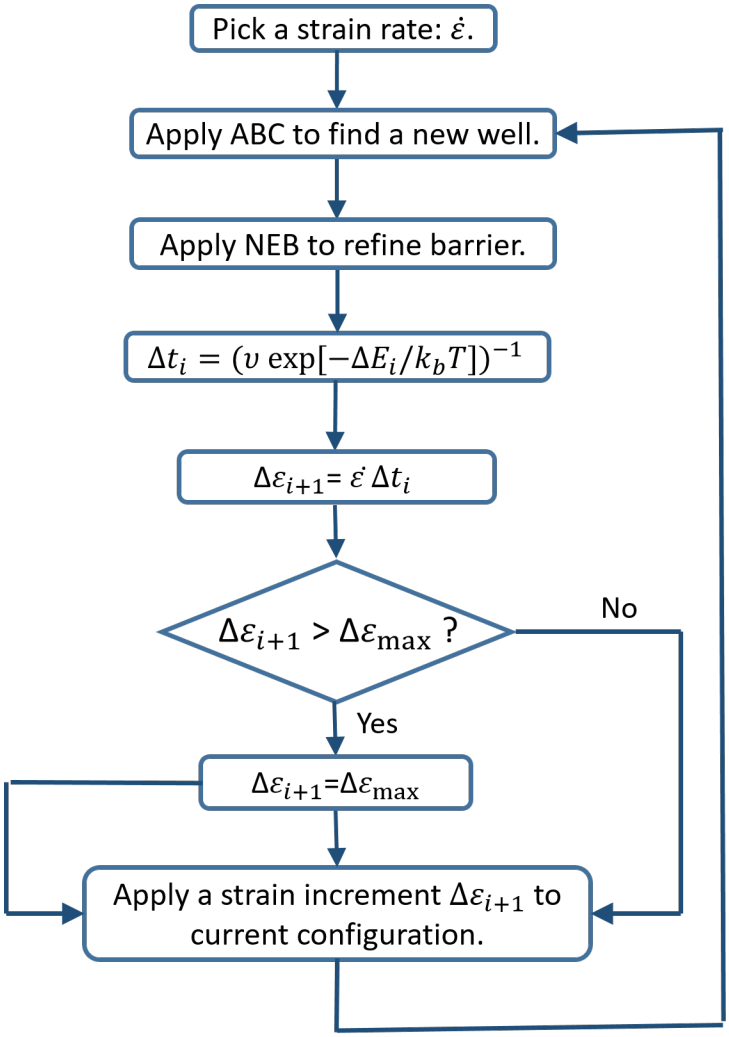

Figure 2.6: Algorithmic flowchart for method 5 [4].

iv TST is used to calculate the transition time (Δt_i) between the initial and final states using Equation (1.1);

v The transition time (calculated in the previous step via Eq. (1.1)) is multiplied by the prescribed strain rate $\dot{\varepsilon}$ to find the corresponding strain increment $\Delta\varepsilon_{i+1} = \dot{\varepsilon}\Delta t_i$;

vi Apply the strain increment ($\varepsilon_{i+1} = \Delta\varepsilon_{i+1} + \varepsilon_i$) to the system and go back to step II.

It should be noted that the strain in method 5 is being imposed on the system in discrete steps of variable magnitude depending on the height of the energy barrier that is found, and thus multiple PES' are identified rather than a single one. As discussed by Fan *et al.* [4], errors could emerge if the calculated strain increment $\Delta\varepsilon$ is too large. This is because, in

essence, the calculation steps are reversed from method 4 in that the strain increment is calculated based on the energy barrier that is crossed, rather than finding the new energy barrier based on the specified strain increment. Because of this reversal, only small strain increments can be applied to the system. Using increments that are too large would lead to errors because of the corresponding changes to the underlying PES.

Thus, because method 5 is restricted to smaller strain increments, it is more computationally expensive than the approach in method 4. This is not particularly problematic at fast, MD-accessible strain rates, but can introduce computational challenges at smaller strain rates, due to the fact that as seen in Equation (1.1), crossing larger energetic barriers ΔE would lead to very small time increments Δt, which means that many strain increments are needed to deform the system an appreciable amount for slower strain rates. However, this approach ensures that the strain increment applied in the next step fits the defined strain rate.

On the other hand, method 5 is likely to be more accurate in its calculations of time than method 4 for two reasons. First, the use of NEB in method 5 results in accurate calculation of the height of the energy barriers that are crossed, which leads to more accurate calculations of the time spent climbing each energy barrier, as the NEB was not used by Cao *et al.* [2, 3] in their development of method 4. Second, the strain increments are calculated based on the prescribed strain rate, such that the strain rate is accurately controlled.

An additional point to note is that both methods 4 and 5 currently assume that the prefactor that is used in Equation (1.1) is a constant that is independent of strain. This is likely to cause some errors in the strain rate simulations, as other researchers have shown that the prefactors are not constant, and in fact can be calculated directly from information that can be obtained during the PES exploration. Such work has been performed recently by Wales' group [65, 66].

To conclude this section, in our opinion no approach is at present clearly superior than another in dealing with long timescale problems. Furthermore, physical intuition about the problem of interest is clearly beneficial to both using and understanding the results obtained. In the next section, we give examples of recent studies based on the ABC approach that deal with various long timescale problems.

2.3 Applications of ABC—a Review of Some Representative Case Studies

After its introduction in 2009, the initial applications of the ABC method were in the study of the viscosity of two types of supercooled liquids, SiO_2 and a binary Lennard-Jones (BLJ) system [41, 42]. Soon thereafter, Lau *et al.* [67, 68] applied this approach to study the deformation in solids under constant strain mechanical loading. These initial efforts were reviewed in a recent review article [16]. We will focus on more recent examples that are predicted on the slow strain-rate methodologies described in previous section.

2.3.1 Applications of Method 1: Diffusion and Grain Boundary Sliding

Sharma and co-workers [1, 5] used method 1 described in Section2.2 to address two problems: diffusion in amorphous materials and grain boundary sliding. Diffusive transport of Li-ions in the silicon anode is one of the key mechanisms that controls the deformation during lithiation, the rate of the charge-discharge cycle, and eventual mechanical failure. The atomistic mechanisms underpinning diffusive transport of Li-ions in amorphous silicon are, however, poorly understood. Conventional molecular dynamics, if used to obtain atomistic insights into the Li-ion transport mechanism, suffers from several disadvantages: in particular, the relaxation times of Li ion diffusion in many of the diffusion pathways in amorphous Si are well beyond the short time scales of conventional molecular dynamics.

Yan *et al.* [1] studied Li diffusion in both amorphous (Figure 2.7) and crystalline (not shown in the figure) silicon matrix. These simulations were performed by implementing the ABC algorithm into the open-source atomistic simulation code LAMMPS [69, 70] such that the well-developed parallel computing capabilities and extensive interatomic potential database of LAMMPS could be employed in the ABC PES exploration, and the diffusion coefficients of Li in both crystalline and amorphous Si were evaluated. For crystalline Si, the diffusion pathway and diffusion coefficient matched prior density functional theory (DFT) calculations. For amorphous Si, after ABC sampling, 257 minima were found. NEB calculations between every two minima were carried out and a 257×257 barrier matrix which contains the energy barrier between all pairs of local energy minima was generated,

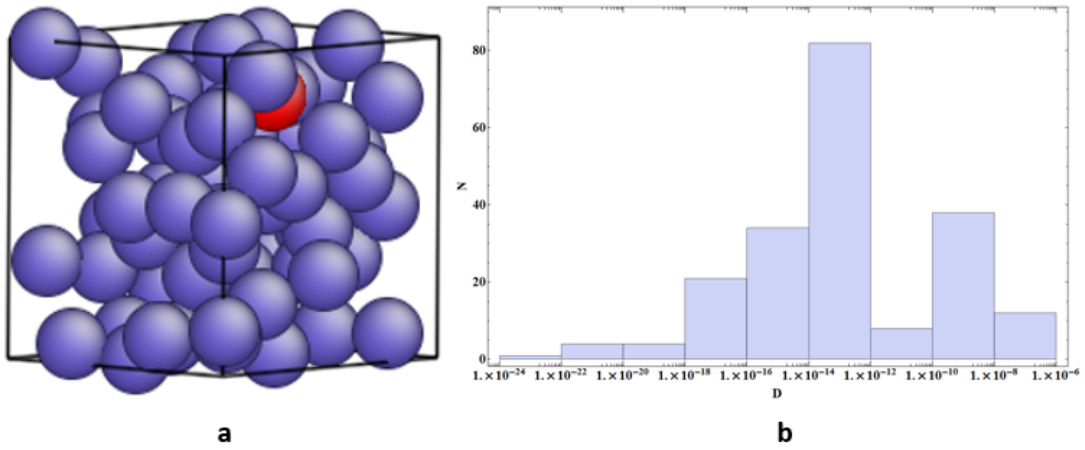

Figure 2.7: a) Diffusion of a Li atom in a Si matrix; b) Resulting diffusion coefficient distribution. Reprinted from [1] with permission from Elsevier.

after which KMC was applied to find the most probable diffusive pathway at 300 K [1]. The most probable diffusive pathways naturally emerge from this approach, and the diversity of diffusivities obtained in experiments can be replicated, as shown in Figure 2.7 b.

Grain boundary sliding is the key deformation and damage mechanism for high temperature deformation of crystalline materials impacting, thus, applications ranging from nuclear reactors to aircraft. Despite decades of research, both theoretical and experimental, a definitive atomistic understanding of this phenomenon has been elusive. To date, there is only speculation regarding the constitutive behavior of grain boundary sliding. Clearly, for such a rate-dependent process, MD is of limited use and while the overall creep behavior can be determined experimentally, the specific constitutive response of grain boundary sliding appears to be unknown. Gouissem et al. [5] applied method 1 to study grain boundary sliding in a bi-crystal under constant stress with the objective of developing physically reasonable constitutive laws based on atomistic simulations. In particular, that work aimed to answer important questions such as (i) is there a threshold stress for grain boundary sliding? (ii) what is the form of constitutive law for grain boundary sliding? The simulation setup is shown in Figure 2.8 a, where a constant shear stress is applied to the moving zones of an Al bi-crystal. After the ABC sampling process, NEB and KMC were applied to obtain the most realistic mode of deformation, after which h-TST was used to calculate the transition time. From the grain boundary displacement and transition time, the corresponding grain

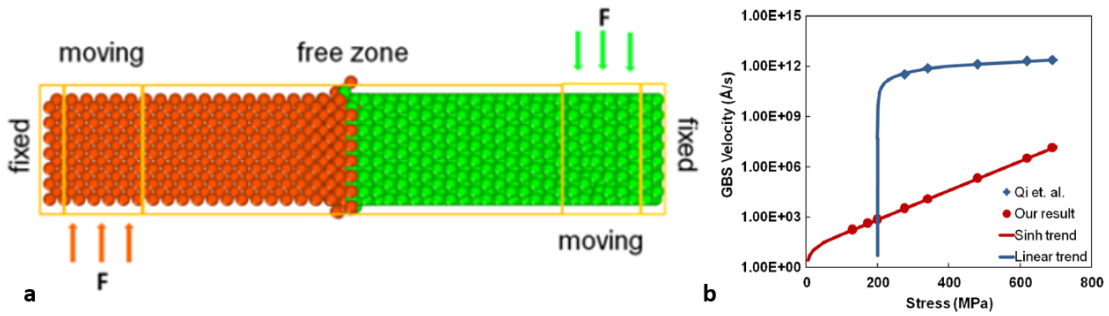

Figure 2.8: a) Grain boundary sliding system set up; b) Grain boundary sliding constitutive law; Reprinted from [5] with permission from Elsevier.

boundary sliding velocity was evaluated. Thus, as Figure 2.8 b shows, the grain boundary sliding velocity can be obtained as a function of applied shear stress. The key conclusion of that work, as amply demonstrated in Figure 2.8 b, is that slow strain rate ABC results and high strain rate MD results give very different sliding rates as a function of applied shear stress. Specifically, it was deduced that the grain boundary sliding constitutive law has a hyperbolic sine character and is highly non-Newtonian.

In both of these studies, ABC, in conjunction with a range of techniques, including NEB, KMC, and h-TST, were used to provide mechanistic details of atomistic deformation that cannot be obtained from classical MD simulations.

2.3.2 Applications of Method 2: Force-Induced Protein Unfolding

For biologically-related problems, such as clamping force-induced protein folding and unfolding, it is a significant challenge for MD simulations to capture the entire unfolding process at experimental time scales. Because of this, the MD simulations of protein unfolding typically occur at clamping forces that are significantly larger and time scales that are significantly shorter than those seen experimentally. Because of this discrepancy in simulated and experimental time scales, atomistic resolution of the unfolding pathways and intermediate configurations that can directly be compared with experiments are generally lacking.

To this end, Park and co-workers [6, 54, 55] have applied method 2 of Section 2.2 to study force-induced unfolding of the proteins ubiquitin, prion, and GFP. To illustrate the

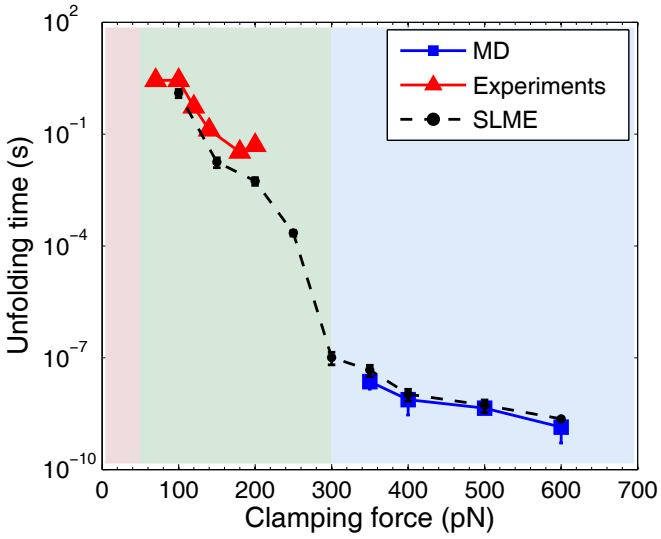

Figure 2.9: Unfolding time as a function of the clamping force for ubiquitin as obtained experimentally, using the ABC-SLME method, and also steered MD simulations [6].

utility of this approach, we focus the present discussion on the unfolding of ubiquitin [6].

Figure 2.9 shows the unfolding times for ubiquitin as measured experimentally, and calculated using both method 2 as described above, and also steered MD (SMD) simulations. Importantly, Figure 2.9 shows that the experimentally measured unfolding times are on the order of seconds, using clamping forces that are 200 pN and smaller. As can be seen, the SMD simulations are only able to simulate timescales up to about 10^{-7} s, or the microsecond time scale. In contrast, the ABC-SLME simulations are able to access both the high and low clamping force regimes, and agree well with both the high force SMD simulations, and the low force experiments. Most importantly, the ABC-SLME simulations capture the experimentally measured unfolding times of seconds when the clamping forces decrease below 200 pN. The ABC simulations also revealed new unfolding mechanisms and intermediate configurations that were not predicted experimentally, and revealed that the intermediate states were likely not observed experimentally because their lifetimes are about two orders of magnitude smaller than the experimental temporal resolution [6].

2.3.3 Applications of Method 3: Diffusion of Point Defects in HCP Zr

Fan and coworkers [24] adopted method 3 of Section 4 (ABC-E) to study the anisotropic diffusion of point defects in HCP Zr. ABC-E allows the sampling of multiple transition pathways from a given minimum. Combined with on-the-fly KMC, Fan *et al.* demonstrated multiple migration mechanisms for both interstitials and vacancies. They demonstrated that the self-interstitial atom diffusion kinetics show a maximum anisotropy at intermediate temperatures (400-700K).

Fan *et al.* also performed an interesting and direct comparison with ART, to determine the respective capabilities of ABC-E and ART in finding low energy saddle points. They did this through studying vacancy hopping in HCP Zr, where all of the 12 pathways are known *a priori*. In doing so, they found that ABC-E was able to both predict the correct order of all 12 pathways in terms of energetic preference, but also do so at much lower computational expense than ART, which was able to capture 10 of the 12 different pathways, thus demonstrating the capability of the ABC-E method as a computationally efficient importance sampling approach.

2.3.4 Applications of Method 4: Strain-Rate and Temperature-Dependent Deformation Mechanisms in Amorphous Solids

After developing method 4 as described in the previous section, Cao *et al.* studied strain-rate and temperature effects on the shear transformation zones (STZs) in two-dimensional [59] and three-dimensional bulk amorphous solids [3], as well as on surface shear transformation zones in two-dimensional finite thickness amorphous solid films [60]. The structure and properties of STZs is important to study because they are the unit carriers of plasticity in amorphous solids [71], playing a similar role as dislocations in crystalline solids.

One of the key findings of these works is shown in Figure 2.10. In (a), the deformation map for the two-dimensional amorphous binary Lennard-Jones solid is shown as a function of strain rate and normalized temperature, where the MD strain rate corresponds to 10^{-5}, and room temperature corresponds to about 0.3 T_g, where T_g is the glass transition tem-

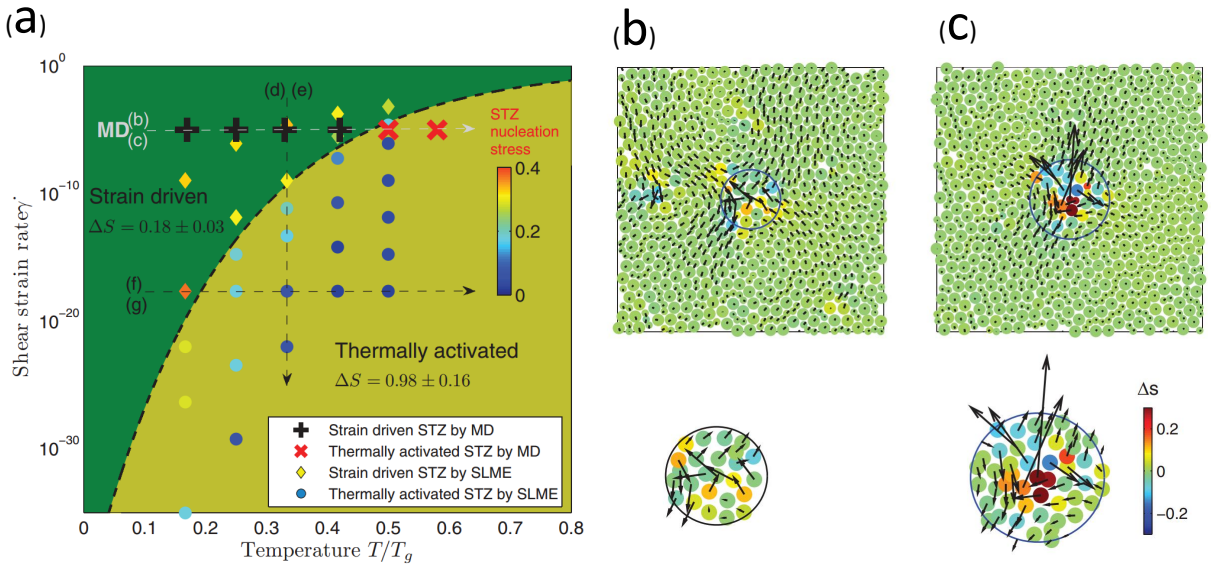

Figure 2.10: 2D bLJ strain-rate and temperature-dependence of deformation mechanism. Reprinted with permission from ref. [2].Copyright (2013) by the American Physical Society.

perature. As can be seen in (b), at room temperature and high (MD) strain rates, the STZs exhibit volume preserving, shear deformation. In contrast, as the strain rate drops about 10 orders of magnitude, corresponding to experimentally-accessible, the characteristics of the STZ change markedly. Specifically, the STZ area increases about 33%, its displacement field decays much more rapidly in space, less stress is needed to nucleate the STZ, its characteristic quadrupolar symmetry is lost, and perhaps most interestingly, the deformation mechanism inside the STZ changes from shear to tension [59]. This example illustrates the powerful and interesting predictions of fundamental mechanical properties that can be made if slower strain rates can be used in atomistic computation.

2.3.5 Applications of Method 5: Strain-Rate-Dependent Mechanical Response of Metals

Method 5 for applying a constant strain rate has also been used in multiple applications. In the work in which method 5 was developed, Fan *et al.* [4] studied the mechanisms of dislocation-defect interactions in HCP Zr for shear strain rates ranging from $\dot{\epsilon} = 10^{-6}$

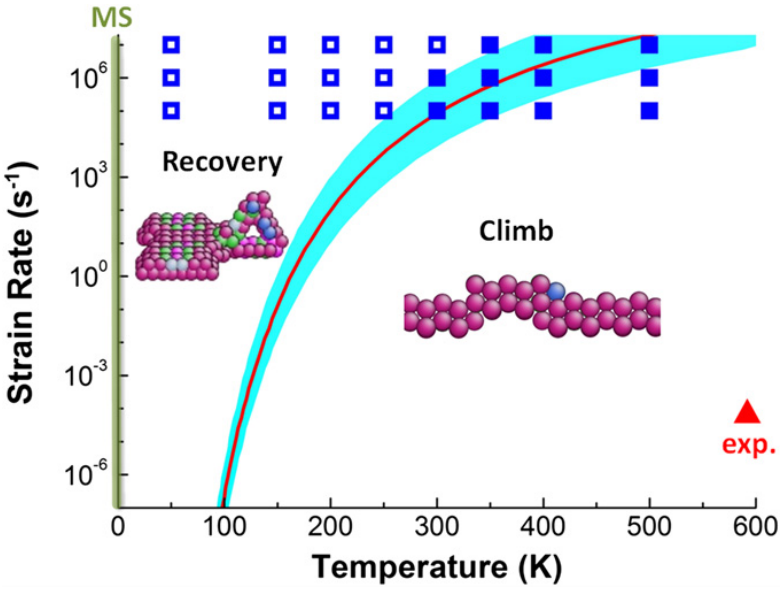

Figure 2.11: Strain-rate and temperature-dependence of recovery and climb mechanisms in dislocation-cluster interactions in HCP Zr; reproduced with permission from ref. [4].

s^{-1} to $\dot{\epsilon} = 10^6$ s^{-1}. In doing so, as shown in Figure 2.11, they found a novel strain-rate-dependent trigger mechanism. Specifically, at high strain rates and low temperature, edge dislocations and SIA clusters were found to exhibit a recovery mechanism, while at low strain rates and high temperature a climb mechanism was observed. The high strain rate deformation mechanism was confirmed by classical MD simulations, while the low strain rate response is a new observation. This work is an example of how these slow strain rate atomistic methods yield new insights into the strain-rate-dependent deformation mechanisms in different materials.

Using a simple model of a metallic nano-pillar that is often the subject of experimental works, Yan *et al.* [7] attempted to circumvent the time-scale bottleneck of conventional MD and provide novel physical insights into the rate-dependence of mechanical behavior of nanostructures. Inspired by the approach reported in Ref. [4], Yan *et al.* [7] modified the approach described in method 5, and applied it to a study of Ni nanoslab compression. In the work of Fan *et al.* [4], ABC was used to find a single new local energy minimum. In contrast for Yan *et al.* work [7], ABC sampling was continued until multiple local energy minima were found, at which point NEB was utilized to accurately calculate the energy

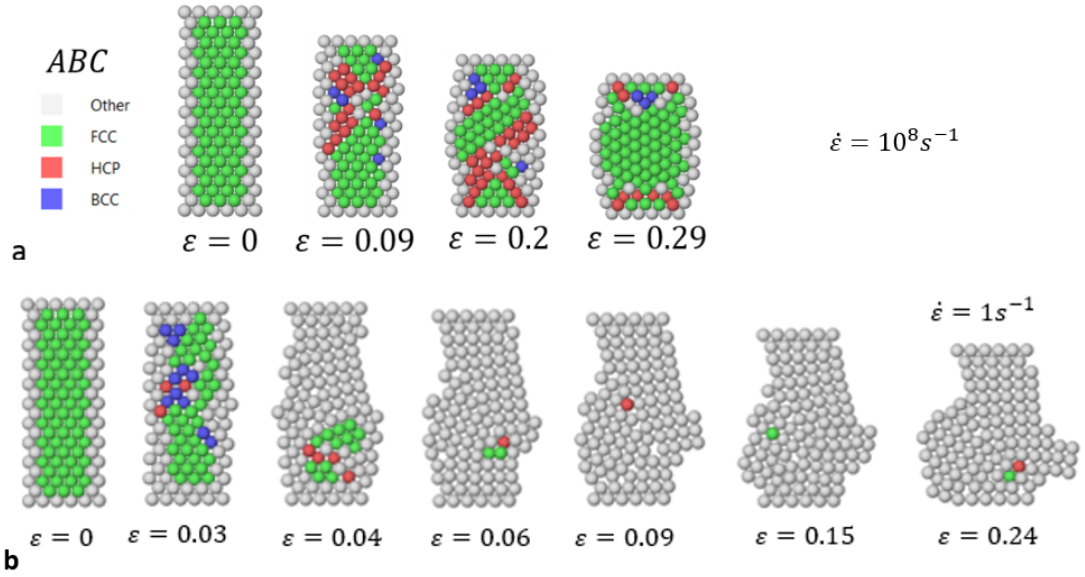

Figure 2.12: Ni compression under different strain rate. (Top): fast, MD-like strain rate; (Bottom) slow, experimentally-relevant strain rate. Reproduced with permission from ref. [7].Copyright (2016) American Chemical Society.

barriers connecting the initial energy minimum to all the possible the final configurations identified by ABC. KMC was then used to select the transition pathway, and h-TST was used to calculate the transition time (Δt) between the initial and selected final states.

The study of Ni nano-slab compression focused on investigating the deformation behavior and mechanisms under both experimentally-relevant (slow) and MD (fast) strain rates. While the high-strain rate deformation proceeds in an unremarkable manner, where the nano-slab shortens its length along with the formation of an expected defect sub-structure, the slow-strain-rate results, which are relevant to most applications and laboratory experiments, exhibit a dramatically different behavior. Specifically, liquid-like deformation at slow strain rates is observed, as shown in Figure 2.12. *In situ* experiments [72] appear to qualitatively confirm the observations that nanostructures, indeed, are more likely to exhibit the deformation pattern captured with the slow-strain-rate time-scaling approach in this research.

3 Chapter 3: Atomistic Insights into Li-ion Diffusion in Amorphous Silicon

Rechargeable Li-ion batteries are a critical part of the future energy storage needs in a broad range of applications: portable electronics, transport, power grid among others. Silicon (Si) is one of key materials being pursued for consideration as an anode material. The ensuing (theoretical) charge capacity is more than an order of magnitude higher than carbon-based anodes. During the charging and discharging process, Li-ions migrate from one electrode via the intervening electrolyte and insert and diffuse in the opposite electrode. Due to the high Li capacity of the Si anode, the insertion and diffusion of Li ions are accompanied with a rather large (nearly four-fold) volumetric swelling and the consequent generation of mechanical stresses. Fracture, loss of structural integrity and the irreversible capacity loss that consequently follow are mainly attributed to swelling induced mechanical stresses. Significant loss of capacity is often seen after only a few charge-discharge cycles. The use of amorphous silicon, instead of its crystalline counterpart, is considered to offer several advantages. The atomistic mechanisms underpinning diffusive transport of Li-ions in amorphous silicon are, however, poorly understood. Conventional molecular dynamics, if used to obtain atomistic insights into the Li-ion transport mechanism, suffers from several disadvantages: the relaxation times of Li ion diffusion in many of the diffusion pathways in amorphous Si are well beyond the short time scales of conventional molecular dynamics. In this chapter, we utilize a sequence of approaches that involve the employment of a novel and recently developed potential energy surface sampling method, kinetic Monte Carlo (KMC), and the transition state theory (TST) to obtain a realistic evaluation of Li-ion diffusion pathways in amorphous Si. Firstly, for a given set of boundary conditions, the autonomous basin climbing (ABC) method is applied to determine the minima of the potential energy surface (PES). Secondly, nudged elastic band method (NEB) is employed on all the minima pairs that are obtained from the ABC algorithm – to obtain accurate barriers. In the third step, KMC is carried out to find the most probable pathway between the different PES minima. Finally, following the pathway, TST is used to calculate the transition time

between minima pairs. The time information is combined with mean square displacement between the two diffusion steps to extract the diffusivity of both crystalline and amorphous Si. Thus, the diffusive pathways are not a priori set but rather emerge naturally as part of our computation. We elucidate the comparative differences between Li-ion diffusion in amorphous and crystalline Si as well as compare our results with past studies based on other methods.

3.1 Introduction

Rechargeable Li-ion batteries are a critical part of the future energy storage needs in a broad range of applications: portable electronics, transport, power grid among others [73, 74]. Intense research is currently focused on understanding the basic materials science underscoring these energy storage devices to achieve high energy density storage and to mitigate the loss of capacity due to chemical and mechanical degradation [75, 73, 74]. Silicon (Si) is one of key materials being pursued for consideration as an anode material [76]. The ensuing (theoretical) charge capacity is more than an order of magnitude higher than carbon-based anodes [75, 77, 78]. During the charging and discharging process, Li-ions migrate from one electrode via the intervening electrolyte and insert and diffuse in the opposite electrode. Due to the high Li capacity of the Si anode, the insertion and diffusion of Li ions is accompanied with a rather large (nearly four-fold) volumetric swelling and the consequent generation of mechanical stresses. Fracture, loss of structural integrity and the irreversible capacity loss that consequently follow are mainly attributed to the swelling induced mechanical stress [79, 80]. Significant loss of capacity is seen after only a few charge-discharge cycles [81].

The use of amorphous silicon (a-Si), instead of its crystalline counterpart, is considered to offer several advantages. Experiments have shown that the amorphous alloys tend to cycle better than the corresponding crystalline phases [82, 83, 84]. These works have concluded that the mechanism underlying loss of capacity in amorphous anode materials is different from the crystalline phases. In crystals, following lithium insertion, intermetallic phases are formed that induce inhomogeneous volume expansion and cracking. Fracture inevitably leads to reduction of capacity [75]. Although the lithiation induced volume expansion

is found to be larger in amorphous materials [80], the deformation is *homogeneous*, and *reversible*; in sharp contrast to the crystalline phase behavior [82, 83]. Finally, c-Si converts to an amorphous Li-Si alloy phase during lithiation [85, 86, 87] which generates additional mechanical stresses that accompany the phase transition process [80]. In summary, there are several technologically relevant reasons to consider a-Si as a viable alternative to c-Si.

The atomistic mechanisms underpinning diffusive transport of Li-ions in a-Si are, however, not fully understood. Experimental studies of Li diffusion in a-Si matrix reveal a wide scatter in the diffusion constant: 1×10^{-10} to 1×10^{-14} $cm^2 s^{-1}$ [88, 89, 90]. The reported results are for diffusion of multiple Li-ion atoms. While more realistic, this prevents a "clean"understanding of the single Li-ion diffusion mechanism. A potential recourse is to use atomistic simulations to obtain the requisite insights. One such study was performed by Tritsaris et al. [91] which yielded several interesting insights. Density Functional Theory (DFT) based calculations were used to study the single Li-ion diffusion mechanism by postulating pre-determined Li-atom positions and diffusive pathways. They concluded that the rate of long-range Li diffusion in a-Si is comparable to the rate in c-Si. One of the limitations of the aforementioned study is that the Li-atom sites and diffusion pathways were *pre-determined*—based on physical intuition. There is no guarantee that those pre-set pathways are the actual (or the most probable) pathways. Alternatively, if one is willing to use empirical force-fields, conventional molecular dynamics (MD) may be used to address this problem. However, as is well known, classical MD (usually) can only handle time-scales of a few hundred to thousand nanoseconds [92]. Thus for slow processes, such as diffusion and creep, conventional MD is clearly not the best choice. In the present context, MD will fail to account for diffusion pathways that have relaxation times longer than hundred of nanoseconds.

In this work, we employ a sequence of methods to perform, at least from the time-scale viewpoint, realistic simulations that provide insights into Li -ion diffusion in both a-Si and c-Si. Our work is based on the recent success of a potential energy surface sampling approach—the so-called autonomous basin climbing (ABC) algorithm [15, 68, 93]). Our study adopts a similar starting point as Tritsaris et al. [91], however, instead of using MD, we employ the ABC approach for potential energy sampling, and then in conjunction with

kinetic Monte Carlo (KMC) and transition state theory (TST), we determine the most probable diffusion pathways and kinetics for a single Li atom in both a-Si and c-Si.

3.2 Approach and Simulation Details

An overview of our overall computational approach is depicted in Figure 1. Below, we briefly describe the four steps (3.1a - 3.1d) of our approach: (1) For a given set of boundary conditions, the ABC method is used to sample the potential energy surface (PES)—this determines the minima of the PES as well as the saddle points yielding thus the energy barriers between different local minima (3.1a). (2) As will be explained further in the next few paragraphs, the energy barriers obtained from ABC are approximate since the determination of the saddle points can be in error based on the resolution of the sampling approach. Accordingly, to extract accurate energy barriers, the nudged elastic band method (NEB) is applied to *all* the minima pairs that are obtained from the ABC algorithm (Figure 1b). This is a fairly tedious step e.g., if only 10 minima are identified by ABC, a 10 $\times$ 10 matrix of energy-barrier pairs needs to be calculated. (3) With the energy barriers in hand, KMC is used to find the most probable pathway between the different PES minima (3.1c). (4) Following the pathway provided in step (3), TST is used to calculate the transition time between two steps (3.1d). The time information is combined with mean square displacement between the two steps to extract the diffusivity.

Inspired by the time-scaling approach of metadynamics [18] the ABC algorithm was developed by Kushima ,Yip and co-workers [68, 15, 16]. In this approach, an energy minimized initial structure is activated by adding a penalty energy $\Phi_p^k(r)$ followed by subsequent relaxation. The penalty energy is in the form of a 3N gaussian penalty function:

$$\Phi_p^k(r) = \omega exp[-(r - r_{min}^k)/2\sigma^2], \tag{3.1}$$

centered at the minimum configuration r_{min}^k. The parameters ω and σ control the shape of the penalty function. Through repeated application of the penalty imposition and the relaxation process, the system is pushed to climb up the basin to a higher energy configuration.In this manner, the algorithm outputs the configurations that the system visits successively,

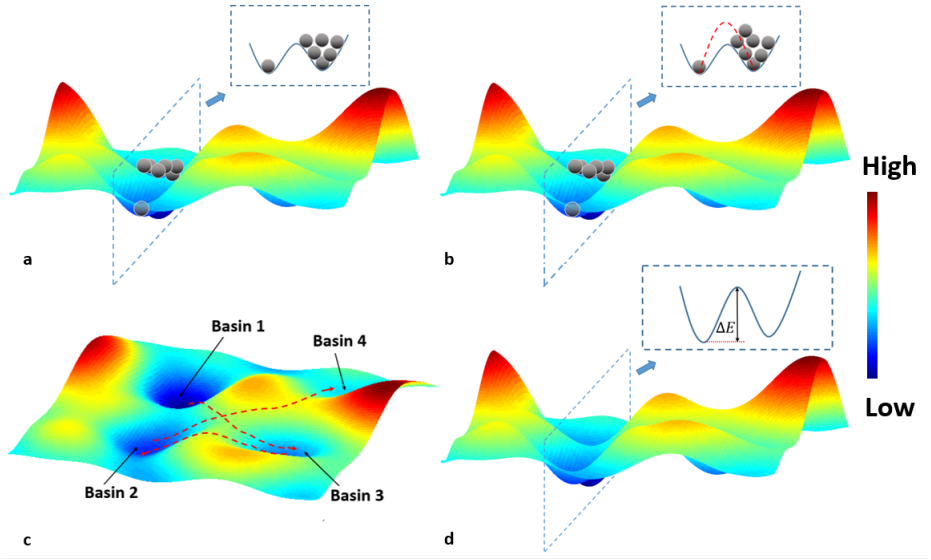

Figure 3.1: Illustration of the computational approach: a) ABC algorithm; b) The NEB approach is used to refine the calculation of the energy barrier; c) KMC then allows the determination of the most probable pathway; d) barrier energy ΔE is used in TST to calculate the rate constant.

moving from one energy basin to another through energy activation and relaxation steps as shown in 3.1a. We have implemented a parallel version of this algorithm in the LAMMPS software [69]. The size of the penalty should not be too large so that physically meaningful potential wells are not missed, nor too small that too many iterations are required to climb the barriers and obtain a *reasonable* sampling of the PES. Further details can be found in the following papers: [68, 15, 16]. Needless to say, the sampling of a system of even a few thousand atoms is computationally demanding. Recently, a rather interesting approach has been taken by Park and co-workers [46, 3], who have modified the ABC approach so that the system adapts the penalty function parameters through a *self-learning* process.

With a suitable penalty size and long-enough sampling time, in principle, the ABC algorithm can provide a "reasonable"approximation of the PES. Although the local minima are indeed captured accurately, unless the penalties are very small, the energy barriers are overestimated (3.1b red dash curve). Thus, to improve the accuracy of the energy barrier estimates, smaller penalties should be applied. However, this strategy is accompanied by a significant computational cost. Alternatively, the NEB [31, 94] method can be applied to the output of the ABC to obtain accurate energy barriers between the various minima

(3.1b).

In ABC sampling, the sequence of the identified local minima is physically irrelevant. For example, starting from the same initial configuration, a different ABC computation (with a different set of parameters) may identify a different sequence of the minima. To ascertain the most probable pathway that the system follows in going from one physical state to the other, we use KMC [30]. This method is used to calculate the corresponding possibilities for the system to cross every barrier (that has been identified) and to determine the most probable sequence for the system to cross the various energy barriers (3.1c). With all the barrier information calculated from NEB, the transition state theory is then applied to estimate the rate constant (3.1d) for each event (crossing a barrier):

$$k_{ij} \propto exp[-\Delta E/k_b T], \tag{3.2}$$

where k_{ij} is the rate constant for the single event, ΔE is the barrier energy calculated from ABC/NEB, k_b is Boltzmann constant and T is temperature. The rate constant divided by the summation of the rate constants of all possible events from the current state, yields the possibility of this single event. One of the possible transition is randomly chosen based on the relative possibilities. The way to realize the random choosing is to compare a random generated number in the range of (0,1] to an array of partial summation of the possibilities (3.2). Starting from the new state, with the corresponding rate constants in the rate matrix, the same action is taken to find the next transition state (3.2).

The simulation configuration chosen in this work is as follows. 3.3a and 3.3b show, respectively, the initial configurations for single Li-atom diffusion in a-Si and c-Si. The a-Si has 64 Si atoms—consistent with [91], to facilitate a subsequent comparison. To ensure meaningful comparison between the crystalline and amorphous configurations, the former has an identical ratio of the number of Si-Li atoms. The size of crystalline matrix is 10.887 Å×10.887 Å×10.887 Å. Two of the Si atoms are fixed to avoid rotation and translation in all directions, and periodic boundary conditions are applied to both systems. The atomistic force-field used in this work is the Modified Embedded Atom Method (MEAM) potential developed by Cui et al. [14].

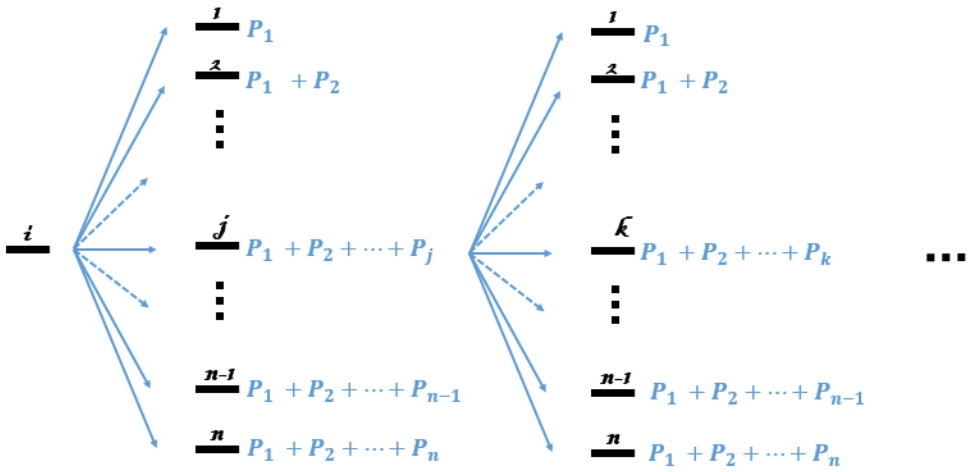

Figure 3.2: KMC algorithm: Starting from the ith state, a random number (r) in the range of (0,1] is compared with the partial summation of possibilities and it turn out $P_1 + P_2 + ... + P_{j-1} < r < P_1 + P_2 + ... + P_j$. Thus,the system will jump to state j. State j become the current state and same action will be taken with state j.

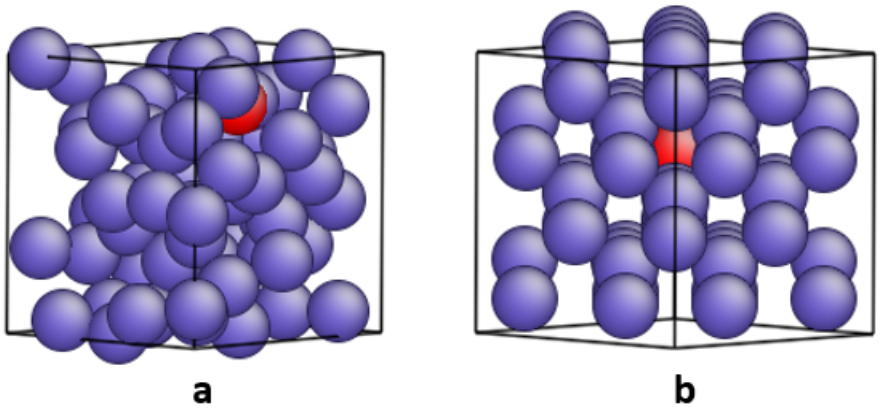

Figure 3.3: Initial simulation structure of Li diffusion in amorphous (a) and crystalline (b) silicon matrix.

The systems, crystalline and amorphous, are first equilibrated at 300K under NVT condition to ensure that the Li atoms occupy the energetically optimal site in the Si-matrix. ABC sampling is initiated from these initial configurations.

3.3 Results and Discussion

As alluded to earlier, in this study, we restrict our attention to monitoring the diffusion of a single Li atom in both crystalline and amorphous Si. We first discuss results for c-Si. For this particular case, we don't expect our results to differ from other approaches and accordingly, this is a useful benchmark analysis. For the Li-atom diffusion in the crystalline matrix, as shown in 3.4a, the captured possible Li sites are shown in red. The numbers on the atoms indicate the sequence of the sites captured in ABC. It is observed that all the possible Li sites are in the T_d positions which is consistent with Tritsaris' work [91]. The T_d site lies at a distance of b_o away from a Si atom in the direction opposite from one of its nearest neighbor Si atoms (b_o equals to the bond length of crystalline silicon matrix). The diffusion pathways and the energy barriers that are obtained from KMC are shown in 3.4b. The barriers between two sites are around 0.5 eV which is also consistent with the results reported by Ref. [91] and the corresponding diffusion coefficient of 5.01×10^{-12} $cm^2 s^{-1}$ agrees with the results in the literature. Based on this comparison, we conclude that the present method can reasonably capture Li diffusion in c-Si. In the following, we discuss our results for a-Si—the main focus of this work.

For amorphous system, different penalty size is used with $\omega = 2$ and $\sigma = 2$. After ABC calculations for Li in a-Si, a total of 260 minima are sampled. Among all these configurations, if any two state have Li-atoms positions that differ by<0.6 Å *and* if the energy barrier between those two states is less than the thermal fluctuation ($k_b T \approx 0.026$ eV), we consider them to be in the same potential well and one of them is removed from the minima list. After this paring down, 3 local minima are eliminated. NEB calculation is then carried out to provide a 257×257 barrier matrix which contains energy barrier between all the pairs. KMC algorithm is applied to find the most probable diffusive pathway. Unlike the crystalline case, the diffusion pathway and kinetics is strongly dependent on the initial site of the Li-atom diffusion. To obtained a deeper understanding of this, we carried out

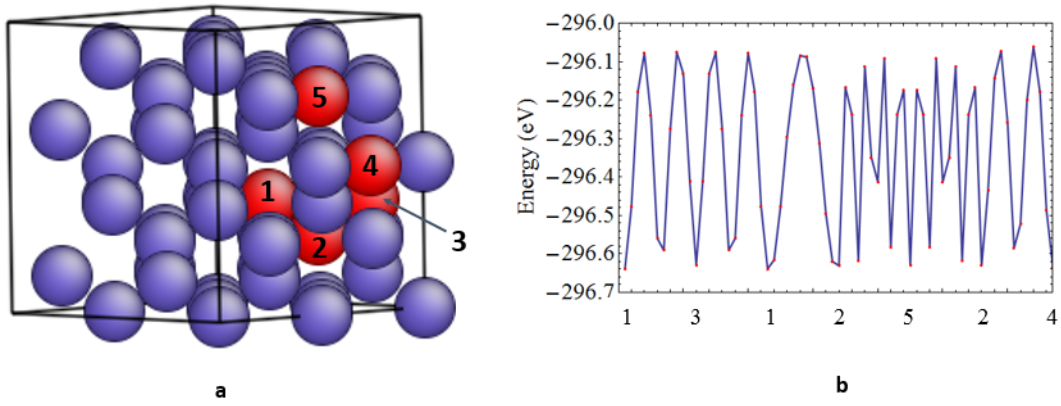

Figure 3.4: Diffusion path and corresponding barriers of single Li diffusion in crystalline Si matrix.

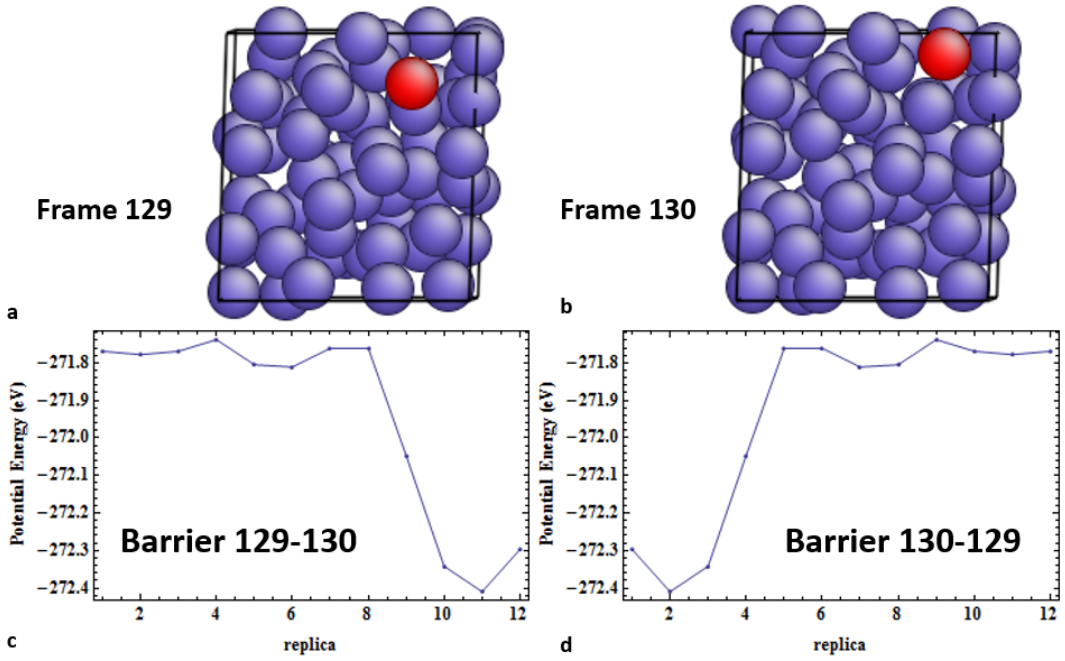

Figure 3.5: (a) Configuration of frame 129; (b) Configuration of frame 130; (c) NEB results of barrier from frame 129 to frame 130; (d) NEB results of barrier from frame 130 to frame 129.

257 KMC simulations starting from different basins and distinguish four scenarios:

(1) Scenario 1: Li atom diffuses a few steps and gets trapped in some wells—subsequently then shuttling back and forth among two or more wells. The reason for this phenomenon is that the barriers between these wells and other "outside wells"are significantly higher and the chances for the Li atom to diffuse out of the traps are low. Taking the states 129 and 130 as an example, in 3.4 a and b, the Li atom diffuses back and forth in these two sites, and the diffusion distance of Li atom is 2.03Å. The corresponding barriers are shown in 3.4 c and d with the value of 0.113 eV and 0.649 eV. Except for the barriers between state 129 and 130, the smallest barrier starting from states 129 and 130 are 2.606 eV and 2.211 eV. Applying Equation 3.2, it is found that the rate constant for barrier between state 129 and 130 are 0.013 and 3.11×10^{-11}, and the rate constant for the smallest "outside barrier"are 2.9×10^{-44} and 1.17×10^{-37}.

(2) Scenario 2: The Li atom is trapped between some wells but then after some iterations, is able to move to other basins.

(3) Scenario 3: The initial site is a "dead"site. By "dead site", here, we mean that the barriers from this site to others are higher than 1.2 eV which indicates that at room temperature (300K), the system requires longer than half a year to diffuse out of this well and the time it requires is much longer than usual charging and discharging time. Thus, we assume that if the barrier is larger than 1.2 eV, diffusion rate is slow enough to be physically irrelevant.

(4) Scenario 4: After a very short diffusive path, the Li atom ends up in a dead site. This case is also pointed out in the work of Tristsaris et al. [91], however their approach precludes the determination of the actual pathways.

To calculate the diffusion coefficient, we find the gradient of mean square displacement (R^2) versus time t and using the Einstein relation

$$D = \lim_{t \to \infty} (R_j - R_i)^2 / 6t. \tag{3.3}$$

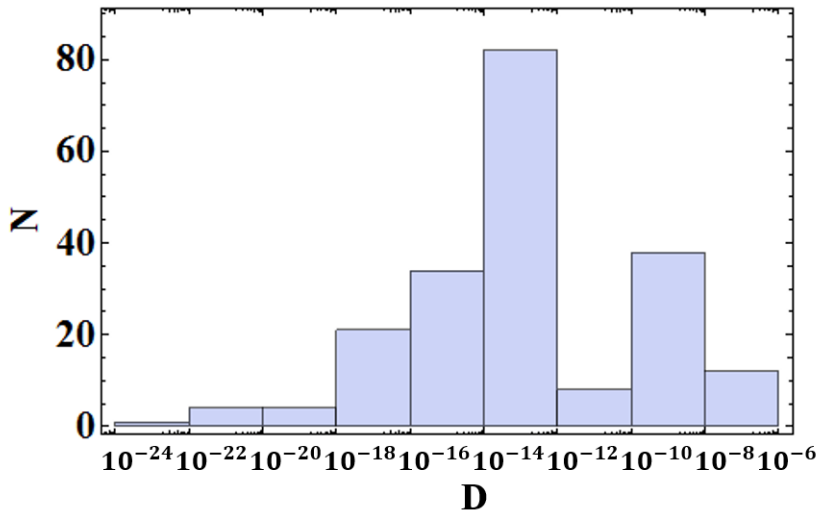

Figure 3.6: Distribution of diffusivities after KMC calculation.

The time t, is obtained from the transition state theory

$$t_{i-j} = (\nu exp[-\Delta E_{i-j}/k_b T])^{-1}, \tag{3.4}$$

where ν is the hopping frequency taken to be $10^{13} s^{-1}$. For scenario (1) and scenario (2), the diffusion coefficient is obtained based on 100 KMC iterations. For scenario (3), we assume that the diffusion will not happen. For scenario (4), we only collect data until the Li-atom diffuses to a dead-site. As a result, 204 diffusion coefficients (obtained from different initial sites) are shown in 3.5. As is evident from 3.5, the estimated diffusion coefficient exhibits a wide range of values: from $10^{-24} cm^2 s^{-1}$ to $10^{-6} cm^2 s^{-1}$. However, the preponderance of the distribution (around 80%) is in the range of 10^{-16} to 10^{-8} $cm^2 s^{-1}$. This range is a little bit larger than what has been reported in experiments: (10^{-14} to 10^{-10} $cm^2 s^{-1}$), and the possible reason is that in this work, we have focused on the diffusion of single Li atom as opposed to diffusion of multiple Li-atoms. It is worth emphasizing that, in 3.6, the slower diffusion rates cannot be captured by *conventional* molecular dynamics.

3.4 Summary

Understanding the kinetics of diffusive transport of Li atoms in amorphous silicon is an important first step to establish the relevant materials science for potential application of

this material as an anode in Lithium-ion batteries. The traditional atomistic approaches suffer from various limitations when dealing with physical phenomena that involve relaxation times longer than hundreds of nanoseconds and/or complex materials (such as amorphous) where reaction pathways are not necessarily intuitively obvious. In this work, we concoct together a series of computational atomistic approaches, the so-called autonomous basic climbing algorithm that allows potential energy landscape sampling, nudged elastic band, kinetic Monte Carlo and finally transition state theory to obtain insights into Li diffusion in amorphous silicon. The probable diffusive pathways naturally emerge from our approach and we are able to replicate the diversity of diffusivities obtained in experiments. The presented work, potentially, paves the way for *materials design* using the approach described herein.

4 Chapter 4: Time-scaling in Atomistics and the Rate-Dependent Mechanical Behavior of Nanostructures

Conventional molecular dynamics simulations enable the elucidation of an astonishing array of phenomena inherent in the mechanical and chemical behavior of materials. Unfortunately, current computational limitations preclude accounting for processes whose transition times exceed, at best, microseconds. This limitation severely impacts, among others, a realistic assessment of slow-strain-rate mechanical behavior. In this work, using a simple paradigmatical model of a metallic nano-pillar that is often the subject of experimental works, we attempt to circumvent the time-scale bottleneck of conventional molecular dynamics and provide novel physical insights into the rate-dependence of mechanical behavior of nanostructures. Using a collection of algorithms that include a recently developed potential energy surface sampling method—the so-called autonomous basin climbing approach, kinetic Monte Carlo, and others, we assess the nano-pillar mechanical behavior under strain rates ranging from 1 to $10^8 s^{-1}$. While our results for high-strain rate behavior are consistent with conventional molecular dynamics, we find that the response of nanostructures to slow compression is "liquid-like"and accompanied by extensive surface reconstructions.

4.1 Introduction

The mechanical behavior of nanostructures is of significant interest both from a basic-science viewpoint as well as for its increasing relevance in applications that range from next-generation electronics, sensors to biomedical technology [95, 96, 97]. This has inspired an exciting array of experimental studies that purport to understand how the mechanical behavior of nanostructures differ from bulk [98, 99, 100]. An often-used paradigm is to mechanically compress a nano-pillar and observe (*in-situ*) its deformation [101, 102, 103, 104]. Complementary to these experimental studies, extensive work has also followed on using *conventional* molecular dynamics (MD) to obtain insights into the mechanisms underpinning the mechanical behavior of nanostructures [105, 106, 107]. While the aforementioned modeling works have provided interesting insights, there is a fundamental limitation of

conventional MD methodology that precludes an assessment of material behavior over realistic laboratory-time-scales. Molecular dynamics can only handle time-scales of the order of, at best, a few microseconds. While this is adequate for understanding several physical, chemical and mechanical phenomena in materials, the inability to address long time-scales prevents an assessment of slow-strain rate mechanical behavior that is the norm in laboratory experiments and real-life applications. This shortcoming thus prevents an atomistically-faithful understanding of phenomena like creep, void nucleation, defect migration, microstructure evolution, corrosion and in general, most processes that are strongly *rate-dependent*.

In this letter, inspired by (at least the partial) success of some recent work on bridging time-scales c.f. [41, 4, 3, 1, 5], we employ a collection of algorithms that assess the mechanical behavior of two-dimensional nano-pillars[4]under strain rates ranging from 1 to $10^8 s^{-1}$. We note that conventional MD can only handle strain rates of $10^7 s^{-1}$ [108] and higher, while our goal is to understand what truly happens in nanostructures at rates comparable to those found in the laboratories and applications (i.e. strain rates comparable to $1 s^{-1}$). We choose a nickel nano-slab as the model material system although the goals of this letter are not to communicate insights into any one particular material but rather proffer broader physical conclusions that pertain to capturing rate effects with atomistic fidelity. Furthermore, another motivation for choosing this particular system is that in a recent work, Pattamatta *et. al.* [8] precisely studied this configuration using an approach that is quite different than ours and thus presents an opportunity for a constructive comparison.

4.2 Simulation Method

4.2.1 Model Description

Consistent with Ref. [8], one of our model systems is a 116 atom Ni nano-slab. The simulation layout is depicted in 4.1. The x-y dimensions are 12.5×35Å. The system is periodic in

[4]We will henceforth refer to these as "nano-slabs".

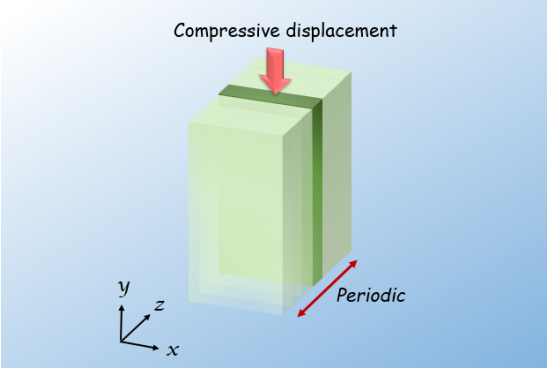

Figure 4.1: Schematic of the model studied in this work: compression of a two dimensional nano-pillar or a nano-slab at a given constant strain rate.

the z-direction–hence the label of "two-dimensional"nano-pillar[5]. The z-direction unit-cell length is 2.46Å Figure 4.1. Later, to investigate size-effects, we will also consider a larger system size. The top and bottom layers are constrained to apply compressive displacement. A compression with constant strain-rate is applied to the system in the y-direction. The Modified Embedded-Atom Method (MEAM) potential is used in all the calculations presented in this work [109, 110]. Further discussion on the effect of the choice of potentials can be found in Section 4.2.6.

4.2.2 General Overview and the Key Ingredients of the Time-scaling Approach

A brief synopsis of our approach and the key ingredients of the time-scaling approach used by us is depicted in Figure 4.2 and briefly described below. Further details of this approach, including a flow-chart of the algorithm, may be found in Sections .

(i) We first fix the strain rate at which we wish to perform the simulation. The strain is then applied to the system in very small discrete steps and we identify multiple potential energy surfaces (PES') corresponding to these very small strain steps. The PES during

[5]We remark that we are not solving a two-dimensional problem and some researchers may prefer the adjective "2.5 dimensional"to distinguish our model system from a real two-dimensional problem

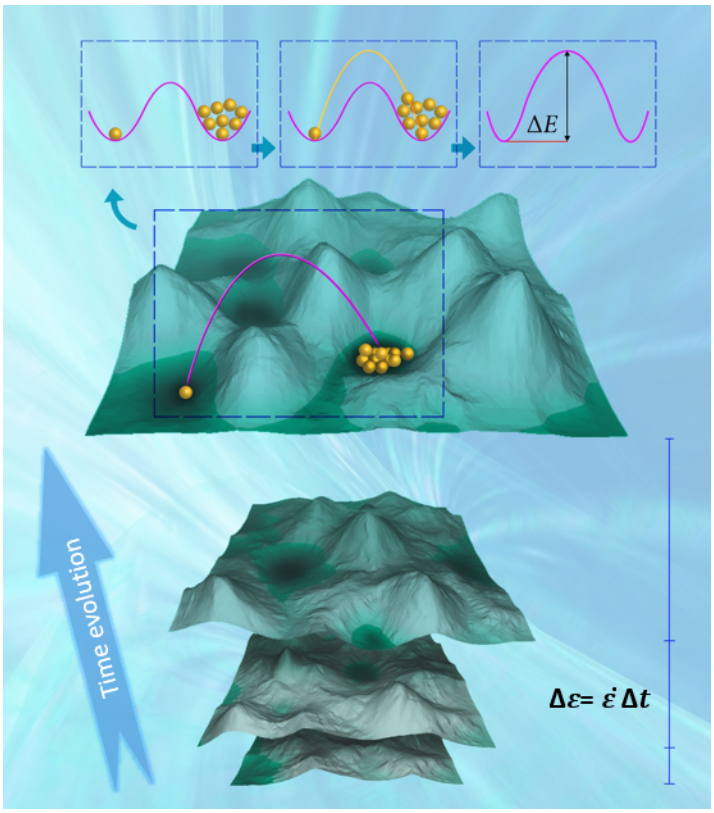

Figure 4.2: This figure describes the key ingredients behind the time-scaling approach used in this work. The corrugated surfaces represent the PES' under different strains identified by the ABC algorithm.

each small strain increment is identified by using the so-called autonomous basin climbing (ABC) algorithm described next.

(ii) *Sampling of the potential energy surface*: For a given set of boundary conditions (i.e. strain increment), the ABC algorithm [41, 16] is used to sample the PES. This determines the minima of the PES as well as the saddle points yielding thus the energy barriers between different local minima. The 3N-dimensional PES is quite complex indeed and Figure 4.2 is merely a schematic representation to provide intuition to the reader. The ABC algorithm was proposed by Kushima, Yip and co-workers [41, 16], and it has found success in a variety of contexts ranging from creep dislocation climb to void nucleation [68, 93, 111]. In this approach, an energy minimized initial structure is activated by adding a penalty energy $\Phi_p^k(r)$ followed by subsequent relaxation. Usually, the penalty energy is in the form of a Gaussian function:

$$\Phi_p^k(r) = \omega exp[-(r - r_{min}^k)/2\sigma^2], \tag{4.1}$$

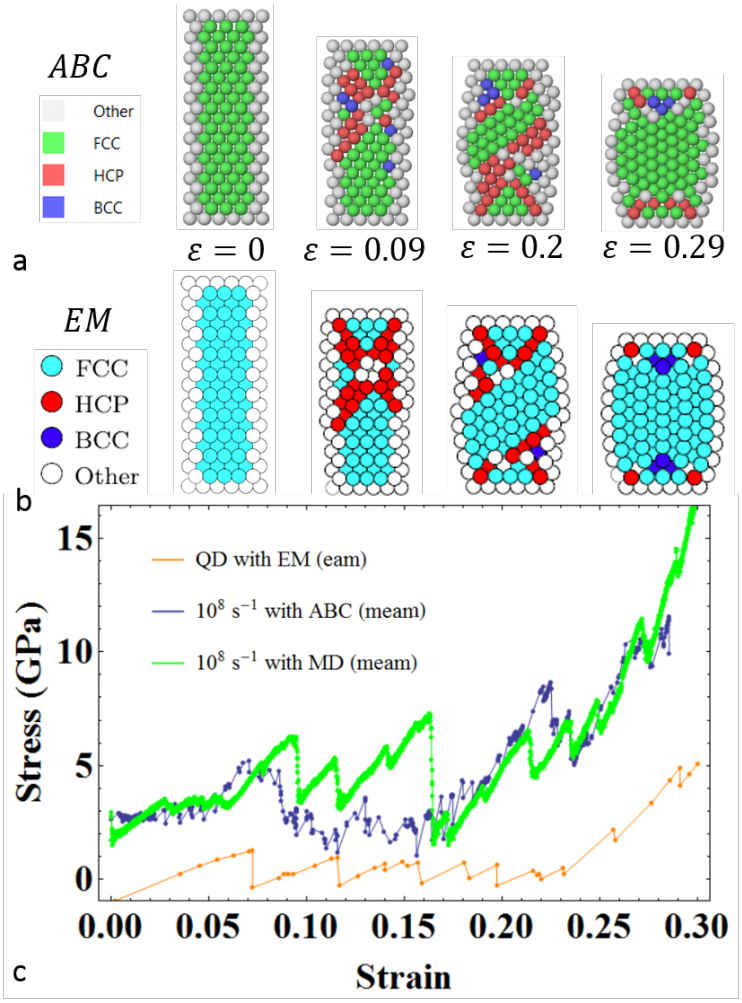

Figure 4.3: (a) High strain rate compression of Ni nano-slab using ABC and (b) the QD case of the EM approach from Ref. [8], are qualitatively similar. (c) Stress-strain behavior comparison between ABC, EM and conventional MD.

centered at the minimum configuration r^k_{min}. The parameters ω and σ control the shape and size of the penalty function. Through repeated application of the penalty imposition and the relaxation process, the system is pushed to climb up the basin to a higher energy configuration. In this manner, the algorithm outputs the configurations that the system visits successively, moving from one energy basin to another through energy activation and relaxation steps as shown in the left inset of Figure 4.2. We have implemented a parallel version of this algorithm in the LAMMPS software [69]. The size of the penalty should not be too large so that physically meaningful potential wells are not missed, nor too small that too many iterations are required to climb the barriers and obtain a "reasonable"sampling of the PES. Further details can be found in the following papers: [41, 16]. Needless to say, the sampling of a system of even a few hundred atoms is computationally demanding. Further details regarding the computational cost of our entire approach may be found in Section 4.2.5. Recently, Park and co-workers [46, 3], have modified the ABC approach so that the system adapts the penalty function parameters through a *self-learning* process.

(iii) *Minimum energy pathway for accurate determination of the energy barriers*: With a suitable penalty size and long-enough sampling time, in principle, the ABC algorithm can provide a "reasonable"approximation of the PES. Although the local minima are indeed captured accurately, unless the penalties are very small, the energy barriers are overestimated. Thus, to improve the accuracy of the energy barrier estimates, smaller penalties should be applied. However, this strategy is accompanied by a significant computational cost. Alternatively, the nudged elastic band (NEB) [31, 94], finite temperature string (FTS) [47] or other such methods can be applied to the output of the ABC to obtain the minimum energy pathway between the initial minimum and all the possible final minima identified in ABC sampling. (iv) *Kinetic Monte Carlo (KMC)*: In ABC sampling, the accumulated penalties push the system to a neighboring minimum and prevent its return to any prior minima that has already been visited. To select the most probable path a system may take starting from some initial minimum state to all the minima identified in ABC, we apply KMC [30]. More details about application of KMC is described in Section 4.2.4.

(v) *Transition State Theory (TST)*: With the barrier of the selected transition in hand,

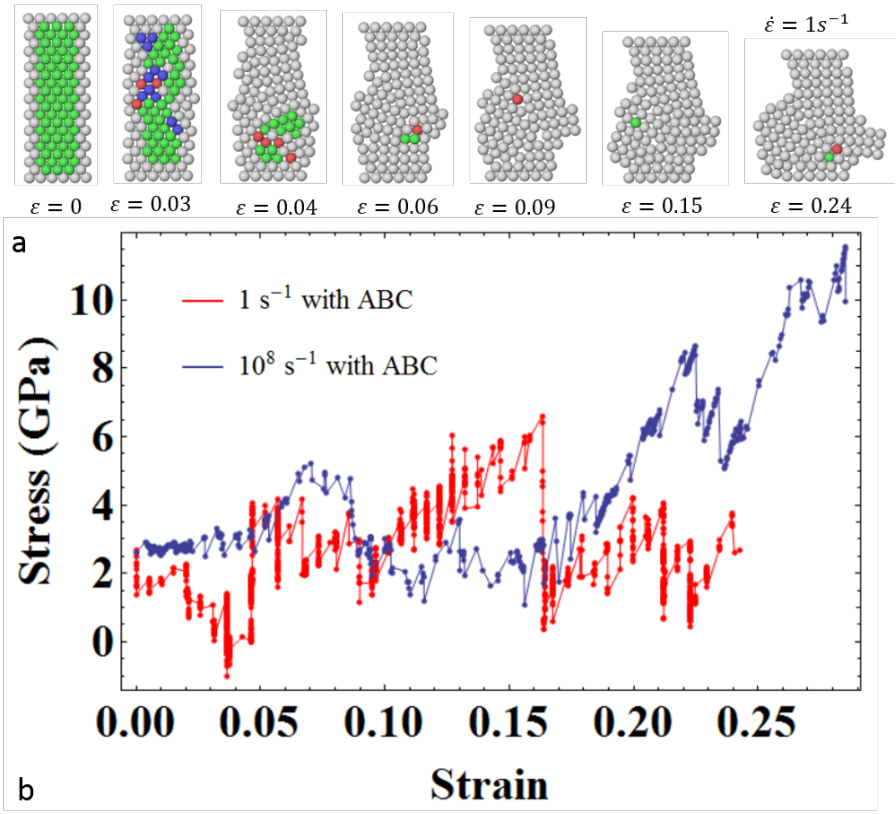

Figure 4.4: a) Structure evolution of compression Ni nano-slab at low strain rate; b) Comparison of stress-strain behavior at high/low strain rates.

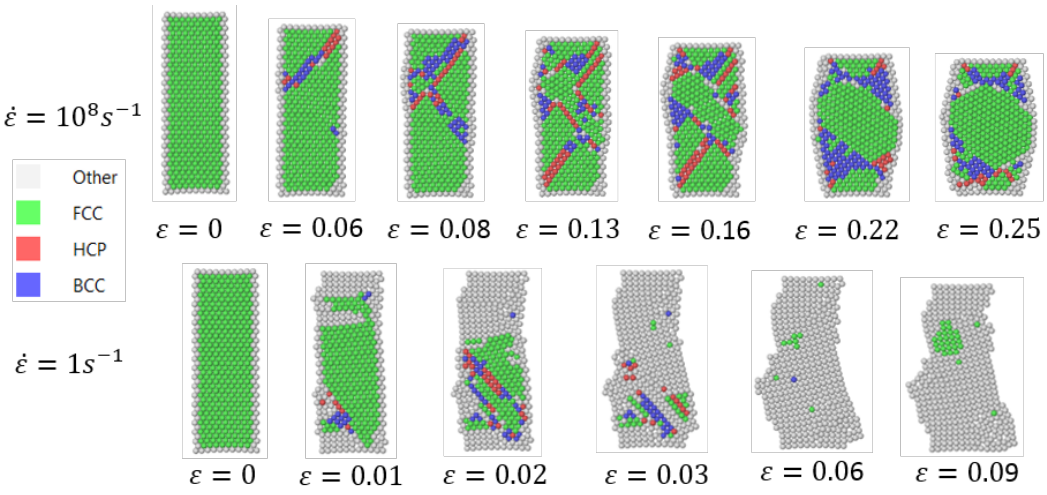

Figure 4.5: Structure evolution of larger Ni nano-slab under compression at high strain rate (top row) and low strain rate (bottom row).

TST can be applied to calculate the transition time. In this work (like many others), we have used the so-called harmonic approximation of the TST, which can be expressed as

$$\Delta t = (\nu exp[-\Delta E/k_b T])^{-1}. \tag{4.2}$$

In the equation above, ν is the hopping frequency taken to be $10^{13}s^{-1}$ and T is temperature(300K for this work). The reader is referred to an interesting study by Nguyen *et al.* [112] which illustrates the shortcomings of the harmonic TST. However, as will become evident in due course, numerical inaccuracy in the calculation of the precise time between events is not likely to impact the physical conclusions of this particular work since the time calculation is controlled through the way we impose the strain rate.

4.2.3 Remark on the Time-calculation and Imposition of Strain Rate

We implement a constant strain rate ($\dot{\boldsymbol{\varepsilon}}$) in the following way (as shown in the flowchart in Figure 2.6). Under a given strain, the current potential energy surface (PES) is sampled by ABC and multiple energy minima are identified. Then Nudged Elastic Band (NEB) is used to calculate accurate barriers from the initial well to all the possible final states identified in the ABC sampling. Kinetic Monte Carlo (KMC) is used to select a transition path and harmonic Transition State Theory (h-TST) is used to calculate the transition time between the initial and selected final states (more simulation details can be found in Section 4.2.4). Finally, the transition time multiplied by defined strain rate ($\dot{\boldsymbol{\varepsilon}}$) yields the strain increment for the next iteration through

$$\Delta \boldsymbol{\varepsilon} = \dot{\boldsymbol{\varepsilon}} \Delta t, \tag{4.3}$$

where Δt is transition time in each increment and it is calculated from h-TST. Then, the strain increment is applied to the system and a new round of ABC sampling (and the entire aforementioned process) is repeated.

We calculate the total time from the total deformation (strain $\boldsymbol{\varepsilon}$) and the constant strain rate ($\dot{\boldsymbol{\varepsilon}}$) we have defined through the relation $t = \boldsymbol{\varepsilon}/\dot{\boldsymbol{\varepsilon}}$. This should provide a fairly tight control over the transition time between minima if the strain increments are "small enough". In this work, to assure this, indeed such small increments (for example $\Delta\boldsymbol{\varepsilon} < 5 \times 10^{-3}$) were applied to the system during each iteration (strain increment).

4.2.4 Simulation Details

We have implemented a parallel version of ABC algorithm in the LAMMPS [69]. For each ABC sampling, 100 penalties are added to the system. Usually, 5-10 minima could be found. We assume all the minima found in ABC are the possible final states in the current PES. NEB with 12 replica is adopted to find the barriers between initial minimum and all the possible final states identified in ABC. The convergence criteria for NEB is 1e-8 eV for energy and 1e-6 eV/Angstrom for force. Either energy criteria or force criteria is satisfied on every replica, the NEB simulation will be terminated. Both ABC and NEB are applied directly to the potential energy landscape.

With the barrier energies in hands, we use harmonic transition state theory to estimate the rate constant for each event (crossing a barrier):

$$k_i \propto exp[-\Delta E_i/k_b T], \tag{4.4}$$

where k_i is the rate constant for the single jump from initial minimum to one possible final minimum, ΔE_i is the barrier energy calculated from NEB, k_b is Boltzmann constant and T is temperature (300K). The rate constant of single jump divided by the summation of all the rate constants calculated in current PES, yields the possibility of this single jump. One of the possible transition is randomly chosen based on the relative possibilities. The way to realize the random choosing is to compare a random generated number in the range of (0,1] to an array of partial summation of the possibilities [30].

The PES evolves with the strain—i.e., with each increment of the strain. At each increment, we have to choose a different penalty size in ABC sampling. For every iteration, due to the constraint of maximum strain increment, a maximum time variation ($\Delta t_{max} = \Delta\boldsymbol{\varepsilon}_{max}/\dot{\boldsymbol{\varepsilon}}$) can be calculated. The maximum time is related to maximum barriers by $\Delta t_{max} = 10^{13} exp[-\Delta E_{max}/k_b T]$). In this way, we can estimate the upper limit to the energy barriers. In ABC sampling, we are only interested in rare events thus we ignore barriers smaller than thermal fluctuation energy (0.0258 eV for 300K). Thus, the meaningful barrier ranges are 0.0258-0.119 eV for high strain rate cases and 0.0258-0.91 eV for low strain rate cases. The identified barriers are closely monitored during simulations. If the barriers go out of the range, the simulation is terminated and the penalty size is adjusted to make sure the barriers identified are located in the range.

We are using nominal stress in all stress-strain curves. We extract stress from the ABC output and thus the MD simulation we are comparing is also at 0K. We were using $\boldsymbol{\varepsilon} = dL/L$ to define the strain. The reference lengths for small (112 atoms) and large (420 atoms) nano-slabs are 35.2Å and 70.4Å respectively.

4.2.5 Computational Cost Evaluation

In our work, the strain is applied to the system in discrete steps and the strain rate is a constant defined at the beginning of the simulation. Thus the computational cost depends on two factors: (i) the cost for ABC sampling during the iteration, NEB during the iteration, and KMC during the iteration and (ii) the number of strain increment (iteration) applied during loading. Please find the summary of computational cost in TABLE 4.1.

KMC is very fast in the present context (less than 1 second) and accordingly we have excluded it from the table. The time shown in TABLE 4.1 is an approximation since for different strain increments, the lapsed time for each ingredient is slightly different. Unfortunately, the time in our actual calculations is different than what is reflected in the

Table 4.1: Computational cost evaluation

	Small model with 116 atoms		Large model with 420 atoms	
ABC	2 minutes (1 processor)		8 minutes (2 processors)	
NEB	around 6 minutes (12 processors)		around 10 minutes (12 processors)	
Total time for single PES	around 9 minutes		around 20 minutes	
Number of strain increment	low strain rate	high strain rate	low strain rate	high strain rate
	559	1592	347	1860
Total time	4 day	10 day	5 day	25 day

table. The reason is that the PES varies (or evolves) with each strain increment. Thus, in order to sample efficiently, we need to manually adjust the penalty parameters every few strain increments. This requires additional time and labor.

4.2.6 Molecular dynamics (MD) Simulations with Different Potentials

Molecular dynamic simulations of high strain rate ($10^8 s^{-1}$) compression with MEAM (green curve) and EAM (pink curve) [113, 114] potentials are shown in Figure . We find that the MEAM based results matches our high-strain rate ABC calculation while the EAM based results match the QD evolution based on the PET approach [8]. Thus, we could claim that the discrepancy of our stress curve and the one in Ref. [8] is because we adopted different potentials. The reason we adopted MEAM potential is because we expected the possibility of surface reconstructions and MEAM was precisely developed (as an extension of EAM) to better handle surface properties of metals.

4.3 Results and Discussion

To benchmark the approach, we first consider a high strain rate of $1 \times 10^8 s^{-1}$ and compare the results with both conventional MD simulations and the Quenched Dynamics (QD) result from Ref. [8]. Pattamatta et al. [8] use a rather interesting approach for time-scaling based on bifurcation theory (—referred to as the Equilibrium Mapping (EM) approach). The deformation of the structure is shown in Figure 4.3 and our results (based on ABC, Figure 4.3 a) are compared with those of Ref. [8] QD process(Figure 4.3 b). Both methods start from the same initial structure (left snapshots), a fcc nano-slab. Under the compression, X-shaped shear band appears in the nano-slab (snapshots of $\varepsilon = 0.09$ in Figure 4.3

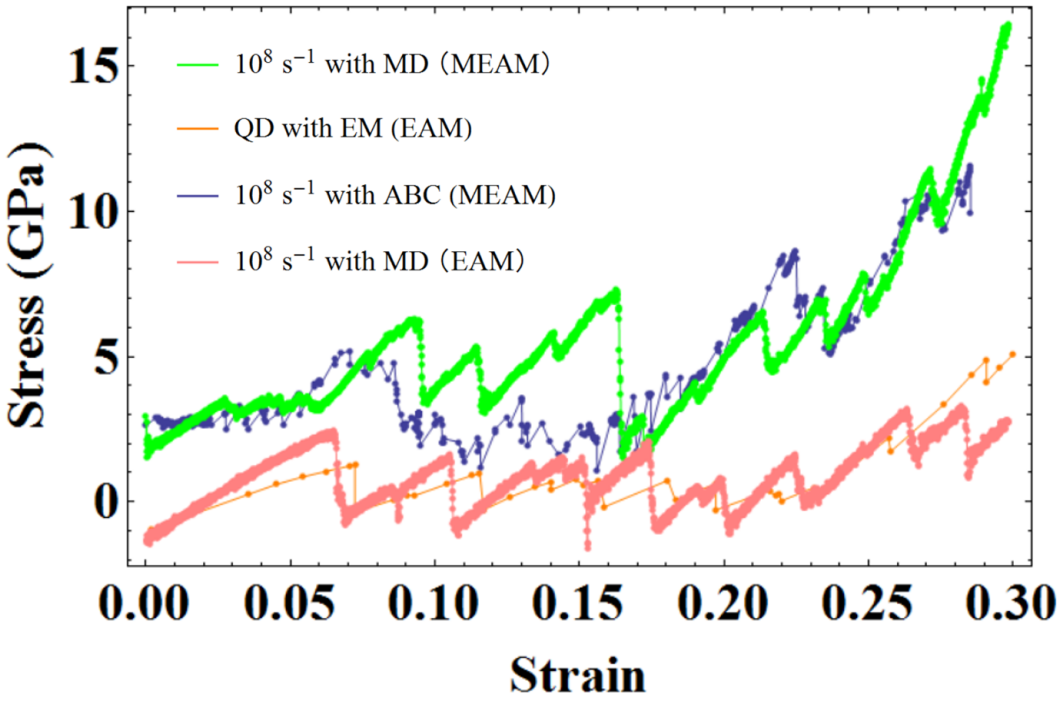

Figure 4.6: Comparison of stress-strain curves.

a and b. In the central region of the nano-slab, the crystallographic orientation rotates by 90° and maps the original {110} free surfaces (in x direction) on to {001}. The rotation of the crystallographic orientation pushes the X-shaped shear band to the top and bottom surfaces of the nano-slab (see the third snapshot in Figure 4.3 a and b) and finally a barrel-shaped nano-slab is formed (snapshots of $\varepsilon = 0.29$ in Figure 4.3 a and b). A comparison between Figure 4.3 a and b, shows that the deformation sequence and patterns predicted by our approach and that of Ref. [8] are qualitatively similar. We have also carried out conventional MD simulations of this same structure and those results also match ours. The resulting stress-strain behavior is shown in Figure 4.3 c. Our result (blue line) is consistent with conventional MD (green line). In summary, for the case of the high strain rate ($1 \times 10^8 s^{-1}$) accessible by conventional MD, our approach yields results that are consistent with both MD and those predicted by Pattamatta *et* al. [8].

We now turn to the key objective of this chapter—imposition of low-strain rates that are inaccessible by conventional MD. For this case-study, we impose a strain rate of $1s^{-1}$.

We remark that in Ref. [8], predicated on the EM method, this particular simulation case was stopped at $\varepsilon = 0.08$. The ensuing deformation(Figure 4.4) under slow compression is remarkably different from the high-strain rate case. The deformation is irregular and both amorphization and surface reconstruction, including extrusion at the sides, can be observed during compression. Starting from the same fcc nano-slab as the high strain rate case, amorphization starts from the top and bottom of the structure (snapshots of $\varepsilon = 0.03$ and $\varepsilon = 0.04$ in Figure 4.4a). At the strain value of 0.06, almost all the fcc character of the original slab structure disappears. With increasing compression, the structure eventually extrudes from the free surfaces of the nano-slab accompanied by extensive surface reconstruction (snapshots of $\varepsilon = 0.09$ and $\varepsilon = 0.15$ in Figure 4.4a). The proportion of crystalline structure progressively reduces with increasing deformation. Compared to the controlled (barrel-shaped) deformation evident in the high strain rate case, the deformation response at the low strain rate is almost "liquid-like". The difference of the responses of high/low strain rate is also quantified with the help of the corresponding stress-strain curves shown in Figure 4.4b.

To assess the effect of size on the deformation of the nano-slab, we also carried out a set of simulations on a larger nano-slab (shown in Figure 4.5). The size of the model has the same x/y ratio (25×70Å) as the smaller model shown in Figure 4.3 and in z direction, the thickness of the unit cell is 2.46Å. There are 399 free atoms and 21 atoms at the boundaries which are utilized to impose the requisite boundary conditions. As before, we imposed two different strain rates of $1 \times 10^8 s^{-1}$ and $1 s^{-1}$. The resulting deformation sequences are shown in Figure 5. In the case of high strain rate(top row in Figure 4.5), similar to the smaller-size model, the nano-slab undergoes a series of deformation from the initial fcc structure ($\varepsilon = 0$), exhibits two different kinds of shear bands ($\varepsilon = 0.06$ and $\varepsilon = 0.08$), and generally shows a similar trend as the smaller model, culminating in the barrel-shaped deformation($\varepsilon = 0.22$ and $\varepsilon = 0.25$). In sharp contrast, the behavior under low strain rate is considerably more irregular. From initial fcc structure, the system starts amorphization from surfaces to the central part of the nano-slab (snapshots of $\varepsilon = 0.01$ and $\varepsilon = 0.02$). Extrusion of the structure with surface reconstruction (snapshots of $\varepsilon = 0.03$ and $\varepsilon = 0.06$). As with the smaller

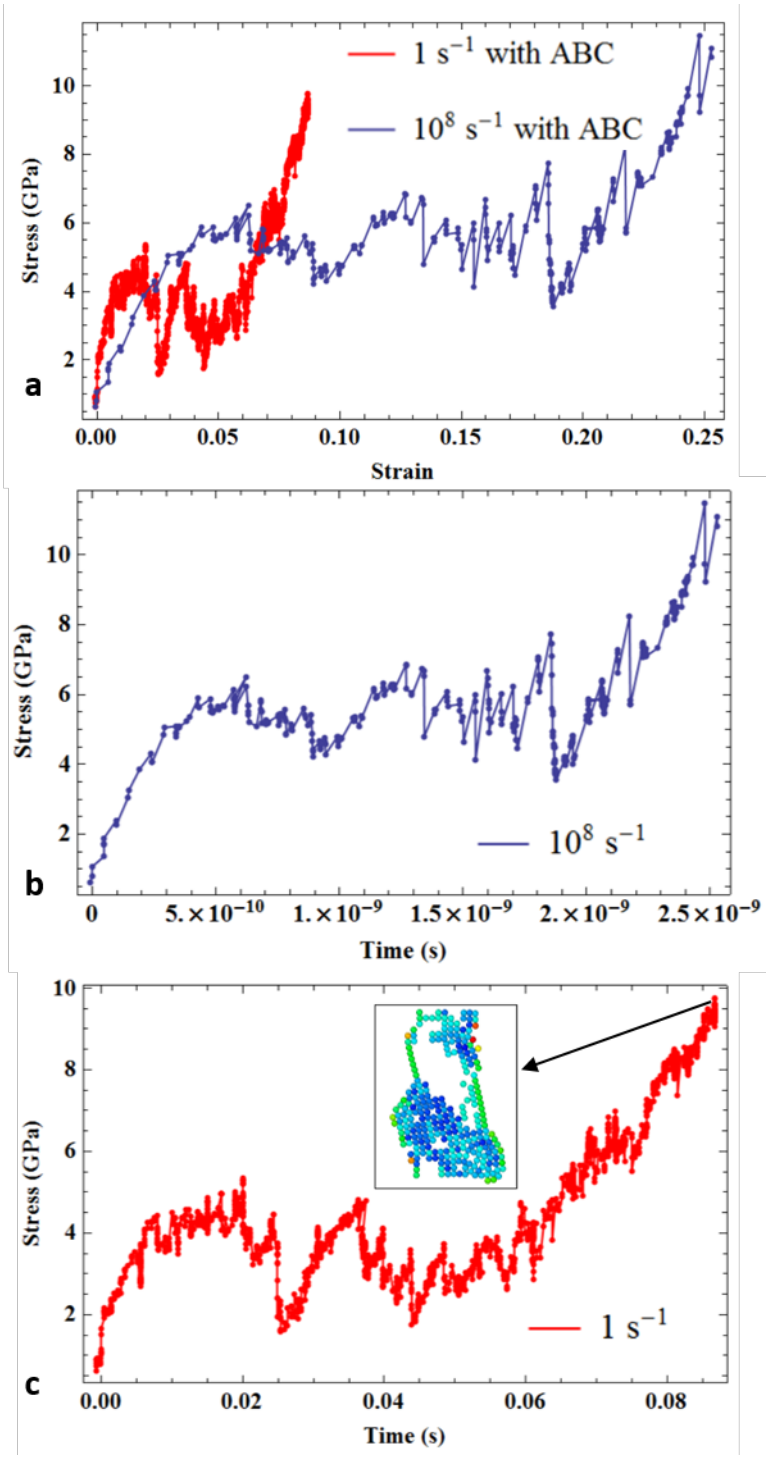

Figure 4.7: a)Stress-strain curves for high/low strain rate for the large model; b) Stress versus time for high strain rate; c) Stress versus time for low strain rate and the inset shows the structure using the centro-symmetry parameter for low strain rate and at the strain value of 0.09.

model, slow-strain rate behavior is "liquid-like". Referring to the inset of Figure 4.7c, the plot of the centro-symmetry parameter allows us to infer that the nano-slab center indeed remains crystalline.

In a recent study of sub-10-nm crystalline silver particles [72], both experiment and simulations observe "liquid-like"deformation in which the shape evolution is dominated by adatom diffusion on the surface and the structure which is a few layers under the surface remains crystalline. The reported deformation is quite similar to what we observed in our simulations. We believe that the studied nanostructure deforms in a "liquid-like"deformation (at slow strain rates) because of the surface diffusion while the central interior part of it behaves more like a crystalline solid, as shown in the inset of Figure 4.7c. Further, a comparison of stress-strain curves shown in Figure 4.7a indicates that for the case of low strain rate, hardening starts at the strain level of 0.07, however, for the case of high strain rate, the hardening may be observed at a much higher strain value of 0.2. In Figure 4.7b and c, we show stress versus time for both high strain rate and low strain rate cases. In our low strain rate simulations, a loading duration of 0.09 s is achieved—well in line with what may be observed in laboratory conditions. In contrast, for high strain rate, the total loading time is of the order of 10^{-9} s.

4.4 Summary

In summary, we have carried out a study of the mechanical compression behavior of nano-slabs to specifically interrogate its deformation behavior under both slow and fast strain rates. While high-strain rate deformation proceeds in an unremarkable manner—merely shortening its length along with the formation of an expected defect sub-structure, the slow-strain rate results (—precisely what is to be expected in most applications and laboratory experiments) exhibit a dramatically different behavior. We observe "liquid-like"deformation under low strain rate. *In Situ* experiments [72] appear to qualitatively confirm our observations that nano structures, indeed, are more likely to exhibit the deformation pattern we have captured with the adopted time-scaling approach in sharp contrast

to the predictions of conventional molecular dynamics.

5 Elucidating the Micro-mechanisms of Rate-Dependent Plasticity in a-LiSi Nano-structures

Rechargeable Li-ion batteries have attracted tremendous attention as potential candidates for future energy storage needs in a broad range of applications. Silicon is an attractive high-capacity anode material for Li-ion batteries. However, its capacity for the storage of Li atoms leads to exceptionally large volume expansion when the electrode is fully-lithiated. The huge inhomogeneous volume changes during the cycles of charging and discharging cause massive cracking of the Si electrode, and eventually result in the loss of electrical contact and consequent loss of capacity. As is well known, conventional molecular dynamics simulations can only address phenomena with characteristic times scales of (at most) a microsecond. Accordingly, in such simulations, the mechanical behavior is deduced under conditions of very high strain rates (usually $10^7 s^{-1}$ or even higher). This limitation severely impacts a realistic assessment of rate-dependent effects and not surprisingly, current molecular dynamics predictions grossly overestimate the yield strength of Li-Si (when compared with experiments). In this work, we attempt to circumvent the time-scale bottleneck of conventional molecular dynamics (MD) and provide novel insights into the mechanisms underpinning plastic deformation of Li-Si. We utilize an approach that involves the employment of a novel and recently developed potential energy surface (PES) sampling method—the so-called autonomous basin climbing (ABC)—to identify the local minima in PES. Combined with other techniques, such as nudged elastic band (NEB), kinetic Monte Carlo (KMC) and transition state theory (TST), we assess the nanostructure of amorphous Li-Si alloy under tensile strain rates ranging from $10^3 s^{-1}$ to $10^8 s^{-1}$. We find that in the case of Li-Si nano-structures, the basic mechanism of plasticity are similar to what has been discussed in other amorphous system—formation of shear transformation zone engineered by diffusion like process. We also identify the rotation of the STZ as a key dissipation mechanism. Furthermore, the behavior under high & low strain rate is quite different and accordingly convectional MD cannot be used to understand plasticity.

5.1 Introduction

Lithium-ion batteries find applications in portable electronics, electric vehicles and many other contexts where a reliable energy storage system is required [73, 74]. Intense efforts are dedicated to developing the next-generation Li-ion batteries with high energy density and long cycle life. Silicon is an important candidate for electrode material due to the potential of high specific charge capacity— more than ten times that of carbon based materials [115]. However, during the charging and discharging processes, the silicon electrode experiences a quite large volumetric change (as much as 300%) and the concomitant stresses lead to the nucleation of the defects, and eventually, mechanical failure of the system [116]. As a result, the effective charge capacity often sharply reduces after just a few charging and discharging cycles [117, 118, 119].

The use of amorphous silicon (a-Si), instead of its crystalline counterpart, is considered to offer several advantages. Experiments have shown that the amorphous alloys tend to cycle better than the corresponding crystalline phases [82, 84, 83]. There is increasing evidence showing that the mechanical degradation of Si electrodes under electrochemical cycling can be mitigated through the reducing the feature sizes, such as nanowires, nanoparticles, porous configurations, thin films, and core—shell structures [120, 73]. In experimental works, the plasticity behavior of fully lithiated nanowire has been observed [121] and it is reported that the strength of nano structure is more sensitive to strain rate [122]. A variety of continuum theories have been introduced to describe the plasticity deformation of lithiated silicon electrode [123, 124, 118]. However, the nanoscale mechanisms underlying the observed plastic behavior of Li-Si alloys remain unclear.

Atomistic simulations provide insights in understanding deformation process from atomistic point of view [125, 126]. Even though these modeling works have provided interesting insights, there is a fundamental limitation of conventional MD methodology that precludes an assessment of material behavior over realistic laboratory-timescales. MD can only handle time-scales of the order of, at best, a few microseconds. Even though this is adequate

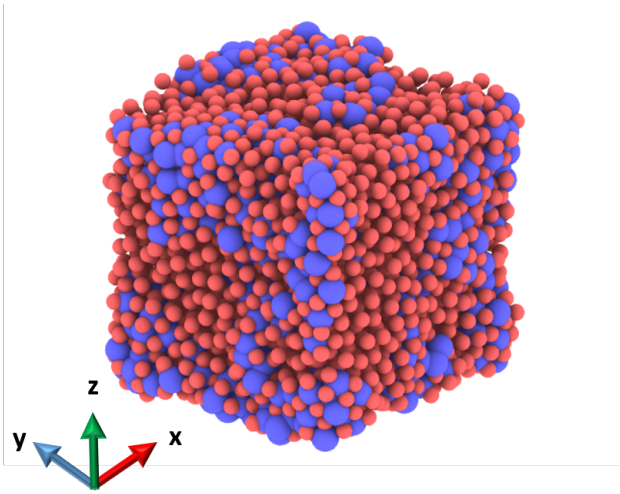

Figure 5.1: Initial amorphous $Li_{15}Si_4$ alloy nano-structure. Red small balls represent Li atoms and blue large balls represent Si atoms.

for understanding several physical, chemical, and mechanical phenomena in materials, the inability to address long timescales prevents an assessment of slow-strain rate mechanical behavior that is the norm in laboratory experiments and real-life applications. It has been valid that rate effect are important for plastic deformation [127].

In this chapter we employ a collection of algorithms that assess the mechanical behavior of amorphous fully lithiated nanostructure under strain rates ranging from $10^3 s^{-1}$ to $10^8 s^{-1}$.

5.2 Approach and Simulation Details

We choose the fully lithiated amorphous silicon ($Li_{15}Si_4$) as the example for this simulation since the fully lithiated silicon is the most severe case as far as mechanical deformation concerned . In this work, we create the amorphous structure via a rapid quench process. We first increase the temperature of an initial crystalline structure to 4000K. Then the temperature is decreased rapidly to room temperature. Such rapid quenching process creates the amorphous structure shown in Figure 5.1. There are 4864 atoms in the initial structure. As shown in Figure 5.1, small Lithium atoms are colored in red and large Silicon atoms are colored in blue. Constant strain rate is applied from z direction and lateral surfaces on x and y directions are free surfaces. The modified embedded-atom method (MEAM)

potential is used in all of the calculations presented in this work [14].

Two independent tensile testings with different imposed strain rates are carried out. The high strain rate of $10^8\ s^{-1}$ which is accessible with regular MD and the low strain rate of $10^3\ s^{-1}$. The atomistic simulation approach we are using in this study is a collection of a few simulation techniques, including a recently developed potential energy surface sampling method, the so-called autonomous basin climbing approach (ABC) [41]. Here, we give a brief description of the simulation techniques. More details can be found in our recent paper [7]. Starting with a minimum-energy configuration (initial structure shown in Figure 5.1), ABC method adds Gaussian penalty functions to the potential energy of the entire space, and pushes the system away from the initial energy minimum, until it enters into an adjacent potential energy well. Keep adding penalties until a few neighbouring states are identified in this process. Then, nudged elastic band method (NEB) is applied to refine the energy barriers from initial state to all the identified energy minimum on this PES in previous ABC treatment. Kinetic Monte Carlo (KMC) is then applied to select the most probable state for the system on current PES. Transition state theory (TST) is adopted to calculate the transition time from initial energy well to the selected energy well. The transition time multiplied constant strain rate defined before simulation will give the strain need to be applied to the system in next simulation step. In this way, a constant tensile rate is applied to the system. With the help of the sampling method, we accelerate the simulation by avoiding the accumulate of very small time steps in regular MD. To benchmark our simulation, MD simulation for high strain rate is carried out and compared with the results from ABC approach.

To clearly compare the plastic deformation during the two strain rates, we start unloading treatment when the strain reaches to 0.079 at which stage yielding has occurred for both strain rates.

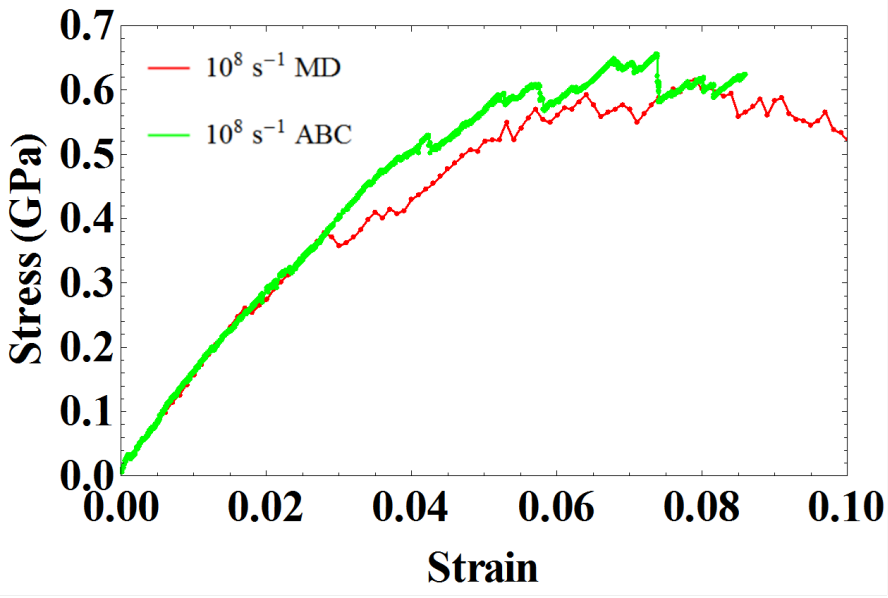

Figure 5.2: Stress-strain curves of tensile testing using MD (red curve) and ABC (blue curve) with imposed strain rate of $10^8 s^{-1}$.

5.3 Results and Discussion

We first compare our ABC simulation of high strain rate (10^8 s^{-1}) with MD simulation. For this particular case, we don't expect our ABC-based results to differ from MD and accordingly, this is a useful benchmark analysis. As shown in Figure 5.2, the agreement between MD simulation and ABC approach is quite remarkable with nearly identical and similar yield stress. Based on this comparison, we conclude that the present method can reasonably capture high strain rate deformation behavior of amorphous $Li_{15}Si_4$ nanostructure.

We now turn to the key objective of this work-imposition of low-strain rates that are inaccessible by conventional MD. Characteristic stress-strain curves are show in Figure 5.3. The two different stress-strain curves correspond to two distinct tensile rates, 10^8 s^{-1} and 10^3 s^{-1}. It is seen that the stress-strain curves exhibit typical characteristics—an initial linear portion, then strain hardening. Clearly, the strength is rate dependent. In comparing with two curves, faster strain rate result in higher stresses with the increase in strength. Slow loading process allows longer time for structural relaxation and self-adjustment. The

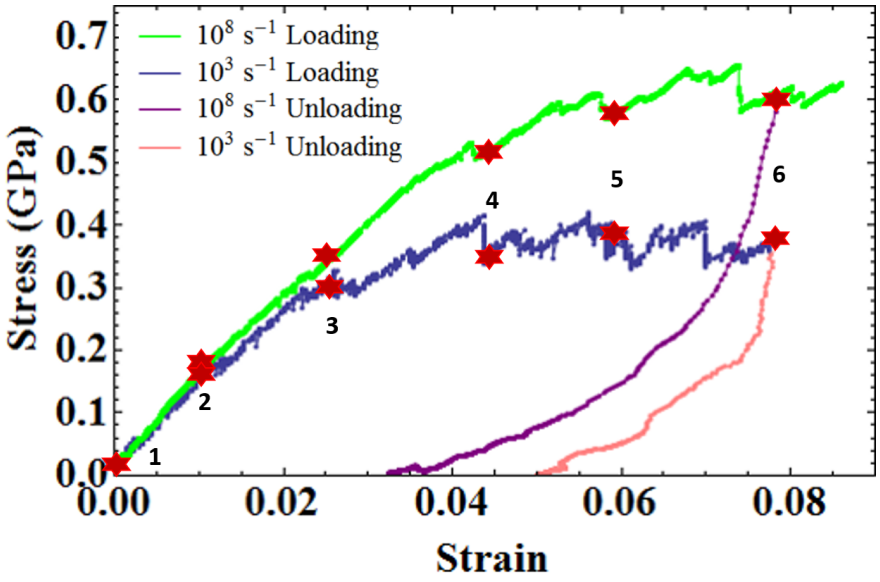

Figure 5.3: Stress-strain curves of loading and unloading under different imposed strain rates. Red stars represent stage of 1)$\varepsilon = 0$, 2)$\varepsilon = 0.01$, 3)$\varepsilon = 0.025$, 4)$\varepsilon = 0.044$, 5)$\varepsilon = 0.058$ and 6)$\varepsilon = 0.079$ where snapshots are taken for further analysis.

stress sustained by atoms can be relieved from these micro adjustments. As a result, the yielding occurs at lower stresses at slower strain rate. The difference of strength between high and low strain rates is nearly 75%.

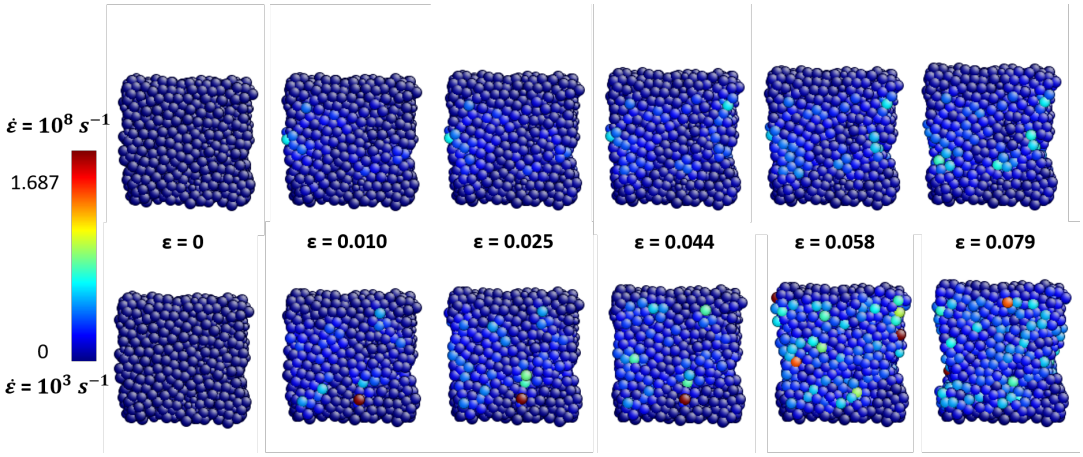

Figure 5.4: Local shear strain (η_i^s) visualization of high strain rate stretching (top line) and low strain rate stretching (bottom line) corresponding to different strain values.

To investigate how much plastic deformation accumulated in the structures during loading, we unload from the strain value of $\varepsilon = 0.079$. We find that the residual strain is 0.032

for the high strain rate case and 0.05 for the low strain rate case.

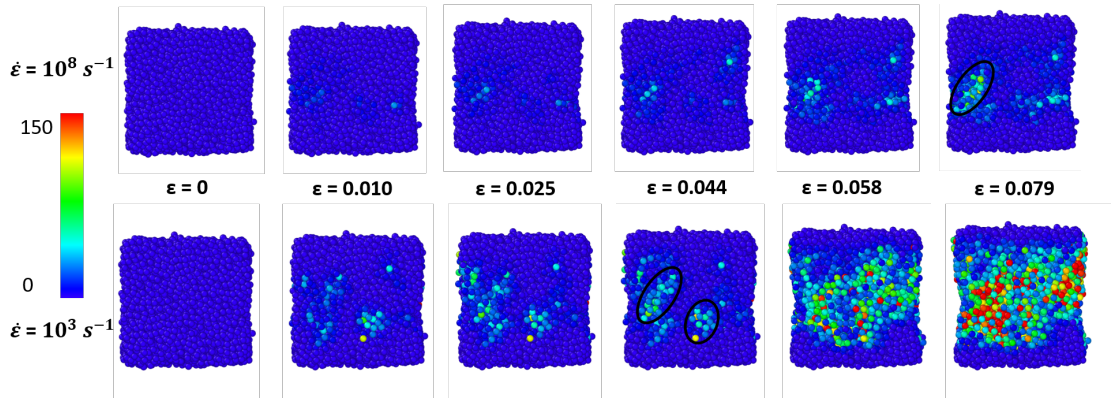

Figure 5.5: Non-affine displacement visualization of {010} free surface with high strain rate stretching (top line) and low strain rate stretching (bottom line) at different strain values. Black circles highlight a few examples of STZs.

An advantage of atomistic simulations is it can provide detailed visualization from an atomistic viewpoint and thus insights into the mechanism of the plastic deformation. To quantify the plastic deformation at the atomic level, we first evaluate the local shear strain η_i^s for every atom [128, 129]. Evaluation of η_i^s requires two configurations, the reference one and the current one. To facilitate a subsequent comparison between the two loading rates, we take the initial configuration as the reference (label 1 in Figure 5.3) and all the labeled points as "current"configurations corresponding to different strain values. The local Lagrangian strain matrix η_i can be calculated from

$$\boldsymbol{\eta}_i = \frac{1}{2}\left(\boldsymbol{J}_i^T \boldsymbol{J}_i - \boldsymbol{I}\right), \tag{5.1}$$

where $\boldsymbol{I}$ is identity matrix and $\boldsymbol{J}_i$ is affine transformation matrix which applies affine transformation on the initial configuration to convert it to the corresponding current configuration. The dilatational component is

$$\eta_m = \frac{1}{3} Tr\left(\boldsymbol{\eta}_i\right), \tag{5.2}$$

and the local shear strain η_i^s is defined as the shear component of local Lagrangian strain

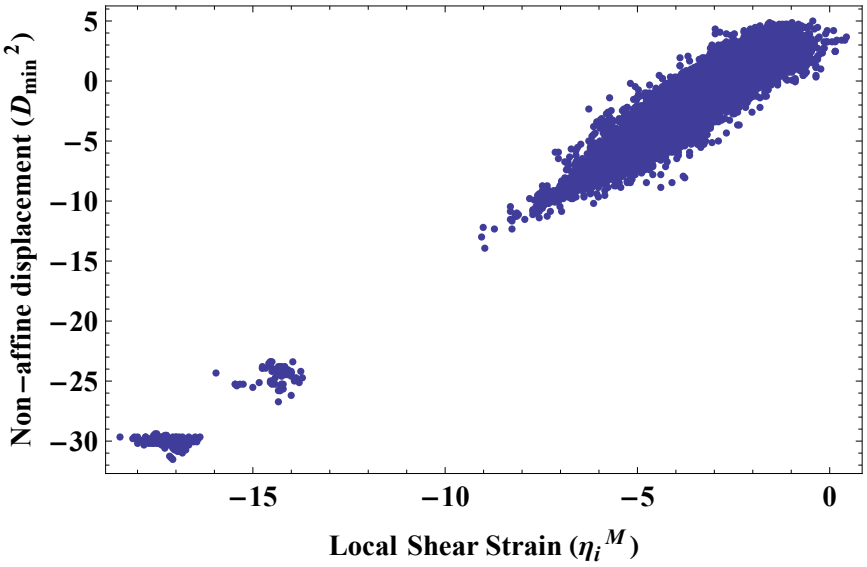

Figure 5.6: Variation of η_i^s with respect to D_{min}^2 for slow strain rate. High strain rate case has similar trend and the figure is not shown here.

tensor:

$$\eta_i^s = \sqrt{\frac{1}{2} Tr\left(\boldsymbol{\eta}_i - \eta^m \boldsymbol{I}\right)^2}. \tag{5.3}$$

As shown in Figure 5.4, with the increase of the applied strain, both the high strain rate and low strain rate case exhibit increasing local shear strain. Comparison between top line (high strain rate) and bottom line (low strain rate) in Figure 5.4 reveals that atoms with higher shear strain in high strain rate loading are localized in the center of the sample, while the atoms that have high shear strain in low strain rate case are spread in the sample ($\varepsilon = 0.058$ and $\varepsilon = 0.079$). This indicates that more atoms are involved in the deformation for low strain rate case.

To systematically analyze the plastic deformation and the exact region where the irreversible plastic rearrangements are occurring–the so-called shear transformation zones (STZs) need to be identified. In this work, besides analyzing local shear strain which represents the local shear component of the shape change, non-affine displacement (D_{min}^2) is calculated to locate the STZs [130, 129]. Similar to local shear strain, the calculation of non-affine displacement also require two configurations. We take the initial structure as the reference configuration and all the labeled points in Figure 5.3 as current configurations.

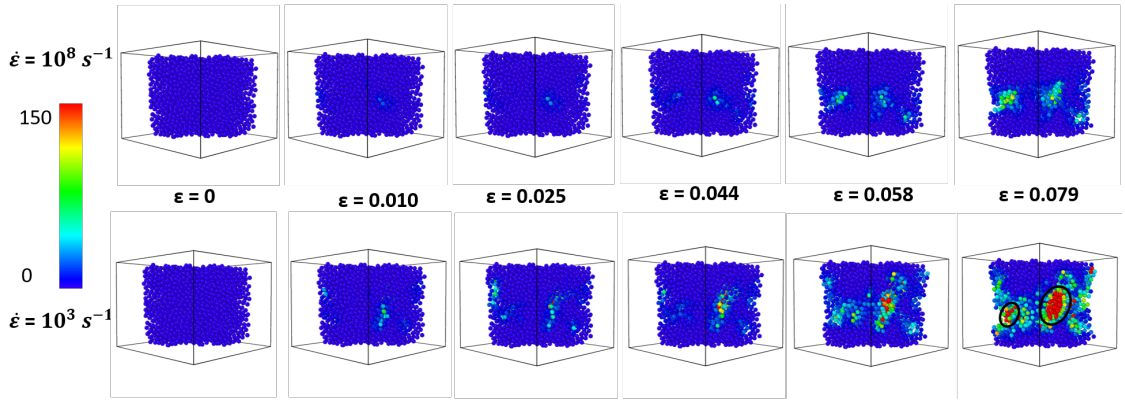

Figure 5.7: Non-affine displacement visualization of $\{1\bar{1}0\}$ surface with high strain rate stretching (top line) and low strain rate stretching (bottom line) at different strain values. Black circles highlight two examples of STZs.

First, we apply an affine transformation to the distance vector between neighboring particle (j) within the cutoff distance r_c (assume there are N_i atoms within r_c and $j \in N_i$) and the center particle (i) at reference time:

$$\boldsymbol{r}_{ji}^{a}(0) = \boldsymbol{J}_i \boldsymbol{r}_{ji}(0), \tag{5.4}$$

where the distance vector $\boldsymbol{r}_{ji}(0)$ is defined as:

$$\boldsymbol{r}_{ji}(0) = r_j(0) - r_i(0). \tag{5.5}$$

Analogues to the way mean square displacement (MSD) is defined, D^2 can be expressed as:

$$D^2 = \frac{1}{N_i} \sum_{j \in N_i} \left[\boldsymbol{r}_{ji}(t) - \boldsymbol{r}_{ji}^{a}(0) \right]^2. \tag{5.6}$$

The difference between MSD and D^2 is that MSD ($MSD = \frac{1}{N} \sum_{n=1}^{N} [\boldsymbol{x}(t) - \boldsymbol{x}(0)]^2$) is an evaluation based on atom position vectors $\boldsymbol{x}$, while D^2 is an definition based on displacement vectors between neighboring atoms (j) and center atom (i). From Equation 5.6 and 5.4, D^2 depends on both distance vectors as well as affine matrix $\boldsymbol{J}_i$. To minimize the error of deformation mapping, best affine transformation matrix need to be used and the non-affine

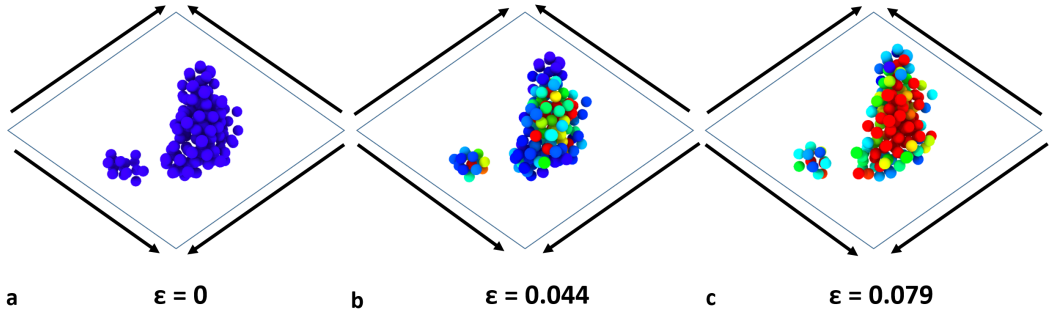

Figure 5.8: Closedup picture of the variation of the two STZs shown in the snapshot of low strain rate case with $\varepsilon = 0.079$ in Figure 5.7. Atoms are colored according to their values of D_min^2 using the same scale as in Figure 5.7 at a) $\varepsilon = 0$, b) $\varepsilon = 0.044$ and c) $\varepsilon = 0.079$. Atoms outside STZs in snapshot of low strain rate case with $\varepsilon = 0.079$ in Figure 5.7 are hided.

displacement D^2_{min} is defined as:

$$D^2_{min} = \frac{1}{N_i} \min_{\boldsymbol{J}_i} \sum_{j \in N_i} \left[\boldsymbol{r}_{ji}(t) - \boldsymbol{r}^a_{ji}(0) \right]^2 . \tag{5.7}$$

The results of computed non-affine displacement for labeled points in Figure 5.3 on {010} free surface are shown in Figure 5.5. The top row are the snapshots for the high strain rate case and the bottom row are the snapshots for the low strain rate case. The nucleation of of STZs (black circles in Figure 5.5) are captured for both cases. The low strain rate loading process nucleate STZs at an earlier stage comparing with high strain rate loading case. The STZs can be observed at the strain of 0.025 or even earlier in the low strain rate case and they appear until $\varepsilon = 0.058$ in high strain rate situation. Besides, the size of STZs in low strain rate case is larger than high strain rate case with high values of D^2_{min} (atoms in red color). Comparison between snapshots shown in Figure 5.4 and Figure 5.5 reveals that the larger values of η^s_i appear in the same region as larger values of D^2_{min}. The correlated relation of η^s_i and D^2_{min} is because the plastic deformation from shape change (η^s_i) will introduce local particle arrangement in the neighborhood (D^2_{min}), especially in the slow loading case which allows neighbor atoms to rearrange themselves. These self-rearrangement can involve the participation of more neighboring atoms and generate larger STZs with higher D^2_{min} values.

To qualitatively evaluate the correlated relation of D^2_{min} and η^s_i, we plot all the calculated D^2_{min} respect to η^s_i using logarithmic axes for both parameters in Figure 5.6. Even though the dots are scatted, statistically, a linear relationship between D^2_{min} and η^s_i is evident. This reminds us again of the similarity between D^2_{min} and MSD. Based on the linear correlation of MSD and time t, the diffusivity of thermally diffusive particle can be evaluated. The atomistic local shear strain η^s_i may play the role of time t and drive the effective particle diffusion leading to deformation [129]. The linear fitting of high strain rate case and low strain rate case are very close, thus these correlation is not rate dependent.

In the case of uni-axial tension of a rectangular block, the maximum shear stress occurs on the planes whose normal and the tensile direction is 45 degree. Thus in order to better visualize the deformation and rotation of STZs, we focus on $\{1\bar{1}0\}$ section which is parallel to loading direction (Figure 5.7). On this surface, the effect of maximum shear stress on STZs should be most conspicuous. In Figure 5.7, clear differences between high strain rate case (top line) and low strain rate case (bottom line) are observed from this section. At every strain values, except $\varepsilon = 0$, STZs in low strain rate case are larger in size and with higher value of D^2_{min} compared with the STZs in high strain rate snapshots. Besides, we see that the STZs appearing in these cases are located in similar regions. The snapshots at $\varepsilon = 0.079$ are good examples of this observation. For low strain rate case, two STZs (circled in black) are formed with very high D^2_{min} (atoms with red color). In the same region for sample loading with low strain rate, two smaller STZs with lower D^2_{min} appears. While the tensile deformation leads to atomic re-arrangements in both strain rate cases. In the faster case, there is not enough "time"for the atoms to dissipate energy. Slow loading process, however, allows the neighboring atoms to adjust themselves corresponding to the shape change so that the stresses on the atoms are relieved much more efficiently.

In Figure 5.7, we show a zoomed view of the variation of STZs shown in the snapshot of low strain rate case with $\varepsilon = 0.079$. Atoms outside the STZs are hidden in this figure. We track the atoms within STZs (Figure 5.8 c) back at the stages of $\varepsilon = 0$ (Figure 5.8 a) and $\varepsilon = 0.044$ (Figure 5.8 b). The arrows indicate the dominant stress sustained by the STZs.

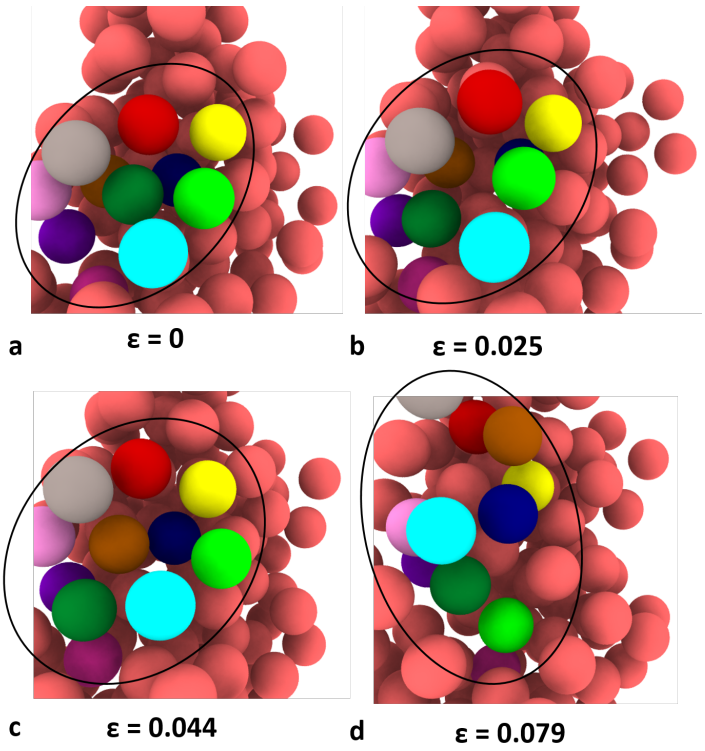

Figure 5.9: Tracing map of the positions of a few atoms (in different colors) inside the big STZ in the snapshot of low strain rate case at $\varepsilon = 0.079$ in Figure 5.7. The snapshots are taken at a) $\varepsilon = 0$, b) $\varepsilon = 0.025$, c) $\varepsilon = 0.044$ and d) $\varepsilon = 0.079$.

With the increase of the strain, the larger STZ extends with the effect of shear stress. The smaller STZ initially is in the shape of a flat ellipsoid. Under the effect of shear stress, it becomes a circle.

With the help of ABC-based approach adopted in this work, we are able to tracking the atom movement during the slow stretching process in which plastic deformation occurs. As shown in Figure 5.9, we track a few atoms inside of the big STZ shown in Figure 5.7 (snapshot of slow strain rate case at $\varepsilon = 0.079$). Figure 5.9 a and b illustrate deformation which mainly occurred in elastic region (points 1 and 3 in Figure 5.3). The atoms do move under strain, while there is no significant variation of the relative positions (colored atoms in ellipsoid). With the same amount of deformation ($\Delta\varepsilon = 0.025$) as Figure 5.9 a and b, in the plastic deformation region (point 4 and 6 in Figure 5.3), the STZ in Figure 5.9 c rotates clockwise and become the shape shown in Figure 5.9 d. This type of rotation is in

our opinion an important dissipation mechanism. During elastic deformation, because of the stretching, atoms are under increasing stress. Correspondingly, in Figure 5.3, the stress difference between point 1 and 3 are 0.3 GPa. For plastic deformation, due to this type of rotation, with same amount of strain increment, the stress of point 4 and 6 in Figure 5.3 are almost same.

5.4 Summary

In summary, we carried out a study of comparing mechanical behavior of amorphous $Li_{15}Si_4$ nano-structure in tensile testing with different strain rates. With the help of ABC-based approach, we were able to lower the strain rate to $10^3\ s^{-1}$ and provided atomistic insights beyond the capability of MD. Low strain rate stretching generates a series of plastic deformation end up with a significant reduction of yield stress. The low strain rate stretching form larger STZs at a earlier stage compared with high strain rate case.

6 Chapter 6: Concluding Remarks

In this dissertation, we have employed a newly adapted atomostic modeling technique to investigate the slow time scale behavior of different systems. The previous chapters, which highlighted a range of application areas, showed examples of how ABC can be a powerful tool to study the behavior of atomistic systems over long time scales and at slow strain rates, both of which are not accessible to classical MD simulations. However, similar to any other numerical technique, there are still important unresolved issues with the ABC methods. In this section, we therefore discuss these issues where offering, where relevant, possible solutions or paths forward.

6.1 Computational Efficiency

The first, and perhaps most important issue with the ABC methods is that of computational expense and efficiency. Ideally, these methods could be used interchangeably with classical MD, and thus used for atomistic systems containing hundreds of thousands, if not millions of atoms. However, we are currently far from this objective. The key factor causing the computational expense of the ABC method can be shown through Equation (2.2), where to calculate the penalty function-modified potential energy $\Psi(\mathbf{r})$, a summation over all applied penalty functions p is required. This is problematic because for the ABC method to explore the PES most efficiently, all previously applied penalty functions must be kept such that energy wells that have already been explored are not explored multiple times. While this makes the PES search more efficient, it also means that the computational expense associated with ABC increases as more of the PES is explored. Thus, the speed of the PES exploration is fairly good at the beginning of a typical ABC simulation, but decreases noticeably as more of the PES is explored.

Various issues have been developed to resolve this issue, which has limited the system sizes that can be studied using the ABC methodologies described in this work to a few tens of thousands of atoms. One obvious approach is to parallelize the ABC methodology, for example using an open source simulation code like LAMMPS [70], which has been done by both the Sharma and Park groups. However, because the ABC method also includes energy

minimization after each penalty function is applied, the benefits of parallelization quickly decrease beyond a few nodes.

Another approach to alleviate this issue is to reduce the information stored in memory, which can be realized in multiple ways. (1) By combining penalty functions, the ABC-SLME approach can significantly reduce the number of stored penalty functions and allow the system to explore more of the PES before the computational overhead becomes intractable [46]. (2) The PES exploration can be done in only localized regions of interest. For example, if the volume of the system where the phenomena of interest is localized or can be identified *a priori*, then only those portions of the PES associated with the atoms in the localized volume could be penalized. (3) Another approach would be to limit the number of penalty functions that are stored in memory; there would be some risk to this approach that the system could still return to a previously explored energy well if the penalty functions were removed, but this could also be done by basing the decision to remove previously stored penalty functions on a criteria based on the distance away from previously explored energy wells on the PES.

6.2 PES Resolution and Penalty Function Parameter Selection

Another issue of ABC is the resolution of the PES that is achieved, which as shown in Figure 6.1 depends on the heights and widths (or sizes) of the penalty functions. As shown in Figure 6.1, if larger penalty functions ϕ_{p1} (red balls) are used, the PES that is effectively described is Φ_1. In contrast, if smaller penalty functions ϕ_{p2} (blue balls) are applied to the PES, the effective PES that is described is Φ_2.

If Φ_2 is the effective PES, then small-scale atomic motion like the diffusion of atoms can be captured. However, if the larger penalty functions leading to the effective PES described by Φ_1 are chosen, then only larger, more collective atomic motions such as planar defects may be captured, where we note that Figure 6.1 is meant to be conceptually illustrative rather than quantitatively accurate. Therefore, the choice of the penalty function parameters can impact the physical phenomena that are observed in the simulations. This choice also impacts the computational efficiency. If the penalty functions are too large, the resolution may not be fine enough to capture the deformation, while if the penalty functions are

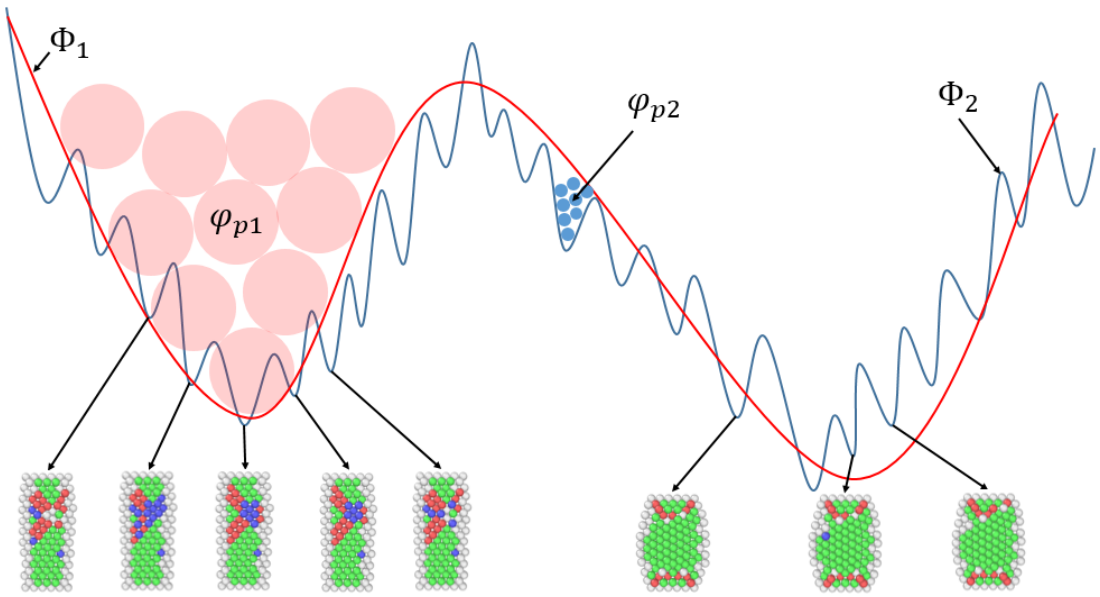

Figure 6.1: PES exploration with different penalty function resolutions. Note that the figure is meant to be conceptually illustrative rather than quantitatively accurate.

too small, it will take a long time to explore a meaningful portion of the PES.

Unfortunately, there is currently no rigorous approach to quickly choosing the appropriate penalty function size and shape, and thus physical intuition and experience with both the ABC method as well as the physics of the problem of interest are required. This is particularly important for strain and strain-rate dependent phenomena, where the underlying PES evolves and changes with each strain increment, and thus where the penalty function parameters would need to dynamically evolve for each strain increment. Therefore, an approach that could identify the appropriate penalty function parameters based solely on the interatomic potential would be greatly beneficial.

This requirement is somewhat satisfied by the ABC-SLME method [46] as the penalty functions that result from the combination of multiple penalty functions are constrained in certain ways. Specifically, the ABC-SLME initializes new penalty function parameters after a true local energy minimum is explored. The penalty function width and height are determined by measuring the displacement and energy difference between a new local minimum and the corresponding saddle point. In this way, the penalty function parameters are self-determined and automatically updated according to the underlying PES.

6.3 Entropic Effects

As has been established, the goal of the ABC method is to sample the PES. In doing so, this means that entropic effects, which contribute to the free energy of the system, are not accounted for, and thus the ABC method works best for problems in which the entropic effects do not dominate. This may be valid for lower temperature cases, or for applications where the PES barriers are sufficiently high such that entropy can be neglected, as the PES is temperature-independent. We note that while we have determined the ability of the ABC methods to access slow strain rate phenomena in amorphous solids [59, 60, 3], we have not, to-date, evaluated the performance of the ABC methodologies for soft amorphous materials like polymers.

In reality, the system moves from one basin to another with a rate that is dependent on the energy barrier between the two basins, as well as temperature, and thus entropic effects can be included via TST. For example, Fan *et al.* [93] investigated the temperature dependence of average vacancy cluster size of a bcc Fe system using TST and KMC based on configurations identified in ABC. The prediction of the cluster sizes using ABC and KMC was found to match experimental measurements. In this way, entropic effects can somewhat be accounted for through the KMC approach to choosing the trajectory along the PES. For other, biologically-relevant problems like protein unfolding, the difference between the free energy surface and the PES cannot be neglected. In these cases, umbrella sampling has been used to convert the information from the PES to that of a free energy [6, 54]. Such approaches can extend the validity of the ABC methodology, though a generic free energy-based search methodology would certainly be a long-term preferable alternative.

6.4 One Dimensional PES Exploration

In the original ABC and ABC-SLME sampling, due to the manner in which the penalties are applied, the system does not return back to energy well it has visited. In this way, the original ABC and ABC-SLME approaches [93, 131] ignore the appearance of other possible jumps from the current state. However, because this results in an incomplete catalog of possible transition states, it results in an overestimation of the transition times.

The time overestimation problem could be fixed through extending the searching dimensions, for example, ABC-E [24] (or other related methods like the dimer approach [21]). In this algorithm, after a new minimum is identified using ABC, a penalty is added on the saddle point to block the identified path. The system then is sent back to the initial state to find other possible minima around the initial state. The way ABC-E is adopted to search multiple transition paths is quite similar to ART [19] and the dimer approach [21].

There are advantages and disadvantages for both searching methods. A benefit of the one-dimensional search is that more states on the PES is explored, which may enable the observation of a dominant transition pathway or physical mechanism, while neglecting other, potentially less important transition paths. These one-dimensional searching methods are also more efficient. However, ignoring the existence of other possible (i.e. higher energy) exit pathways has been shown to lead to overestimations of the calculated transition time out of an energy well [24, 131, 132].

ABC-E and other similar searching algorithm, such as dimer or ART can identify multiple possible transition pathways out of a given energy well, which in our experience is particularly important for diffusion-based problems, where there are many competing states and pathways. However, the additional computational expense entailed in cataloging multiple transition pathways can be prohibitive. For example, in recent studies of the annihilation of dislocation dipoles, the ART method was unable to complete the simulations, while ABC was able to observe the dislocation dissociation processes [133, 134]. These issues again illustrate the need for more efficient ways to perform ABC-based explorations of the PES.

6.5 Length Scale Limitations

As we have discussed in this review, the various ABC methods have been effective in addressing the timescale issues that traditionally arise in classical MD simulations. However, in doing so, because of the limitations in the number of atoms (i.e tens of thousands) that can be considered, the ABC methods are, at present, length scale limited. This length scale limitation also limits the types of problems that can be tackled using ABC, and thus the physical phenomena that are most often studied are those with localized, unit processes like diffusion and localized plastic deformation.

One approach that may be beneficial to extending the length scales of the ABC simulations is to use coarse-grained atomistic potentials, i.e. [135]. Using such potentials would enable the study of significantly larger length scales and system sizes with the same number of degrees of freedom, while potentially opening up the study of more complex system mechanics.

References

[1] X. Yan, A. Gouissem, and P. Sharma, "Atomistic insights into li-ion diffusion in amorphous silicon," *Mechanics of Materials*, vol. 91, pp. 306–312, 2015.

[2] P. Cao, H. S. Park, and X. Lin, "Strain-rate and temperature-driven transition in the shear transformation zone for two-dimensional amorphous solids," *Physical Review E*, vol. 88, no. 4, p. 042404, 2013.

[3] P. Cao, X. Lin, and H. S. Park, "Strain-rate and temperature dependence of yield stress of amorphous solids via a self-learning metabasin escape algorithm," *Journal of the Mechanics and Physics of Solids*, vol. 68, pp. 239–250, 2014.

[4] Y. Fan, Y. N. Osetskiy, S. Yip, and B. Yildiz, "Mapping strain rate dependence of dislocation-defect interactions by atomistic simulations," *Proceedings of the National Academy of Sciences*, vol. 110, no. 44, pp. 17756–17761, 2013.

[5] A. Gouissem, R. Sarangi, Q. Deng, and P. Sharma, "Bridging time-scales: Grain boundary sliding constitutive law from atomistics," *Computational Materials Science*, vol. 104, pp. 200–204, 2015.

[6] P. Cao, G. Yoon, W. Tao, K. Eom, and H. S. Park, "The role of binding site on the mechanical unfolding mechanism of ubiquitin," *Scientific Reports*, vol. 5, p. 8757, 2015.

[7] X. Yan and P. Sharma, "Time-scaling in atomistics and the rate-dependent mechanical behavior of nanostructures," *Nano Letters*, vol. 16, no. 6, pp. 3487–3492, 2016.

[8] S. Pattamatta, R. S. Elliott, and E. B. Tadmor, "Mapping the stochastic response of nanostructures," *Proceedings of the National Academy of Sciences*, vol. 111, no. 17, pp. E1678–E1686, 2014.

[9] G. I. Taylor, "The mechanism of plastic deformation of crystals. part I. theoretical," *Proceedings of the Royal Society of London (A)*, vol. 145, no. 855, pp. 362–387, 1934.

[10] V. Bulatov and W. Cai, *Computer simulations of dislocations*, vol. 3. Oxford University Press on Demand, 2006.

[11] E. B. Tadmor and R. E. Miller, *Modeling materials: continuum, atomistic and multiscale techniques*. Cambridge University Press, 2011.

[12] V. Yamakov, D. Wolf, S. Phillpot, and H. Gleiter, "Grain-boundary diffusion creep in nanocrystalline palladium by molecular-dynamics simulation," *Acta Materialia*, vol. 50, no. 1, pp. 61–73, 2002.

[13] H. Van Swygenhoven, M. Spaczer, A. Caro, and D. Farkas, "Competing plastic deformation mechanisms in nanophase metals," *Physical Review B*, vol. 60, no. 1, p. 22, 1999.

[14] Z. Cui, F. Gao, Z. Cui, and J. Qu, "A second nearest-neighbor embedded atom method interatomic potential for li–si alloys," *Journal of Power Sources*, vol. 207, pp. 150–159, 2012.

[15] A. Kushima, X. Lin, J. Li, J. Eapen, J. C. Mauro, X. Qian, P. Diep, and S. Yip, "Computing the viscosity of supercooled liquids," *The Journal of chemical physics*, vol. 130, p. 224504, 2009.

[16] A. Kushima, J. Eapen, J. Li, S. Yip, and T. Zhu, "Time scale bridging in atomistic simulation of slow dynamics: viscous relaxation and defect activation," *The European Physical Journal B*, vol. 82, no. 3-4, pp. 271–293, 2011.

[17] A. Laio and M. Parrinello, "Escaping free-energy minima," *Proceedings of the National Academy of Sciences*, vol. 99, no. 20, pp. 12562–12566, 2002.

[18] A. Laio and F. L. Gervasio, "Metadynamics: a method to simulate rare events and reconstruct the free energy in biophysics, chemistry and material science," *Reports on Progress in Physics*, vol. 71, no. 12, p. 126601, 2008.

[19] G. Barkema and N. Mousseau, "Event-based relaxation of continuous disordered systems," *Physical review letters*, vol. 77, no. 21, p. 4358, 1996.

[20] N. Mousseau and G. Barkema, "Traveling through potential energy landscapes of disordered materials: The activation-relaxation technique," *Physical Review E*, vol. 57, no. 2, p. 2419, 1998.

[21] G. Henkelman and H. Jónsson, "A dimer method for finding saddle points on high dimensional potential surfaces using only first derivatives," *The Journal of chemical physics*, vol. 111, no. 15, pp. 7010–7022, 1999.

[22] E. Cances, F. Legoll, M.-C. Marinica, K. Minoukadeh, and F. Willaime, "Some improvements of the activation-relaxation technique method for finding transition pathways on potential energy surfaces," *The Journal of chemical physics*, vol. 130, no. 11, p. 114711, 2009.

[23] D. Rodney, A. Tanguy, and D. Vandembroucq, "Modeling the mechanics of amorphous solids at different length scale and time scale," *Modelling and Simulation in Materials Science and Engineering*, vol. 19, p. 083001, 2011.

[24] Y. Fan, S. Yip, and B. Yildiz, "Autonomous basin climbing method with sampling of multiple transition pathways: application to anisotropic diffusion of point defects in hcp zr," *Journal of Physics: Condensed Matter*, vol. 26, no. 36, p. 365402, 2014.

[25] D. J. Wales, "Discrete path sampling," *Molecular physics*, vol. 100, no. 2, pp. 3285–3305, 2002.

[26] D. J. Wales, "Some further applications of discrete path sampling to cluster isomerization," *Molecular physics*, vol. 102, no. 9-10, pp. 891–908, 2004.

[27] J. M. Carr and D. J. Wales, "Folding pathways and rates for the three-stranded β-sheet peptide beta3s using discrete path sampling," *Journal of Physical Chemistry B*, vol. 112, pp. 8760–8769, 2008.

[28] J. M. Carr and D. J. Wales, "Global optimization and folding pathways of selected α-helical proteins," *Journal of Chemical Physics*, vol. 123, p. 234901, 2005.

[29] P. Hanggi, P. Talkner, and M. Borkovec, "Reaction-rate theory: fifty years after kramers," *Reviews of Modern Physics*, vol. 62, no. 2, pp. 251–342, 1990.

[30] A. F. Voter, "Introduction to the kinetic monte carlo method," in *Radiation Effects in Solids*, pp. 1–23, Springer, 2007.

[31] G. Henkelman and H. Jonsson, "Improved tangent estimate in the nudged elastic band method for finding minimum energy paths and saddle points," *The Journal of chemical physics*, vol. 113, no. 22, pp. 9978–9985, 2000.

[32] D. Perez, B. P. Uberuaga, and A. F. Voter, "The parallel replica dynamics method - coming of age," *Computational Materials Science*, vol. 100, pp. 90–103, 2015.

[33] A. F. Voter, "Hyperdynamics: Accelerated molecular dynamics of infrequent events," *Physical Review Letters*, vol. 78, no. 20, p. 3908, 1997.

[34] M. R. So and A. F. Voter, "Temperature-accelerated dynamics for simulation of infrequent events," *The Journal of Chemical Physics*, vol. 112, no. 21, pp. 9599–9606, 2000.

[35] D. Perez, B. P. Uberuaga, Y. Shim, J. G. Amar, and A. F. Voter, "Accelerated molecular dynamics methods: introduction and recent developments," *Annual Reports in computational chemistry*, vol. 5, pp. 79–98, 2009.

[36] A. F. Voter, "Parallel replica method for dynamics of infrequent events," *Physical Review B*, vol. 57, no. 22, p. R13985, 1998.

[37] D. Hamelberg, J. Mongan, and J. A. McCammon, "Accelerated molecular dynamics: a promising and efficient simulation method for biomolecules," *The Journal of chemical physics*, vol. 120, no. 24, pp. 11919–11929, 2004.

[38] R. A. Miron and K. A. Fichthorn, "Accelerated molecular dynamics with the bond-boost method," *The Journal of chemical physics*, vol. 119, no. 12, pp. 6210–6216, 2003.

[39] S. Hara and J. Li, "Adaptive strain-boost hyperdynamics simulations of stress-driven atomic processes," *Physical Review B*, vol. 82, no. 18, p. 184114, 2010.

[40] S. Chakraborty, J. Zhang, and S. Ghosh, "Accelerated molecular dynamics simulations for characterizing plastic deformation in crystalline materials with cracks," *Computational Materials Science*, vol. 121, pp. 23–34, 2016.

[41] A. Kushima, X. Lin, J. Li, J. Eapen, J. C. Mauro, X. Qian, P. Diep, and S. Yip, "Computing the viscosity of supercooled liquids," *The Journal of chemical physics*, vol. 130, no. 22, p. 224504, 2009.

[42] A. Kushima, X. Lin, J. Li, X. Qian, J. Eapen, J. C. Mauro, P. Diep, and S. Yip, "Computing the viscosity of supercooled liquids. ii. silica and strong-fragile crossover behavior," *The Journal of chemical physics*, vol. 131, no. 16, p. 164505, 2009.

[43] Y. Fan, A. Kushima, and B. Yildiz, "Unfaulting mechanism of trapped self-interstitial atom clusters in bcc fe: A kinetic study based on the potential energy landscape," *Physical Review B*, vol. 81, no. 10, p. 104102, 2010.

[44] Y. Fan, B. Yildiz, and S. Yip, "Analogy between glass rheology and crystal plasticity: yielding at high strain rate," *Soft Matter*, vol. 9, no. 40, pp. 9511–9514, 2013.

[45] X.-Z. Tang, Y.-F. Guo, Y. Fan, S. Yip, and B. Yildiz, "Interstitial emission at grain boundary in nanolayered alpha-fe," *Acta Materialia*, vol. 105, pp. 147–154, 2016.

[46] P. Cao, M. Li, R. J. Heugle, H. S. Park, and X. Lin, "Self-learning metabasin escape algorithm for supercooled liquids," *Physical Review E*, vol. 86, no. 1, p. 016710, 2012.

[47] W. Ren and E. Vanden-Eijnden, "Finite temperature string method for the study of rare events," *The Journal of Physical Chemistry B*, vol. 109, no. 14, pp. 6688–6693, 2005.

[48] D. Sheppard, R. Terrell, and G. Henkelman, "Optimization methods for finding minimum energy paths," *The Journal of chemical physics*, vol. 128, no. 13, p. 134106, 2008.

[49] I. Popa, P. Kosuri, J. Alegre-Cebollada, S. Garcia-Manyes, and J. M. Fernandez, "Force dependency of biochemical reactions measured by single-molecule force-clamp spectroscopy," *Nat. Protocols*, vol. 8, no. 7, pp. 1261–1276, 2013.

[50] R. Perez-Jimenez, A. InglÃČÂľs-Prieto, Z.-M. Zhao, I. Sanchez-Romero, J. Alegre-Cebollada, P. Kosuri, S. Garcia-Manyes, T. J. Kappock, M. Tanokura, A. Holmgren, J. M. Sanchez-Ruiz, E. A. Gaucher, and J. M. Fernandez, "Single-molecule paleoenzymology probes the chemistry of resurrected enzymes," *Nat Struct Mol Biol*, vol. 18, no. 5, pp. 592–596, 2011.

[51] S. Garcia-Manyes, J. Liang, R. Szoszkiewicz, T.-L. Kuo, and J. M. Fernández, "Force-activated reactivity switch in a bimolecular chemical reaction," *Nature Chemistry*, vol. 1, no. 3, pp. 236–242, 2009.

[52] A. del Rio, R. Perez-Jimenez, R. Liu, P. Roca-Cusachs, J. M. Fernandez, and M. P. Sheetz, "Stretching single talin rod molecules activates vinculin binding," *Science*, vol. 323, no. 5914, pp. 638–641, 2009.

[53] K. C. Neuman and A. Nagy, "Single-molecule force spectroscopy: optical tweezers, magnetic tweezers and atomic force microscopy," *Nature Methods*, vol. 5, no. 6, pp. 491–505, 2008.

[54] W. Tao, G. Yoon, P. Cao, K. Eom, and H. S. Park, "β-sheet-like formation during the mechanical unfolding of prion protein," *Journal of Chemical Physics*, vol. 143, p. 125101, 2015.

[55] P. Cao, W. Tao, and H. S. Park, "Force-dependent mechanical unfolding pathways of GFP," *Extreme Mechanics Letters*, 2016. in press.

[56] H. S. Park, K. Gall, and J. A. Zimmerman, "Deformation of FCC nanowires by twinning and slip," *Journal of the Mechanics and Physics of Solids*, vol. 54, no. 9, pp. 1862–1881, 2006.

[57] V. Yamakov, D. Wolf, S. R. Phillpot, A. K. Mukherjee, and H. Gleiter, "Dislocation processes in the deformation of nanocrystalline aluminum by molecular-dynamics simulation," *Nature Materials*, vol. 1, pp. 1–4, 2002.

[58] T. Belytschko, S. P. Xiao, G. C. Schatz, and R. S. Ruoff, "Atomistic simulations of nanotube fracture," *Physical Review B*, vol. 65, p. 235430, 2002.

[59] P. Cao, H. S. Park, and X. Lin, "Strain-rate and temperature-driven transition in the shear transformation zone for two-dimensional amorphous solids," *Physical Review E*, vol. 88, p. 042404, 2013.

[60] P. Cao, X. Lin, and H. S. Park, "Surface shear-transformation zones in amorphous solids," *Physical Review E*, vol. 90, no. 1, p. 012311, 2014.

[61] T. Zhu, J. Li, A. Samanta, A. Leach, and K. Gall, "Temperature and strain-rate dependence of surface dislocation nucleation," *Physical Review Letters*, vol. 100, p. 025502, 2008.

[62] S. Ryu, K. Kang, and W. Cai, "Entropic effect on the rate of dislocation nucleation," *Proceedings of the National Academy of Science*, vol. 108, no. 13, pp. 5174–5178, 2011.

[63] W. L. Johnson and K. Samwer, "A universal criterion for plastic yielding of metallic glasses with a $(t/t_g)^{2/3}$ temperature dependence," *Physical Review Letters*, vol. 95, p. 195501, 2005.

[64] Y. Q. Cheng and E. Ma, "Intrinsic shear strength of metallic glass," *Acta Materialia*, vol. 59, pp. 1800–1807, 2011.

[65] J. D. Stevenson and D. J. Wales, "Communication: Analysing kinetic transition networks for rare events," *The Journal of chemical physics*, vol. 141, no. 4, p. 041104, 2014.

[66] D. J. Wales, "Calculating rate constants and committor probabilities for transition networks by graph transformation," *The Journal of chemical physics*, vol. 130, no. 20, p. 204111, 2009.

[67] T. T. Lau, A. Kushima, and S. Yip, "An atomistic method for slow structural deformations," in *IOP Conference Series: Materials Science and Engineering*, vol. 3, p. 012002, IOP Publishing, 2009.

[68] T. T. Lau, A. Kushima, and S. Yip, "Atomistic simulation of creep in a nanocrystal," *Physical review letters*, vol. 104, p. 175501, 2010.

[69] S. Plimpton, "Fast parallel algorithms for short-range molecular dynamics," *Journal of computational physics*, vol. 117, no. 1, pp. 1–19, 1995.

[70] Lammps *http://lammps.sandia.gov*, 2016.

[71] C. A. Schuh, T. C. Hufnagel, and U. Ramamurty, "Mechanical behavior of amorphous alloys," *Acta Materialia*, vol. 55, pp. 4067–4109, 2007.

[72] J. Sun, L. He, Y.-C. Lo, T. Xu, H. Bi, L. Sun, Z. Zhang, S. X. Mao, and J. Li, "Liquid-like pseudoelasticity of sub-10-nm crystalline silver particles," *Nature materials*, vol. 13, no. 11, pp. 1007–1012, 2014.

[73] X. H. Liu, L. Zhong, S. Huang, S. X. Mao, T. Zhu, and J. Y. Huang, "Size-dependent fracture of silicon nanoparticles during lithiation," *Acs Nano*, vol. 6, no. 2, pp. 1522–1531, 2012.

[74] U. Kasavajjula, C. Wang, and A. J. Appleby, "Nano-and bulk-silicon-based insertion anodes for lithium-ion secondary cells," *Journal of Power Sources*, vol. 163, no. 2, pp. 1003–1039, 2007.

[75] M. Winter and J. O. Besenhard, "Electrochemical lithiation of tin and tin-based intermetallics and composites," *Electrochimica Acta*, vol. 45, no. 1, pp. 31–50, 1999.

[76] G. Bucci, S. P. Nadimpalli, V. A. Sethuraman, A. F. Bower, and P. R. Guduru, "Measurement and modeling of the mechanical and electrochemical response of amorphous si thin film electrodes during cyclic lithiation," *Journal of the Mechanics and Physics of Solids*, vol. 62, pp. 276–294, 2014.

[77] R. A. Sharma and R. N. Seefurth, "Thermodynamic properties of the lithium-silicon system," *Journal of The Electrochemical Society*, vol. 123, no. 12, pp. 1763–1768, 1976.

[78] B. Boukamp, G. Lesh, and R. Huggins, "All-solid lithium electrodes with mixed-conductor matrix," *Journal of the Electrochemical Society*, vol. 128, no. 4, pp. 725–729, 1981.

[79] S.-P. Kim, D. Datta, and V. B. Shenoy, "Atomistic mechanisms of phase boundary evolution during initial lithiation of crystalline silicon," *The Journal of Physical Chemistry C*, vol. 118, no. 31, pp. 17247–17253, 2014.

[80] K. Zhao, M. Pharr, J. J. Vlassak, and Z. Suo, "Fracture of electrodes in lithium-ion batteries caused by fast charging," *Journal of Applied Physics*, vol. 108, no. 7, p. 073517, 2010.

[81] T. Hatchard and J. Dahn, "In situ xrd and electrochemical study of the reaction of lithium with amorphous silicon," *Journal of The Electrochemical Society*, vol. 151, no. 6, pp. A838–A842, 2004.

[82] L. Beaulieu, K. Eberman, R. Turner, L. Krause, and J. Dahn, "Colossal reversible volume changes in lithium alloys," *Electrochemical and Solid-State Letters*, vol. 4, no. 9, pp. A137–A140, 2001.

[83] L. Beaulieu, T. Hatchard, A. Bonakdarpour, M. Fleischauer, and J. Dahn, "Reaction of li with alloy thin films studied by in situ afm," *Journal of The Electrochemical Society*, vol. 150, no. 11, pp. A1457–A1464, 2003.

[84] L. Beaulieu, K. Hewitt, R. Turner, A. Bonakdarpour, A. Abdo, L. Christensen, K. Eberman, L. Krause, and J. Dahn, "The electrochemical reaction of li with amorphous si-sn alloys," *Journal of The Electrochemical Society*, vol. 150, no. 2, pp. A149–A156, 2003.

[85] P. Limthongkul, Y.-I. Jang, N. J. Dudney, and Y.-M. Chiang, "Electrochemically-driven solid-state amorphization in lithium-silicon alloys and implications for lithium storage," *Acta Materialia*, vol. 51, no. 4, pp. 1103–1113, 2003.

[86] P. Limthongkul, Y.-I. Jang, N. J. Dudney, and Y.-M. Chiang, "Electrochemically-driven solid-state amorphization in lithium–metal anodes," *Journal of power sources*, vol. 119, pp. 604–609, 2003.

[87] C. K. Chan, H. Peng, G. Liu, K. McIlwrath, X. F. Zhang, R. A. Huggins, and Y. Cui, "High-performance lithium battery anodes using silicon nanowires," *Nature nanotechnology*, vol. 3, no. 1, pp. 31–35, 2007.

[88] N. Ding, J. Xu, Y. Yao, G. Wegner, X. Fang, C. Chen, and I. Lieberwirth, "Determination of the diffusion coefficient of lithium ions in nano-si," *Solid State Ionics*, vol. 180, no. 2, pp. 222–225, 2009.

[89] J. Xie, N. Imanishi, T. Zhang, A. Hirano, Y. Takeda, and O. Yamamoto, "Li-ion diffusion in amorphous si films prepared by rf magnetron sputtering: A comparison of using liquid and polymer electrolytes," *Materials Chemistry and Physics*, vol. 120, no. 2, pp. 421–425, 2010.

[90] K. Yoshimura, J. Suzuki, K. Sekine, and T. Takamura, "Measurement of the diffusion rate of li in silicon by the use of bipolar cells," *Journal of Power Sources*, vol. 174, no. 2, pp. 653–657, 2007.

[91] G. A. Tritsaris, K. Zhao, O. U. Okeke, and E. Kaxiras, "Diffusion of lithium in bulk amorphous silicon: a theoretical study," *The Journal of Physical Chemistry C*, vol. 116, no. 42, pp. 22212–22216, 2012.

[92] S. O. Nielsen, R. E. Bulo, P. B. Moore, and B. Ensing, "Recent progress in adaptive multiscale molecular dynamics simulations of soft matter," *Physical Chemistry Chemical Physics*, vol. 12, no. 39, pp. 12401–12414, 2010.

[93] Y. Fan, A. Kushima, S. Yip, and B. Yildiz, "Mechanism of void nucleation and growth in bcc fe: atomistic simulations at experimental time scales," *Physical review letters*, vol. 106, no. 12, p. 125501, 2011.

[94] G. Henkelman, B. P. Uberuaga, and H. Jónsson, "A climbing image nudged elastic band method for finding saddle points and minimum energy paths," *The Journal of Chemical Physics*, vol. 113, no. 22, pp. 9901–9904, 2000.

[95] M.-S. Lee, K. Lee, S.-Y. Kim, H. Lee, J. Park, K.-H. Choi, H.-K. Kim, D.-G. Kim, D.-Y. Lee, S. Nam, and J.-U. Park, "High-performance, transparent, and stretchable

electrodes using graphene–metal nanowire hybrid structures," *Nano letters*, vol. 13, no. 6, pp. 2814–2821, 2013.

[96] J. A. Rogers, T. Someya, and Y. Huang, "Materials and mechanics for electronics," *Science*, vol. 327, no. 5973, pp. 1603–1607, 2010.

[97] M. Park, J. Im, M. Shin, Y. Min, J. Park, H. Cho, S. Park, M.-B. Shim, S. Jeon, D.-Y. Chung, J. Bae, J. Park, J. Unyong, and K. Kinam, "Highly stretchable electric circuits from a composite material of silver nanoparticles and elastomeric fibres," *Nature nanotechnology*, vol. 7, no. 12, pp. 803–809, 2012.

[98] H. Gleiter, "Nanostructured materials: basic concepts and microstructure," *Acta materialia*, vol. 48, no. 1, pp. 1–29, 2000.

[99] J. Biener, A. M. Hodge, J. R. Hayes, C. A. Volkert, L. A. Zepeda-Ruiz, A. V. Hamza, and F. F. Abraham, "Size effects on the mechanical behavior of nanoporous au," *Nano letters*, vol. 6, no. 10, pp. 2379–2382, 2006.

[100] J. R. Greer, W. C. Oliver, and W. D. Nix, "Size dependence of mechanical properties of gold at the micron scale in the absence of strain gradients," *Acta Materialia*, vol. 53, no. 6, pp. 1821–1830, 2005.

[101] Z. H. Aitken, H. Fan, J. A. El-Awady, and J. R. Greer, "The effect of size, orientation and alloying on the deformation of az31 nanopillars," *Journal of the Mechanics and Physics of Solids*, vol. 76, pp. 208–223, 2015.

[102] S.-W. Lee, A. T. Jennings, and J. R. Greer, "Emergence of enhanced strengths and bauschinger effect in conformally passivated copper nanopillars as revealed by dislocation dynamics," *Acta Materialia*, vol. 61, no. 6, pp. 1872–1885, 2013.

[103] Q. Guo, P. Landau, P. Hosemann, Y. Wang, and J. R. Greer, "Helium implantation effects on the compressive response of cu nanopillars," *Small*, vol. 9, no. 5, pp. 691–696, 2013.

[104] A. Jennings, C. Gross, F. Greer, Z. Aitken, S.-W. Lee, C. Weinberger, and J. Greer, "Higher compressive strengths and the bauschinger effect in conformally passivated copper nanopillars," *Acta Materialia*, vol. 60, no. 8, pp. 3444–3455, 2012.

[105] C. R. Weinberger and W. Cai, "Surface-controlled dislocation multiplication in metal micropillars," *Proceedings of the National Academy of Sciences*, vol. 105, no. 38, pp. 14304–14307, 2008.

[106] C. R. Weinberger and W. Cai, "The stability of lomer–cottrell jogs in nanopillars," *Scripta Materialia*, vol. 64, no. 6, pp. 529–532, 2011.

[107] C. J. Healy and G. J. Ackland, "Molecular dynamics simulations of compression–tension asymmetry in plasticity of fe nanopillars," *Acta Materialia*, vol. 70, pp. 105–112, 2014.

[108] T. Zhu, J. Li, A. Samanta, A. Leach, and K. Gall, "Temperature and strain-rate dependence of surface dislocation nucleation," *Physical Review Letters*, vol. 100, no. 2, p. 025502, 2008.

[109] M. Baskes, "Application of the embedded-atom method to covalent materials: a semiempirical potential for silicon," *Physical review letters*, vol. 59, no. 23, p. 2666, 1987.

[110] S. J. Plimpton and A. P. Thompson, "Computational aspects of many-body potentials," *MRS bulletin*, vol. 37, no. 05, pp. 513–521, 2012.

[111] Y. Fan, Y. N. Osetsky, S. Yip, and B. Yildiz, "Onset mechanism of strain-rate-induced flow stress upturn," *Physical review letters*, vol. 109, no. 13, p. 135503, 2012.

[112] L. Nguyen, K. Baker, and D. Warner, "Atomistic predictions of dislocation nucleation with transition state theory," *Physical Review B*, vol. 84, no. 2, p. 024118, 2011.

[113] J. E. Angelo, N. R. Moody, and M. I. Baskes, "Trapping of hydrogen to lattice defects in nickel," *Modelling and Simulation in Materials Science and Engineering*, vol. 3, no. 3, p. 289, 1995.

[114] M. Baskes, X. Sha, J. Angelo, and N. Moody, "Trapping of hydrogen to lattice defects in nickel," *Modelling and Simulation in Materials Science and Engineering*, vol. 5, no. 6, p. 651, 1997.

[115] J.-M. Tarascon and M. Armand, "Issues and challenges facing rechargeable lithium batteries," *Nature*, vol. 414, no. 6861, pp. 359–367, 2001.

[116] X. H. Liu, H. Zheng, L. Zhong, S. Huang, K. Karki, L. Q. Zhang, Y. Liu, A. Kushima, W. T. Liang, J. W. Wang, J.-H. Cho, E. Epstein, S. A. Dayeh, S. T. Picraux, T. Zhu, J. Li, J. P. Sullivant, J. Cumings, C. Wang, S. X. Mao, Z. Z. Ye, S. Zhang, and J. Y. Huang, "Anisotropic swelling and fracture of silicon nanowires during lithiation," *Nano letters*, vol. 11, no. 8, pp. 3312–3318, 2011.

[117] J. Maranchi, A. Hepp, A. Evans, N. Nuhfer, and P. Kumta, "Interfacial properties of the a-si/ cu: active–inactive thin-film anode system for lithium-ion batteries," *Journal of the Electrochemical Society*, vol. 153, no. 6, pp. A1246–A1253, 2006.

[118] H. B. Chew, B. Hou, X. Wang, and S. Xia, "Cracking mechanisms in lithiated silicon thin film electrodes," *International Journal of Solids and Structures*, vol. 51, no. 23, pp. 4176–4187, 2014.

[119] H. Wang, B. Hou, X. Wang, S. Xia, and H. B. Chew, "Atomic-scale mechanisms of sliding along an interdiffused li–si–cu interface," *Nano letters*, vol. 15, no. 3, pp. 1716–1721, 2015.

[120] S. W. Lee, M. T. McDowell, L. A. Berla, W. D. Nix, and Y. Cui, "Fracture of crystalline silicon nanopillars during electrochemical lithium insertion," *Proceedings of the National Academy of Sciences*, vol. 109, no. 11, pp. 4080–4085, 2012.

[121] A. Kushima, J. Y. Huang, and J. Li, "Quantitative fracture strength and plasticity measurements of lithiated silicon nanowires by in situ tem tensile experiments," *ACS nano*, vol. 6, no. 11, pp. 9425–9432, 2012.

[122] A. T. Jennings, J. Li, and J. R. Greer, "Emergence of strain-rate sensitivity in cu nanopillars: Transition from dislocation multiplication to dislocation nucleation," *Acta Materialia*, vol. 59, no. 14, pp. 5627–5637, 2011.

[123] A. F. Bower, P. R. Guduru, and V. A. Sethuraman, "A finite strain model of stress, diffusion, plastic flow, and electrochemical reactions in a lithium-ion half-cell," *Journal of the Mechanics and Physics of Solids*, vol. 59, no. 4, pp. 804–828, 2011.

[124] L. Brassart and Z. Suo, "Reactive flow in solids," *Journal of the Mechanics and Physics of Solids*, vol. 61, no. 1, pp. 61–77, 2013.

[125] H. Wang, X. Wang, S. Xia, and H. B. Chew, "Brittle-to-ductile transition of lithiated silicon electrodes: Crazing to stable nanopore growth," *The Journal of chemical physics*, vol. 143, no. 10, p. 104703, 2015.

[126] H. Wang and H. B. Chew, "Molecular dynamics simulations of plasticity and cracking in lithiated silicon electrodes," *Extreme Mechanics Letters*, 2016.

[127] J. Luo, J. Wang, E. Bitzek, J. Y. Huang, H. Zheng, L. Tong, Q. Yang, J. Li, and S. X. Mao, "Size-dependent brittle-to-ductile transition in silica glass nanofibers," *Nano letters*, vol. 16, no. 1, pp. 105–113, 2015.

[128] F. Shimizu, S. Ogata, and J. Li, "Theory of shear banding in metallic glasses and molecular dynamics calculations," *Materials transactions*, vol. 48, no. 11, pp. 2923–2927, 2007.

[129] W. Li, J. M. Rieser, A. J. Liu, D. J. Durian, and J. Li, "Deformation-driven diffusion and plastic flow in amorphous granular pillars," *Physical Review E*, vol. 91, no. 6, p. 062212, 2015.

[130] M. Falk and J. Langer, "Dynamics of viscoplastic deformation in amorphous solids," *Physical Review E*, vol. 57, no. 6, p. 7192, 1998.

[131] P. Brommer and N. Mousseau, "Comment on âĂIJmechanism of void nucleation and growth in bcc fe: Atomistic simulations at experimental time scalesâĂİ," *Physical review letters*, vol. 108, no. 21, p. 219601, 2012.

[132] Y. Fan, A. Kushima, S. Yip, and B. Yildiz, "Fan et al. reply," *Physical Review Letters*, vol. 108, no. 21, p. 219602, 2012.

[133] H. Wang, D. Xu, D. Rodney, P. Veyssière, and R. Yang, "Atomistic investigation of the annihilation of non-screw dislocation dipoles in al, cu, ni and γ-tial," *Modelling and Simulation in Materials Science and Engineering*, vol. 21, no. 2, p. 025002, 2013.

[134] H. Wang, D. Xu, and R. Yang, "Defect clustering upon dislocation annihilation in α-titanium and α-zirconium with hexagonal close-packed structure," *Modelling and Simulation in Materials Science and Engineering*, vol. 22, no. 8, p. 085004, 2014.

[135] D. D. Hsu, W. Xia, S. G. Arturo, and S. Keten, "Systematic method for thermodynamically consistent coarse-graining: a universal model for methacrylate-based polymers," *Journal of Chemical Theory and Computation*, vol. 10, pp. 2514–2527, 2014.